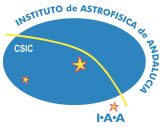

UNIVERSIDAD DE GRANADA

Tesis doctoral
Noviembre 2009

A SEARCH FOR MECHANISMS PRODUCING CIRCULAR POLARIZATION IN COMETS

[PhD THESIS]

Daniel Guirado Rodríguez
Instituto de Astrofísica de Andalucía (CSIC)

Memoria de Tesis
presentada en la Universidad de Granada
para optar al grado de Doctor en Física

Directores de tesis:
Dr. Fernando Moreno Danvila
Dra. Olga Muñoz Gómez

Editor: Editorial de la Universidad de Granada
Autor: Daniel Guirado Rodríguez
D.L.: GR 2672-2010
ISBN: 978-84-693-1999-4

Agradecimientos

Lo difícil de hacer una lista de agradecimientos es terminarla, por extensión y por olvido, así que aquí va mi lista incompleta. Desen todos los olvidados por agradecidos.

A quienes primero tengo que decir gracias es a Fernando y a Olga, por haberme enseñado todo lo que hacer falta para ser un científico (otra cosa es que yo haya aprendido algo), por seguir confiando en mí a pesar de mi delirio por la procrastinación, y también por su entrega total en este final de tesis de *Fórmula 1*, en el que ellos lo han pasado peor que yo (lo cierto es que creo que yo he disfrutado, soy adicto a la adrenalina).

A mis compañeros del IAA les debo una buena ronda de abrazos de reconocimiento, y a más de uno un sombrerazo con reverencia, porque hacen de este edificio un sitio en el que estoy tan a gusto que hasta tengo un colchón y unas zapatillas en el despacho. Me divierte pasear por los pasillos salpicando chascarrillos (o escupiendo juramentos, depende del día), y tengo en la memoria un buen álbum de fotos de momentos con cada uno. Jamás se me ocurriría destacar a ninguno por encima de los demás. Pero si me obligaran con una pistola a nombrar alguna situación, me quedo con los ratos de madrugada con Paco Navarro en el pasillo: él enfundado en su pijama, y arreglando el mundo a golpe de cigarro, mientras a mí me faltaba una barra debajo del codo y un vaso en la mano contraria con los que decorar la escena.

El triunvirato es cosa aparte, trasciende lo institucional. Es difícil que yo conecte con alguien, y más aún que la conexión sea duradera. Darío, Charly y *El Boquerón* han sido durante cinco años esos amigos de base que uno hace en cada estación en la que para su tren, y que luego se conservan para siempre sin necesidad de un intercambio de favores continuado. Charly gritando sin control, Darío intentando poner calma, y Miguel Ángel "emboqueronao" mientras yo cuento alguna historia, es la la habitual escena de este cuarteto de corte marxista (por la rama grouchiana), en el que he tenido la suerte de verme involucrado. Gracias por los ratos de cháchara en el patio, por las doce tapas, por la caña de la una y por las noches de juego impecable. Que siga este equipo haciendo su magia con el balón, aunque tenga que llevarse cada uno su balón en la maleta.

También he tenido ocasión de viajar en este tiempo de tesis, y conocer a gente con duende, de ésa que pulsa alguna tecla olvidada del piano de la mente y de pronto te descubre un abanico enorme de nuevas melodías posibles. Gracias a Joop Hovenier por recibirme y por tratarme siempre como a un amigo. No me cabe en la maleta de la memoria todo lo que me ha intentado enseñar, pero supongo que ya iré sacando prendas a lo largo del viaje.

Y hablando de viajes, en el viaje de la edad me he encontrado con compañeros que han sido tan decisivos en que yo escriba esta tesis, como el tribunal pertienente que decidiera la concesión de mi beca. Son mis maestros y profesores desde el colegio. Creo que he tenido una suerte increíblemente inusual, porque guardo un recuerdo excelente de todos. No está bien destacar a nadie, pero yo ya he demostrado sobradamente mi amor por lo inmoral, lo ilegal, y hasta lo pecaminoso, así que no me voy a resisir a reconocer que una parte (la buena) de mi actitud hacia el trabajo y de mi conciencia de equipo se la debo a Don Miguel Salvador, a quien le agradezco haberse extralimitado en sus labores de maestro, y haber enseñado mucho más que Matemáticas y Ciencias Narutales a esa panda de jóvenes neandertales submentales sin futuro entre la que me encontraba yo. Y mi mensaje en la botella es para Juan Simón. No sé a dónde gritar esto, Juan, para que lo oigas, pero el 100% de la curiosidad científica que hay en mí me la pegaste tú, y no soy el único. Ojalá te hubiera dicho esto a ti antes, así podría habértelo dicho a ti.

Bueno, tengo una colección de amigos que es como un plato de *El Bulli*: escasa pero exquisita (y una colección de enemigos como una enorme fuente de patatas fritas de paquete). Su fidelidad supera mis méritos en el campo de la apatía, y su compañía durante estos años de tesis me ha devuelto periódicamente a la estabilidad y a la vida sosegada que requiere este trabajo sin horario ni calendario. No caben todos en los dedos de la mano, y sin esa técnica no podré retener la lista completa, así que sólo diré que gracias a Miguel por ser mi hermano, al *Consejo de la Fiesta del Vino* en pleno por darme cada año un día imborrable, y a todos los *Ana Lógica* por haberme integrado en su cuadro de cosas curiosas que contar en los bares, y por haberme dado una aventura que contar yo cuando ya no tenga edad más que para recopilar mis fechorías.

Pero también tengo otro tipo de amigos a los que debo agradecer profundamente un buen porcentaje de lo que queda de mi salud mental tras los años de elaboración de esta tesis. Gracias a Groucho Marx, a Woody Allen, a Julio Verne, a Brian Wilson, a Ray Davies, a los 4 Beatles y sus santas madres, porque aunque ninguno de ellos me conocerá jamás, han llenado mi tiempo de vida, y no tendré en la vida tiempo de disfrutar de ellos tanto como sus genialidades se merecen.

Si tengo que hacer una lista de las personas que más han sufrido esta tesis, podría dudar sobre la segunda y la tercera, pero la medalla de oro está clarísima. Gracias, Pérez, por devolverme una pluma por cada piedra que te he lanzado, como los buenos futbolistas. Gracias por tener la solución antes de que yo tuviera el problema, y sobre todo, gracias por aguantarme y por hacer que parezca fácil. Eres la médica que más sabe de polarización circular del mundo, y yo me hago el chulo hablando de Medicina cuando alguien

comenta su dolencia. “Gracias” no es un premio suficiente a tu labor. Soy mal pagador.

El postre se toma al final, porque así queda el regusto a chocolate, así que si hiciera falta, éste sería el punto en el que dijera gracias a mis padres y a mis hermanas. Somos cinco marineros en tierra, hipotecados desde hace siglos por un barco que zozobra más que avanza, pero que viene cubriendo sus rutas puntualmente desde el principio. Aquí tenemos otro puerto en el que parar un rato a tomar un respiro y a beber una jarra de vino antes de seguir con nuestro itinerario inquebrantable. Me alegra haber sido el timonel en esta ocasión.

Y nada más por hoy (como la canción de *091*), no porque no tenga más que decir, sino porque ya es tan tarde que está amaneciendo (estas cosas hay que escribirlas de noche), y yo ya no podré dormir, como siempre me pasa.

A Los Lentejos, que de todos
los que nunca van a leer esta tesis,
son quienes más han puesto en ella.

Resumen

El presente trabajo está orientado a la búsqueda de los mecanismos físicos que puedan explicar el grado de polarización circular observado en los cometas. Con objeto de establecer una lista de los posibles mecanismos, primero derivamos una condición necesaria para que aparezca un cierto grado de polarización circular no nulo, la cual es que la simetría del sistema respecto a la dirección de la luz incidente debe romperse de alguna manera. El siguiente paso fue identificar los mecanismos que cumplen ese requisito. En primer lugar, investigamos el alineamiento de los granos en el coma, que, de hecho, ha sido propuesto por varios autores como una posible causa de la polarización circular. Para ello desarrollamos un modelo numérico de alineamiento de los granos por el viento solar de tipo Monte Carlo. Nuestros resultados muestran que las partículas elongadas se alinean en unas horas, pero el grado de polarización circular que se produce es nulo, lo cual es debido a la configuración simétrica respecto a la dirección de la luz incidente que se genera por ese alineamiento. Como segundo mecanismo, se ha investigado la dispersión simple de la luz por partículas asimétricas ópticamente inactivas. En este caso, y para dos partículas modelo muy concretas, encontramos un nivel del grado de polarización circular resultante del orden de el observado, e incluso mayor. Sin embargo, como quiera que las partículas en un coma real deben estar distribuidas en una gran cantidad de tamaños y formas, realizamos una extensión de los cálculos teniendo en cuenta esta circunstancia. Los resultados fueron negativos, en el sentido de que a medida que en la distribución se iban añadiendo cada vez más formas y tamaños, el grado de polarización circular se acercaba cada vez más a cero. En tercer lugar descartamos la posibilidad de que la actividad óptica de los materiales que componen el polvo del coma sea la responsable de la polarización circular en los cometas. La razón es que los resultados producidos no encajarían con algunas de las características encontradas en las observaciones. El cuarto y último mecanismo que propusimos fue el de la dispersión multiple en condiciones de asimetría respecto de la dirección de la luz incidente. Para el estudio de este mecanismo fue necesario desarrollar un programa de tipo Monte Carlo que simulara el transporte radiativo en estas atmósferas. A partir de este programa pudimos calcular el flujo y los grados de polarización lineal y circular de la luz emergente de un coma cometario, tanto ópticamente delgado como grueso, es decir, en condiciones de dispersión simple o múltiple. Después de estudiar los resultados del código para diferentes parámetros de entrada que caracterizan a la atmósfera cometaria y a la región que se observa, llegamos a la conclusión de que este mecanismo es el único que puede producir por sí mismo los niveles observados del grado de polarización circular en los cometas.

Abstract

In this work, a systematic study aimed at identifying all possible mechanisms producing the observed non-zero degree of circular polarization in the light scattered by comets is presented. In order to make a list of possible mechanisms, we first derived a necessary condition, which is that the symmetry of the system around the direction of the incident light must be broken somehow. Then, we made a search for the mechanisms fulfilling this condition. The first mechanism tested was the grain alignment, that has been proposed by several authors as the cause for the presence of a certain degree of circular polarization in comets. To this end, we developed a Monte Carlo model of grain alignment by solar wind particles. We found that elongated particles do align in a few hours by this mechanism, but they do not produce any degree of circular polarization owing to the azimuthally symmetrical configuration with respect to the direction of the incident light that results from the alignment. The second mechanism tested was the single scattering of light by optically inactive asymmetrical particles. In this case (just for two specific model shapes), we found a significant degree of circular polarization in the scattered light, comparable to, or even higher than, the observed. However, in a real cometary atmosphere there must exist a large variety of asymmetrical particles with different sizes and shapes, so that an extension of these calculations to samples of distributions of asymmetrical particles of many different sizes and shapes was also conducted. The result was negative, in the sense that for the whole sample the degree of circular polarization tends asymptotically to zero as more and more particles are added to the system. Third, we ruled out the possibility of the optical activity of the materials forming the dust particles of the coma to be responsible for the degree of circular polarization observed in comets. The reason is that the produced results would not match some of the features we found in the observations. The fourth, and last, mechanism we tried was the presence of multiple scattering in an azimuthally asymmetrical scenario around the direction of the incoming light. To accomplish this, a Monte Carlo model of radiative transfer in cometary comae was developed. The model is capable of giving the flux, and the degree of linear and circular polarization of light emerging from dusty cometary environments, under conditions of either single or multiple scattering. After trying several scenarios corresponding to different physical parameters of the cometary atmosphere, and different observational conditions, we concluded that the multiple scattering processes are the only mechanism that might give rise to the observed degree of circular polarization by itself.

Contents

Chapter 1

Introduction

Comets were formed at the beginning of the Solar System formation, and since their genesis they have remained quite isolated in very clear regions far away from the Sun and from any other massive body of the Solar System (see Sec. 2.2). Hence, since their beginning, they have been prevented more than any other type of bodies of the Solar System from heating, from the interaction with massive planets, and from collisions with other small bodies. Thus, comets are regarded as the most pristine objects in the Solar System, representing the most primitive form of the material out of which all Solar System bodies have formed, and giving information on their formation and evolution.

Once they were formed, comets that did not escape from the Solar System or crash into any other object, remained moving around the Sun in very far orbits (Sec. 2.2). Eventually, because of some dynamical perturbation, they are taken out from their orbits and sometimes fall into the inner Solar System, becoming observable from Earth.

The surface features of a comet nucleus cannot be observed from Earth because it is just a few kilometers wide (the largest nucleus ever observed was Hale-Bopp's 40 km across). However, close to the Sun, comets exhibit dust comae and tails driven by ice sublimation owing to high temperature. The coma usually reach dimensions of the order of 10^4 kilometers and become observable because of light scattered by the dust particles (see Chap. 4).

The study of the composition of the dust contained in comets may give us some information about the primordial composition of the Solar System. Getting some knowledge about the shape and internal structure of those grains may provide us with some clues about the physical processes that those particles underwent during their formation in the primordial Solar System 4.6 billion years ago.

A way to carry out such a study is to send a spacecraft to the comet and

perform *in situ* measurements or take some samples. Making measurements and sending the data back to Earth is the goal of the ESA space mission *Rosetta*, which was launched on March 2nd, 2004, and is expected to start orbiting around Comet 67P/Churyumov-Gerasimenko in 2014. The orbiter will rotate around the coma, but also a lander module will be deployed and will make measurements on the surface of the nucleus.

Figure 1.1: *Rosseta* mission module. **Credit: ESA**.

Another recent space mission to study comets was *Stardust*, by NASA. It consisted of a probe that travelled to the nearby of Comet P/Wild 2 to capture some dust grains in an aerogel and send them back to Earth in a module that landed in the dessert of Utah on January 15th, 2006. Particles captured in the aerogel were localized in microscopic pictures with the help of volunteers, and they were extensively analyzed by NASA scientists (see, e.g., [26]).

Deep Impact was a previous mission performed by NASA. It consisted on crashing a projectile of 370 kg on the surface of Comet Temple 1 on the 4th of July, 2005. Scientists observed then from Earth the cloud of gas and dust ejected from the nucleus

The only remote way of studying a comet is by the light it scatters. To retrieve information on the physical properties of the scattering particles, we must relate the properties of the observed scattered light to the physical properties of the scatterers.

In the present work, we focus on one of the properties of the scattered light: *circular polarization*. Our goal is then to identify the mechanisms giving the observed degree of circular polarization in comets, i.e., to establish

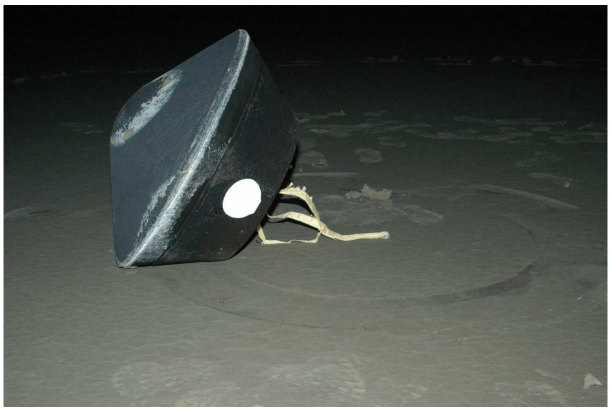

Figure 1.2: *Stardust* module containing the collected dust particles, just after landing in the dessert of Utah, on January 15th, 2006. **Credit: NASA**.

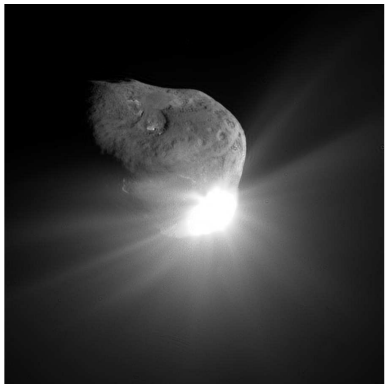

Figure 1.3: Impact of the *Deep Impact* projectile on the nucleus of Comet Temple 1. **Credit: NASA**.

which properties of the particles in the coma, or the surface of the nucleus, may explain the observations.

The theoretical basis on comets and light scattering are presented in Chaps. 2 and 3 respectively. In Chap. 4 we make a summary of some of the available observations of the degree of circular polarization in comets, and point out the common properties of all of them and their remarkable features. Once the observations are described and analyzed, we make a theoretical approach to the problem by deriving a necessary condition for a mechanism to circularly polarize light, and elaborate a list of candidate mechanisms based on that condition (Chap. 5). Then, the following mechanisms are studied: alignment of non-spherical particles, in Chap. 6, presence of randomly oriented asymmetrical grains, in Chaps. 7 and 8, scattering by optically active

materials (Chap. 9), and finally, in Chap. 10, multiple scattering by a local non-central region of a coma. A summary of the general conclusions of the present work are presented in Chap. 11, and Chap. 12 contains a list of some work items to be accomplished in the near future.

Chapter 2

Basics on comets

2.1 Definition of comet

Along with asteroids, centaurs, and transneptunian objects, comets belong to the so-called small Solar System bodies category. They can be described as kilometer-sized irregularly-shaped chunks of dusty ice that develop a shell of sublimated gas with dust, a tail of gas, and another tail of dust when they approach the Sun.

A rigorous definition of comets is given by Festou et al. (1993) [19]. Their definition of the different parts of a comet is as follows:

- *Nucleus: a kilometer-sized, irregularly shaped, solid body of relatively loose internal cohesion, consisting of ices (frozen gases; mostly H_20) with imbedded dust particles. The nuclei move in elliptical, sometimes nearly parabolic orbits in the solar system. The orbits are basically unstable, due to the variable action of the gravitational attraction of the planets and are also influenced by "non-gravitational" forces caused by anisotropic out-gassing from the nuclei.*

- *Coma: a gaseous and dusty atmosphere around the nucleus which develops when it is heated as it approaches the Sun and again abates during the outward motion in the orbit. The coma consists of evaporated molecules and their daughter products (radicals, atoms, ions) as well as dust particles released in the same process. Depending on the distribution of "active" areas on the surface of the nucleus, comae may be featureless or highly structured (jets, shells). They shine by atomic and molecular emissions, mostly excited by fluorescence, by sunlight reflected by the dust and by thermal emission at infrared wavelengths.*

- *Ion tail: consisting of ions which are lost from the coma and accelerated in the anti-solar direction by action of the interplanetary magnetic field carried by the solar wind. Ion tails shine by the fluorescence from their ions.*

- *Dust tail: consisting of dust particles lost from the coma and spread along the orbit while subjected to pressure of the solar radiation. Dust tails shine by reflected sunlight and thermal infrared emission and they are an important source of interplanetary material.*

Figure 2.1: Comet Hale-Bopp in 1997. The coma is the brightest region near the center. Both tails emerge from the coma: the ionic tail (blue), in the anti-solar direction, is due to the interaction of the solar wind with the gas of the coma, and the dust tail (yellow) is slightly curved owing to radiation pressure. **Credit: E. Kolmhofer, H. Raab; Johannes-Kepler-Observatory, Linz, Austria.**

The nuclei of comets do absorb almost all light that they receive. Let us define the *surface albedo* of the nucleus as the ratio between the reflected and the received radiation energy. Some measurements have been performed of such a ratio, and it is of the order of 4% (see, e.g. [32, 33]).

2.2 The origin of comets

Comets are usually divided into two types by the period of their orbit [15]:

1. Short-period comets:
    - Less than 200 years period.
    - Orbits of 30 - 100 AU in semi-major axis.
    - Low inclination of the orbits with respect to the ecliptic plane.
2. Long-period comets
    - More than 200 years period.
    - Orbits of 10,000 AU or larger in semi-major axis.
    - Isotropic distribution of the inclination of orbits.

The generally accepted interpretation of this classification is that there are two different origins for comets [15]: Planetesismals forming in the region of the Jovian planets were ice-rich, because that zone is beyond the frost line of the Solar System. Some of these planetesismals underwent close gravitational encounters with the Jovian planets, and that made a number of them to be cast away in all directions. Some may have completely escaped from the Solar System and now are drifting through the interstellar space. The rest ended up in orbits with very large average distances from the Sun. These became objects of the Oort cloud, a spherical shell that lies roughly 50,000 AU from the Sun. A dynamical perturbation caused, for instance, by a near supernova explosion, may take some of these objects out of their orbits and a number of them could fall into the inner Solar System. This is supposed to be the origin of the long-period comets. Planetesimals formed beyond Neptune were even more ice-rich than those forming among the Jovian planets. They could not aggregate into larger bodies because the low density of material in that zone makes very unlikely an encounter of two objects. As they did not have gravitational interactions with the massive Jovian planets, they remained in the region where they were formed, building up the so called *Kuiper belt*. Obviously, the Kuiper belt is quite plane, it coincides with the plane of the ecliptic and it starts at the orbit of Neptune ($\approx 30\ AU$). Some of the objects lying in the Kuiper belt may fall into the inner Solar System after any kind of dynamical perturbation of their orbits. This is thought to be the origin of the short-period comets. According to this interpretation, short-period comets were formed further away than long-period ones.

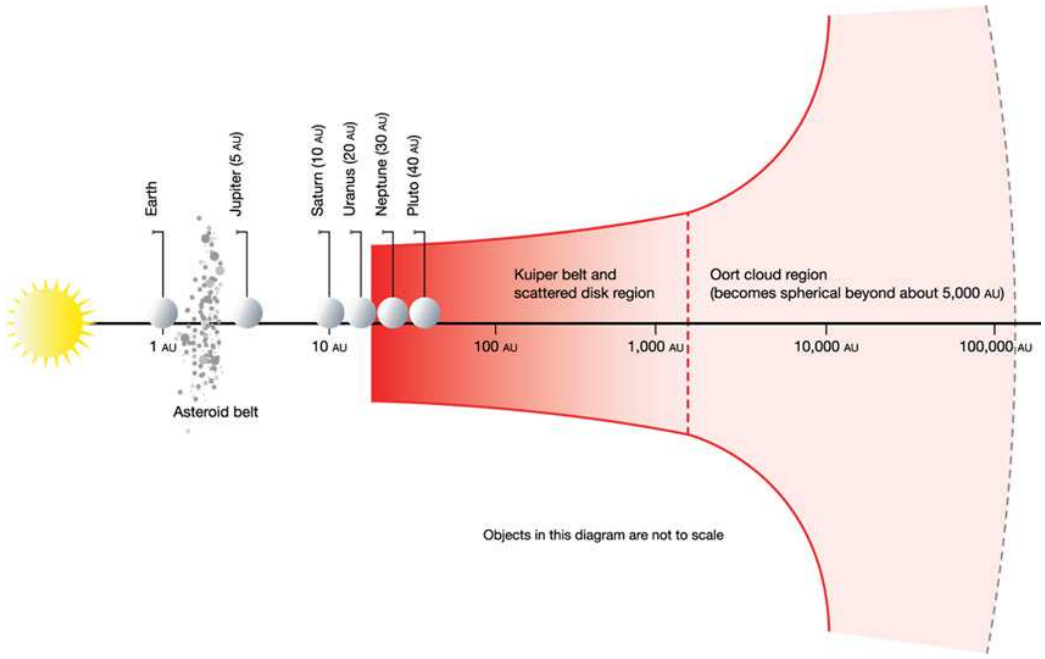

Figure 2.2: Sketch of the outer part of the Solar System: the plane region that starts at the orbit of Neptune is the Kuiper belt, where short-period comets come from. Long-period comets come from the far spherical shell: the Oort cloud. **Credit: Stern 2003 [66].**

2.3 Composition of the dust

Historically, silicates have been considered the main components of comets, according to infrared spectra. The first detection of the silicate $10-\mu m$ band was made by Maas et al. in 1970 [41].

In 1997, Kolokolova & Jockers [36] presented a work in which they fitted the refractive index of the dust particles for the wavelength dependence of the linear polarization to coincide with that typically observed in comets. The fit was made based on observations of several comets. They deduced that cometary dust grains are mainly composed of silicates, with less than 1% (in volume) of metallic and carbon inclusions.

A very complete study based on the fit of infrared spectra, and the measured degree of linear polarization of the scattered light at various phase angles and wavelengths, was carried out by Min et al. in 2005 [48]. They studied the composition of Comet Hale-Bopp, and deduced that dust grains were mainly formed by amorphous carbon (39.1% in volume), amorphous olivine (25.7%) and amorphous pyroxene (18.3%). Crystalline silicicates were also inferred to be present in comets, but in a much lower abundance. In this

study, silicates are still the primary component, although carbon becomes a main component too.

More recently, much more direct information on the composition of cometary dust of Comet Wild 2 has been retrieved from Stardust mission. The analysis of the sample reveals that silicates are indeed the main components [5, 26], but this time the abundance of carbon is found to be much smaller that that inferred in [48] for Hale-Bopp.

A very exhaustive work by Kelley & Wooden was recently published [34]. They review ground-based and space-based mid-infrared spectra of short-period comets, taken over the last 25 years. They inferred that the silicate content of short-period comets might be low relative to other species like amorphous carbon or FeS. They also claim that short period comets may contain crystalline silicates, as comets from the Oort cloud (high-temperature processes are needed for the formation of crystals).

In conclusion, silicates appear as the mean component of cometary dust in most works, although amorphous carbon is also considered important in some comets.

Hereafter, we will refer as m to the complex refractive index of any medium. The imaginary part of m is a measure of the absorption by the medium [7].

2.4 Size distribution of the particles

Suppose a sample made of spherical particles. The *number density distribution* $n(r)$ at a certain point is defined such as $n(r)dr$ is the fraction of particles with radii within $[r, r + dr]$ at that point. By definition, it is normalized to unity:

$$\int_{r_{min}}^{r_{max}} n(r)dr = 1. \tag{2.1}$$

For non-spherical grains, the same definition is valid just by considering the equivalent radius r_{eq} instead of r (see Sec. 3.1 for definition).

A commonly used model size distribution is the *power-law* [25]:

$$n(r) = \begin{cases} c(\delta, r_{min}, r_{max})r^{-\delta} & \text{if } r_{min} \leq r \leq r_{max}, \\ 0 & \text{otherwise.} \end{cases} \tag{2.2}$$

The constant $c(\delta, r_{min}, r_{max})$ can be obtained from the normalization condition (Eq. 2.1).

In real samples, the size of the grains usually varies through a very wide range of several orders of magnitude. For this reason, it is more convenient

to make plots using $\log r$ for the abscissa, instead of r. However, if we plot $n(r)$ as a function of $\log(r)$, we loose the simple interpretation of areas under the curve as relative number of particles in a certain range of sizes. A commonly adopted solution consists of using a new variable $N(\log r)$ such that $N(\log r)dlogr = n(r)dr$. The transformation between $N(\log r)$ and $n(r)$ is then given by $N(\log r) = \ln 10 r n(r)$.

In situ measurements of the dust size distribution functions are available for a few comets only. Thus, measurements by *Giotto* mission on Halley's Comet dust provided us with a size distribution that could be fitted to a power-law, with exponents varying between -2 and -3.4 approximately [44]. Stardust measurements gave a size distribution for Comet Wild 2 that could also be fitted to a power-law, resulting in a slightly less steep size distribution than that for Halley, with particles ranging from 0.01 μm to 1 mm [26].

On the other hand, remote sensing observations of dust tails, and their interpretation in terms of models based on dynamical grounds, resulted also in time-averaged size distributions that could be fitted to power-law functions with exponents generally within the range -3 to -3.5 (see, e.g., [31] and [20]).

Chapter 3

Theoretical basis on light scattering

3.1 Some basic definitions

Hereafter we will use the term *light* to refer to electromagnetic radiation of any wavelength, not only visible radiation.

When a solid particle is illuminated by a beam of light, some of the energy of the incident beam is absorbed (*absorption*) by the particle (and re-radiated in form of thermal emission), and some of it is scattered in all directions (*scattering*). If light is scattered at the same wavelength as the incident light, we will call the scattering *elastic scattering*. In the limiting case of scatterers much larger than the wavelength of the incident light, the scattering phenomenon can be divided into three clearly distinguishable processes: reflection on the surface of the scatterer particle, refraction through the particle and diffraction by the borders. Out of this case, these phenomena mix up in such a way that we can just talk about scattering.

In a typical scattering experiment, a cloud of particles is illuminated by a beam of light and an observer sees light scattered in a certain direction (see Fig. 3.1). The plane containing the directions of the incident beam and the observed scattered light is called the *scattering plane*. The angle θ formed by the directions of the observed scattered light and the incident beam is called the *scattering angle*, and the *phase angle* ϕ is defined as $\phi = \pi - \theta$. We call *optical axis* to the direction of the incident light.

In Fig. 3.2 we show the *coordinates system* to describe the components of the electric field vector of a beam of light. We chose an orthogonal right-handed system (see Eq. 3.1) for vectorial products to be calculated in the usual way [45]. For simplicity, we also imposed that one of the axes lies on

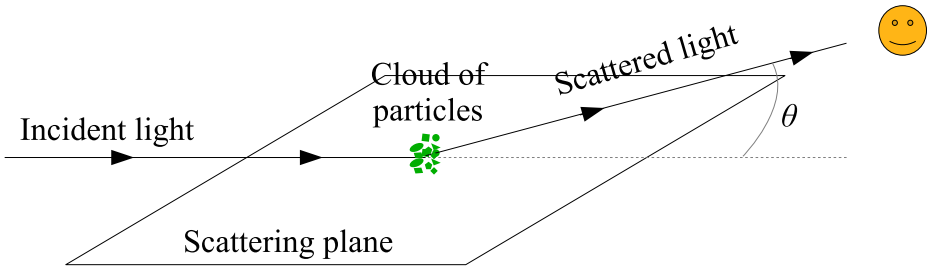

Figure 3.1: Sketch of a light scattering event. The scattering plane lies through the directions of the incident and observed scattering beams.

the scattering plane, another one is perpendicular to the plane, and the last one is obviously in the direction of propagation of light. The unit vectors defining this system are:

- $\hat{\mathbf{u}}$ in the direction (and sense) of the propagation of light,
- $\hat{\mathbf{r}}$ perpendicular to the scattering plane,
- $\hat{\mathbf{l}}$ through the scattering plane and perpendicular to $\hat{\mathbf{u}}$ and to $\hat{\mathbf{r}}$ in such a way that

$$\hat{\mathbf{r}} \times \hat{\mathbf{l}} = \hat{\mathbf{u}} \tag{3.1}$$

The axes choice is not unique, as seen in Fig. 3.2: vectors $\hat{\mathbf{l}}'$, $\hat{\mathbf{r}}'$, and $\hat{\mathbf{u}}$ also fulfill the constrain imposed in Eq. 3.1. Stokes parameters, flux, and the degree of linear and circular polarization (defined in Secs. 3.2.2 and 3.2.3) are independent of the choice of the system of reference. However, the signs of the components of the electric field vector do depend on that choice.

Let us now define some concepts related to the scatterers:

Suppose a particle of arbitrary shape with volume V. Then, the *equivalent radius*, r_{eq}, is defined as the radius of a spherical particle with the same volume.

$$r_{eq} = \sqrt[3]{\frac{3}{4\pi}V}. \tag{3.2}$$

Along the present thesis, we will usually refer to r_{eq} as the *size of a particle*.

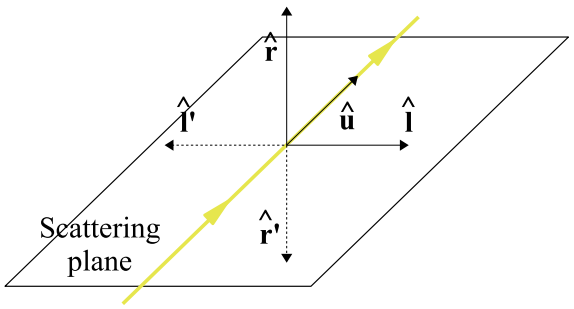

Figure 3.2: Orthogonal right-handed reference systems to describe the electric field. Two options are presented: ($\hat{\mathbf{l}}$,$\hat{\mathbf{r}}$,$\hat{\mathbf{u}}$) and ($\hat{\mathbf{l}}'$,$\hat{\mathbf{r}}'$,$\hat{\mathbf{u}}$). Although the signs of the components of the electric field vector depend on the choice we make, the observable magnitudes remain the same. The system we assume hereafter is the one plotted with solid lines ($\hat{\mathbf{l}}$,$\hat{\mathbf{r}}$,$\hat{\mathbf{u}}$).

The *equivalent size parameter* x of a particle is defined as:

$$x = \frac{2\pi r_{eq}}{\lambda}, \tag{3.3}$$

where λ is the wavelength of the incident light (and the scattered light, in case of elastic scattering). From the electromagnetic point of view, if we equally scale the size of the scatterers and the wavelength of the incident light without changing the shape of the particles, the resulting problem is completely equivalent to the original one, if the refractive index m of the scatterers is the same for the new wavelength. This is called the *scale invariance rule*, and a rigorous proof of it can be found in [50].

Let us introduce now the concept of *cross-section*. Imagine a large particle bombarded by a plain, uniform and constant stream of small solid projectiles. Let us call F the total energy (kinetic energy of the projectiles) crossing a surface perpendicular to the direction of propagation of the stream per unit time and per unit area. If σ is the projected area of the particle on the plane perpendicular to the incoming stream, then we have:

$$dE = F\sigma dt, \tag{3.4}$$

where dE is the sum of the energy of all projectiles interacting with the particle in a time interval dt. Now let us change the stream of small solid projectiles by a beam of light of any wavelength, still plane, uniform and constant, and let us assume that the particle does not absorb any radiation. By analogy, we define the *scattering cross-section* σ_{SCA} of the particle as:

$$dE = F\sigma_{SCA}dt. \tag{3.5}$$

It has dimensions of area. It can be interpreted as follows: the total energy scattered by the particle is equal to the energy of the incident radiation falling on a surface σ_{SCA} perpendicular to the direction of propagation.

We define the *geometrical cross-section* G of a particle as its projected area on a plane perpendicular to the direction of propagation of an incoming beam of light.

The extensions of these definitions to an ensemble of N particles can be done simply by adding:

$$\sigma_{SCA} = \sum_{k=1}^{N} \sigma_{SCA}^{k}, \tag{3.6}$$

σ_{SCA}^{k} being the scattering cross-section of the k-particle. Obviously, the same addition relation is valid for the geometrical sections.

Contrary to the intuitive interpretation, the scattering cross-section is not equal to the geometrical cross-section, either for a single particle or for an ensemble of particles. Based on this fact, it makes sense the definition of the ratio $Q_{SCA} = \frac{\sigma_{SCA}}{G}$: the *scattering factor*. This magnitude is dimensionless. Fig. 3.3 shows some examples of the ratio Q_{SCA}.

As stated before, not only scattering, but also absorption produces the extinction of light when it interacts with matter. In a way similar to the scattering cross-section, we define the *absorption cross-section* σ_{ABS} as the area such that the total energy absorbed by the particle is equal to the energy of the incident radiation falling on a surface σ_{ABS} perpendicular to the direction of propagation.

The *extinction cross-section* is just the sum of the scattering and absorption cross-sections. If we directly illuminate a sensor, and then we interpose a particle between the light source and the detector, the particle will cast a shadow of area σ_{EXT} on the detector. As

$$\sigma_{EXT} = \sigma_{SCA} + \sigma_{ABS}, \tag{3.7}$$

then:

$$Q_{EXT} = Q_{SCA} + Q_{ABS}, \tag{3.8}$$

where the *absorption factor* $Q_{ABS} = \frac{\sigma_{ABS}}{G}$ and the *extinction factor* $Q_{EXT} = \frac{\sigma_{EXT}}{G}$.

Both the cross-sections and the factors present a problem: they tell us about the particles of the cloud of scatterers, but do not contain any information on how many particles per unit volume are present in that cloud. For that purpose, we define the coefficients as the cross-sections per unit volume:

$$K_{SCA} = \lim_{\Delta V \to 0} \frac{\sigma_{SCA}}{\Delta V}, \tag{3.9}$$

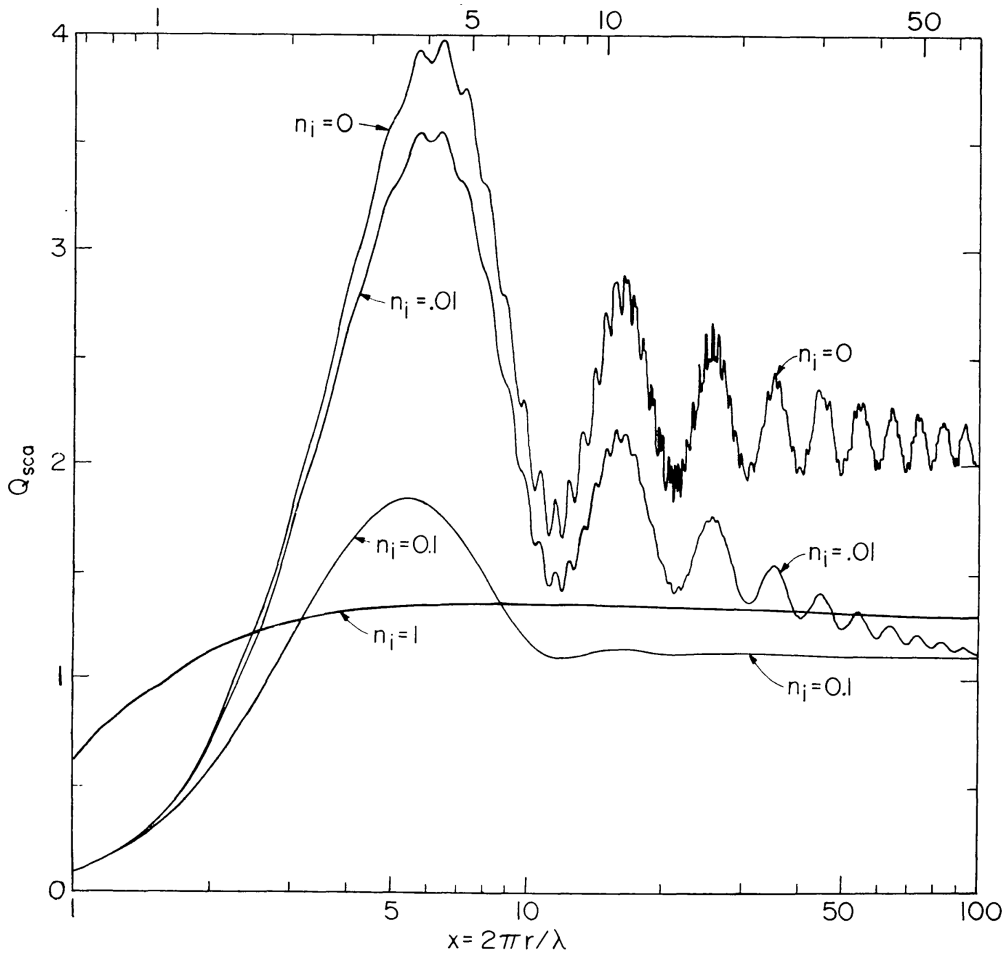

Figure 3.3: Scattering factor as a function of the size parameter of a single sphere. The real part of the complex refractive index is $Re(m) = 1.33$. Results are presented for four values of the imaginary part $Im(m)$. **Credit: Hansen & Travis 1974 [25].**

$$K_{ABS} = \lim_{\Delta V \to 0} \frac{\sigma_{ABS}}{\Delta V}, \tag{3.10}$$

$$K_{EXT} = K_{SCA} + K_{ABS} = \lim_{\Delta V \to 0} \frac{\sigma_{EXT}}{\Delta V}. \tag{3.11}$$

The cross sections and the factors are properties of every single particle of a sample or of the sample as a whole. The coefficients are properties of each point of the space.

The *single scattering albedo* $\tilde{\omega}$ of a particle is defined as:

$$\tilde{\omega} = \frac{\sigma_{SCA}}{\sigma_{EXT}} = \frac{Q_{SCA}}{Q_{EXT}} = \frac{K_{SCA}}{K_{EXT}}. \tag{3.12}$$

It varies from 0 to 1, and it gives information on how important is the scattering in the extinction. In this way, $\tilde{\omega} = 1$ means that all extinction is due to scattering and $\tilde{\omega} = 0$ means it is completely due to absorption.

3.2 Description of light

Radiation can be described at three levels. The most complete description consists of giving the electric (or magnetic) field that constitutes the electromagnetic wave. For visible radiation this field cannot be directly observed, because its oscillation period is much smaller than the typical duration of a measurement. Nevertheless, the fields contain all the information about the radiation.

Stokes parameters can be defined as functions of the components of the electric field (Eqs. 3.34 to 3.37). They consist of four quantities that can be determined experimentally. By this description, some of the information contained in the fields is lost (like the oscillation period of the fields), but all information on the flux and the degree of linear and circular polarization (see Sec. 3.2.3 for definitions) is kept, and the formalism is far more simple than that based on the fields.

The closest description to the directly observable quantities consists of an array of three magnitudes: flux, degree of linear polarization and degree of circular polarization. At this level of description, the information about the dominant direction of vibration of the fields (in case it exists) is lost.

3.2.1 Description of light in terms of the electric field vector

If we interpose a cloud of particles to a beam of light that propagates in vacuum, the electromagnetic waves propagating before and after the scattering event will be solutions of the Maxwell equations for an homogeneous and isotropic linear medium without any charge distribution, zero-conductivity, and the electric permitivity and magnetic permeability of vacuum. In this case, one solution is the monochromatic harmonic plane wave, that fulfills the following properties [7]:

1. The wave propagates at speed $c = \frac{1}{\sqrt{\epsilon_0 \mu_0}}$, where ϵ_0 and μ_0 are the electric permitivity and the magnetic permeability of vacuum, respectively.

2. Both the electric field vector $\mathbf{E}$ and the magnetic field vector $\mathbf{B}$ are perpendicular to the direction of propagation of the wave $\hat{\mathbf{u}}$ in all positions at all times.

3. Vectors **E** and **B** are perpendicular to each other in all points at all times.

4. The amplitudes of the electric and magnetic fields, E_0 and B_0, are related by $B_0 = \frac{1}{c}E_0$.

5. Vectors **E** and **B** are in phase in all points at all times.

Statements 2 to 5 can be summarized by the equation:

$$\hat{\mathbf{B}} = \frac{1}{c}\hat{\mathbf{u}} \times \hat{\mathbf{E}}. \tag{3.13}$$

This means that, in the case of scattering by a cloud of particles in vacuum, the magnetic field is univocally determined by the electric field. Hence, the incident beam is completely described by:

$$\mathbf{E} = a\mathrm{e}^{-i(kz-\omega t+\epsilon)}\hat{\mathbf{E}}, \tag{3.14}$$

with $\hat{\mathbf{E}}$ a real unit vector in the direction (and sense) of **E**, and ϵ the initial phase. We can also write the electric field as a function of its components in the reference frame defined in Fig. 3.2:

$$\begin{aligned} \mathbf{E}(\mathbf{r},t) &= E_l\hat{\mathbf{l}} + E_r\hat{\mathbf{r}}, \\ E_l &= a_l\mathrm{e}^{-i(kz-\omega t+\epsilon_l)}, \\ E_r &= a_r\mathrm{e}^{-i(kz-\omega t+\epsilon_r)}. \end{aligned} \tag{3.15}$$

3.2.2 Description of light in terms of the Stokes parameters

In 1852 George Gabriel Stokes introduced the parameters named after him. The goal of these quantities was to offer a handy way of describing light.

The *Stokes parameters for monochromatic light* can be defined as functions of the components of the electric field vector:

$$I = E_lE_l^* + E_rE_r^*, \tag{3.16}$$
$$Q = E_lE_l^* - E_rE_r^*, \tag{3.17}$$
$$U = E_lE_r^* + E_rE_l^*, \tag{3.18}$$
$$V = i\left(E_lE_r^* - E_rE_l^*\right). \tag{3.19}$$

We call $(I, Q, U, V)^t$ the *Stokes vector*, where t means transpose.

Substituting the components of the electric field (Eq. 3.15) in Eqs. 3.16 to 3.19, we can alternatively write the Stokes parameters as:

$$I = a_l^2 + a_r^2, \tag{3.20}$$
$$Q = a_l^2 - a_r^2, \tag{3.21}$$
$$U = 2a_l a_r \cos(\epsilon_l - \epsilon_r), \tag{3.22}$$
$$V = 2a_l a_r \sin(\epsilon_l - \epsilon_r). \tag{3.23}$$

In Fig. 3.4, the polarization ellipse is shown. Axes l and r are defined in the direction and sense of $\hat{\mathbf{l}}$ and $\hat{\mathbf{r}}$ respectively. Light travels into the paper, and the ellipse represents the trajectory of the tip of the electric field vector through time at a fixed position. Inclination is given by angle χ, which is measured by bringing the positive part of axis l to the mayor semi-axis of the ellipse anticlockwise. Hence, $0 \leq \chi < \pi$. The angle β contains the information on the eccentricity of the ellipse and the sense of the polarization. It remains within the interval $-\pi/4 \leq \beta < \pi/4$. The modulus of $\tan\beta$ can be obtained as the ratio between the minor and the major axes of the ellipse. The sign of β is determined depending on the sense of rotation of the electric field vector. Along the present study, we do not need to establish a criterion to set the correspondence between the sense of rotation of $\mathbf{E}$ and the sign of β.

The Stokes parameters can also be written as functions of the quantities that define the polarization ellipse [28] (see Fig. 3.4) as follows:

$$I = a^2, \tag{3.24}$$
$$Q = a^2 \cos 2\beta \cos 2\chi, \tag{3.25}$$
$$U = a^2 \cos 2\beta \sin 2\chi, \tag{3.26}$$
$$V = a^2 \sin 2\beta, \tag{3.27}$$

where $a^2 = a_l^2 + a_r^2$. Suppose that the polarization ellipse is oriented with its axes in the directions of the reference axes l and r (see Fig. 3.5). Then, a can be understood as the hypotenuse of the right triangle formed by the semi-axes of the ellipse. When rotating the reference axes by an angle i_{rot} anticlockwise to (l', r'), the change of the electric field vector components is like this:

$$E_{l'} = E_l \cos i_{rot} + E_r \sin i_{rot} \tag{3.28}$$
$$E_{r'} = -E_l \sin i_{rot} + E_r \cos i_{rot}. \tag{3.29}$$

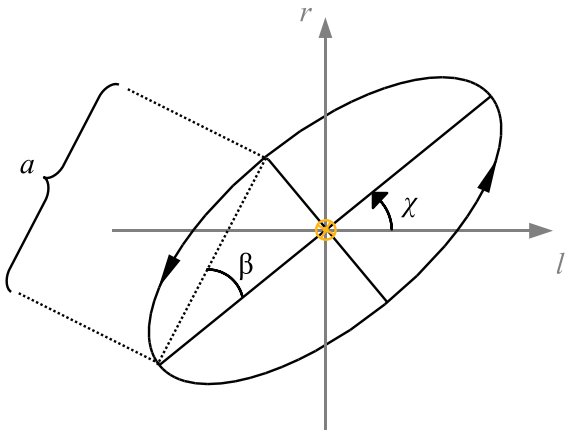

Figure 3.4: Polarization ellipse of a beam of light that propagates into the paper. The ellipse represents the trajectory of the tip of the electric field vector through time at a fixed position. The reference plane is that formed by the axis l and the direction of propagation of light. The inclination of the semi-major axis of the ellipse with regard to the reference plane is χ, while β determines the eccentricity.

Therefore, the amplitudes of the new electric field vector components are:

$$a_{l'} = a_l \cos i_{rot} + a_r \sin i_{rot} \tag{3.30}$$

$$a_{r'} = -a_l \sin i_{rot} + a_r \cos i_{rot}. \tag{3.31}$$

Then, $a'^2 = a^2$. We have deduced that a do not depend on the orientation of the reference plane of the polarization ellipse, and as a consequence, it is always the hypotenuse of the right triangle formed by the semi-axes of the ellipse (see Fig. 3.4). Hence, according to Eq. 3.24, I is independent of the scattering plane too, and it is a measure of the size of the polarization ellipse.

Eqs. 3.24 to 3.27 give us a geometrical interpretation of the Stokes parameters: I is a measure of the size of the polarization ellipse. The sign of V is telling us whether the electric field vector is rotating to the right or to the left. The magnitude of V informs us about the elongation of the ellipse. $V = 0$ corresponds to the maximum elongation, when the ellipse becomes a line. While increasing the modulus of V the elongation disappears until the ellipse becomes a circle for $|V| = I$. On the other hand, U vanishes for $\chi = 0, \pi/2$, and achieves its extreme values for $\chi = \pm\pi/4$, while the opposite happens to Q. Extreme (either positive or negative) values of Q (or equivalently values of U close to zero) are typical of polarization ellipses with their major axis close to the direction of the scattering plane or to its normal.

When values of Q are close to zero, the major axis of the ellipse is close to any of the middle positions between $\hat{\mathbf{l}}$ and $\hat{\mathbf{r}}$. When U tends to zero, the axes of the ellipse are close to coincide with the axes of the reference system l and r.

An obvious property of the Stokes parameters from their definition (Eqs. 3.16 to 3.19) is:

$$I = \sqrt{Q^2 + U^2 + V^2}. \tag{3.32}$$

In this work we are interested in *non-monochromatic light*, since the spectra of stars are approximately a black body continuum. For a non-monochromatic beam of light (composed of plane waves of several frequencies), the electric field can be written as a plane wave with amplitude and initial phase variable in time (see Eq. 3.33) [4]. In this case, the Stokes parameters, as defined in Eqs. 3.16 to 3.19, are variable in time. To avoid this, we now define the *Stokes parameters for non-monochromatic light* as follows. If the components of the electric field vector are given by:

$$\begin{aligned} E_l(t) &= a_l(t)\, \mathrm{e}^{-i(kz-\omega t+\epsilon_l(t))}, \\ E_r(t) &= a_r(t)\, \mathrm{e}^{-i(kz-\omega t+\epsilon_r(t))}, \end{aligned} \tag{3.33}$$

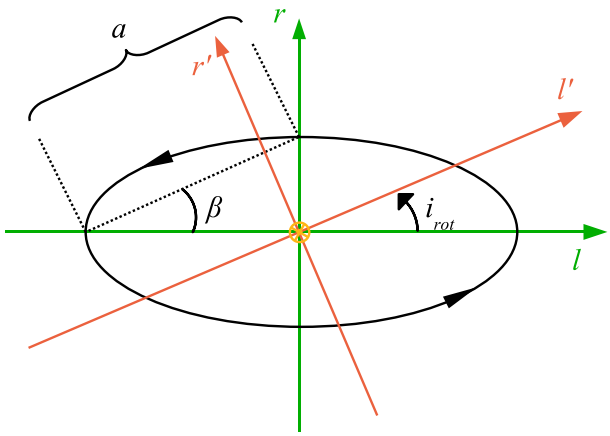

Figure 3.5: Polarization ellipse (light travelling into the paper) oriented with its axes in the directions of the reference axes l and r. In such an orientation, the hypotenuse of a right triangle formed by the semi-axes of the ellipse is equal to a, where $a^2 = I$, with I written in the axes (l, r). Another system of axes (l', r') is plotted rotated an angle i_{rot} anticlockwise with respect to (l, r).

the Stokes parameters are calculated as the time average of those defined in Eqs. 3.16 to 3.19:

$$I(t) = \langle E_l(t) E_l^*(t) + E_r(t) E_r^*(t) \rangle, \tag{3.34}$$
$$Q(t) = \langle E_l(t) E_l^*(t) - E_r(t) E_r^*(t) \rangle, \tag{3.35}$$
$$U(t) = \langle E_l(t) E_r^*(t) + E_r(t) E_l^*(t) \rangle, \tag{3.36}$$
$$V(t) = i\langle (E_l(t) E_r^*(t) - E_r(t) E_l^*(t)) \rangle, \tag{3.37}$$

or, equivalently:

$$I = \langle a_l(t)^2 + a_r(t)^2 \rangle, \tag{3.38}$$
$$Q = \langle a_l(t)^2 - a_r(t)^2 \rangle, \tag{3.39}$$
$$U = 2\langle a_l(t) a_r(t) \cos(\epsilon_l(t) - \epsilon_r(t)) \rangle, \tag{3.40}$$
$$V = 2\langle a_l(t) a_r(t) \sin(\epsilon_l(t) - \epsilon_r(t)) \rangle, \tag{3.41}$$

or:

$$I = \langle a^2(t) \rangle, \tag{3.42}$$
$$Q = \langle a^2(t) \cos 2\beta(t) \cos 2\chi(t) \rangle, \tag{3.43}$$
$$U = \langle a^2(t) \cos 2\beta(t) \sin 2\chi(t) \rangle, \tag{3.44}$$
$$V = \langle a^2(t) \sin 2\beta(t) \rangle. \tag{3.45}$$

In all cases the symbols $\langle\rangle$ mean average over a time much larger than $2\pi/\omega$. The definition for the monochromatic light is a particular case of the one for non-monochromatic situation, so we can take the latter as the general definition.

Light with constant a_l/a_r and $(\epsilon_l(t) - \epsilon_r(t))$ is called *totally polarized light*. For this kind of light, the elongation, the inclination and the sense of the polarization ellipse remain constant, but its size may change. For totally polarized light Eqs. 3.42 to 3.45 transform into:

$$I = \langle a^2(t) \rangle, \tag{3.46}$$
$$Q = \langle a^2(t) \rangle \cos 2\beta \cos 2\chi, \tag{3.47}$$
$$U = \langle a^2(t) \rangle \cos 2\beta \sin 2\chi, \tag{3.48}$$
$$V = \langle a^2(t) \rangle \sin 2\beta. \tag{3.49}$$

As seen in Eqs. 3.46 to 3.49, Stokes parameters do not remain constant in general for totally polarized light, but the ratio of any pair of them does. Regarding the polarization ellipse, for totally polarized light it remains constant in shape and orientation, but its size may vary. If the amplitudes and the

initial phases remain constant, the size of the ellipse will remain constant too (monochromatic light). When no correlation exists neither between the amplitudes nor the initial phases of the components of the electric field, light is called *totally unpolarized light* or *natural light*: $(I, Q, U, V)^t = (1, 0, 0, 0)^t$. In this case, the polarization ellipse is not defined in eccentricity, nor in inclination, nor in sense, nor in size. Ratios between any pair of Stokes parameters are not defined either. Between both of these extreme cases (totally polarized and totally unpolarized light), we find *partially polarized light*, for which a stable average polarization ellipse exists. In this case, ratios between pairs of Stokes parameters vary in time, but they are distributed around a stable average.

For the general case of non-monochromatic light the property given in Eq. 3.32 is not always valid. A valid property for the general case is (see [28]):

$$I \geq \sqrt{Q^2 + U^2 + V^2}. \tag{3.50}$$

Another general property, and even more important, is the *additivity of the Stokes parameters* [28]: If several incoherent light beams (with no correlated phases) income on the same point at once, the observed Stokes parameters at that point will be the summation of the Stokes parameters of all beams.

3.2.3 Description of light in terms of flux and degrees of polarization

Suppose a point source of light emitting radiation in all directions. Two magnitudes are usually defined to measure how bright the source is:

- *Flux*: Imagine that we place a detector of elemental area dS_{det} in a point P at a certain distance R of the source, with its surface perpendicular to the direction of light. Suppose that an elemental amount of energy dE comes onto the detector in an elemental time interval dt. Then, the flux Φ at P is defined by:

$$dE = \Phi dS_{det} dt. \tag{3.51}$$

- *Intensity*: Let us now adopt the same assumptions as in the definition of the flux, and consider as well that the solid angle subtended by the detector is $d\Omega_{det}$. Then, the intensity I_n is defined by:

$$dE = I_n dS_{det} d\Omega_{det} dt. \tag{3.52}$$

Intensity and flux have the same dimensions. A difference between them is that the intensity does remain constant along the path of light in a medium without absorption, or scattering, or emission (vacuum, for instance). The reason is that when moving far away from the source along the direction of light, the energy that the detector receives per unit time and per unit area decreases at the same rate as the solid angle subtended by the source. Let us call W_0 the energy emitted by the light source per unit time in all directions. Then, the energy propagating per unit surface and per unit time at a distance R from the source is $\frac{W_0}{4\pi R^2}$. Since the solid angle subtended by the detector can be written as $d\Omega_{det} = \frac{dS_{det}}{R^2}$, the intensity is given by $I_n = \frac{W_0}{4\pi dS_{det}^2 dt}$. All factors of the right side of the equation are constant, so the intensity is constant.

In contrast, the flux measured at different distances from the source may be different. Let us assume a certain solid angle $d\Omega$ with its origin in the source. As light travels in straight lines, the energy of the light propagating into the cone defined by $d\Omega$ cannot cross the wall to get out of it, and the energy from the outside cannot enter. Let us assume now that the medium of propagation does not absorb, or scatter, or emit radiation. Then, the energy crossing an elemental surface dS per unit time will be the same at all distances, but if $R_2 > R_1$, dS_2 will be larger than dS_1 ($dS = R^2 d\Omega$). Hence, the energy travelling per unit surface and per unit time decreases while moving far from the source. On the other hand the surface of the detector dS_{det} is constant, so according to Eq. 3.51 the flux decreases while moving far from the source along the direction of light. Fig. 3.6 illustrates the difference between flux and intensity.

Along the present work, not intensity, but flux will be used to describe light.

As defined in Eq. 3.34, the first Stokes parameter I is proportional to the flux Φ for a plane harmonic monochromatic wave.

The *degree of polarization* of a beam of light is defined as:

$$DP = \frac{\sqrt{Q^2 + U^2 + V^2}}{I}. \tag{3.53}$$

For totally polarized light $DP = 1$ (Eq. 3.32) and it is smaller than 1 for any other case (Eq. 3.50).

We define the *degree of linear polarization* of a beam of light as:

$$DLP = \frac{\sqrt{Q^2 + U^2}}{I}. \tag{3.54}$$

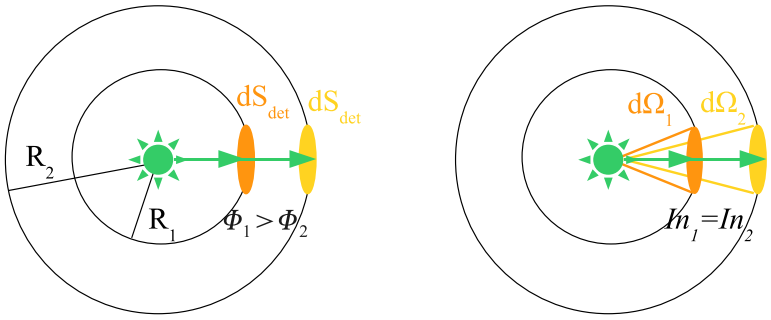

Figure 3.6: Light propagating from a point source through a medium without absorption, or scattering, or emission. A detector with a fixed area dS_{det} is located at two different distances from the source. Flux is represented on the left panel. As the energy propagating through a spherical shell per unit surface and per unit time is smaller for larger distances to the source, and the surface of the detector remains constant, the flux decreases while increasing the distance (Eq. 3.51). On the right panel the intensity is represented (see Eq. 3.52 for definition). It is constant along the path of light because while increasing the distance to the source, the energy propagating per unit area and per unit time decreases at the same rate as the solid angle subtended by the detector.

We refer as the *extended degree of linear polarization* to:

$$EDLP = \frac{-Q}{I} = \frac{I_r - I_l}{I_r + I_l}, \tag{3.55}$$

with $I_l = (I+Q)/2 = E_l^2$ and $I_r = (I-Q)/2 = E_r^2$. In case that $U = 0$, this magnitude in absolute value coincides with the DLP, but it contains some more information: it is positive when the longest axis of the polarization ellipse is close to the perpendicular to the scattering plane, and negative when it is close to be parallel.

The *degree of circular polarization* is defined as:

$$DCP = \frac{V}{I}. \tag{3.56}$$

For totally polarized light, we deduce from Eqs. 3.46 and 3.49 that the sign of the DCP is equal to the sign of β. It is zero when the ellipse becomes a line, i.e., when $DLP = 1$. The DLP will vanish when the ellipse becomes a circle, i.e., $DCP = 1$.

We refer as *circular polarization* (CP hereafter), to the property of light with a non-zero DCP. The DCP is the magnitude that accounts for the CP.

We say that light is left-handed or right-handed circularly polarized when it possesses a positive or negative DCP respectively (or vice versa, depending on the criterion). There is no need in this work for establishing a criterion of correspondence between (left-handed,right-handed) circular polarization and (positive,negative) DCP.

3.3 Change of the plane of reference

Let us consider totally polarized light along the present section.

In Secs. 3.2.1 to 3.2.3, the scattering plane is assumed as the plane of reference. Changing the scattering plane would lead to a change in the components of the electric field E_l and E_r, and equivalently, a change of the parameters defining the polarization ellipse (Fig. 3.4). As a consequence, the Stokes parameters may change, because they are defined as functions of the components of the electric field vector (Eqs. 3.34 to 3.37) and also as functions of the parameters defining the polarization ellipse (Eqs. 3.42 to 3.45). Fig. 3.7 shows a polarization ellipse (light travelling into the paper), along with two systems of reference corresponding to the parallel and perpendicular axes of two scattering planes. Rotating the axes by an angle i_{rot} anticlockwise produces a change in the orientation of the ellipse, but the size and the shape remain the same. As I depends on the size of the polarization ellipse only, and V depends on the size and the shape (see Sec. 3.2.2), these two Stokes parameters remain constant when rotating the reference plane around the direction of light. Parameters Q and U do change, because they depend on χ:

$$Q' = a^2 \cos 2\beta \cos 2\chi' = Q \cos 2i_{rot} + U \sin 2i_{rot}, \tag{3.57}$$

$$U' = a^2 \cos 2\beta \sin 2\chi' = -Q \sin 2i_{rot} + U \cos 2i_{rot}. \tag{3.58}$$

Thus, the transformation can be written as:

$$\begin{pmatrix} I' \\ Q' \\ U' \\ V' \end{pmatrix} = \begin{pmatrix} 1 & 0 & 0 & 0 \\ 0 & \cos 2i_{rot} & \sin 2i_{rot} & 0 \\ 0 & -\sin 2i_{rot} & \cos 2i_{rot} & 0 \\ 0 & 0 & 0 & 1 \end{pmatrix} \begin{pmatrix} I \\ Q \\ U \\ V \end{pmatrix}. \tag{3.59}$$

Although two Stokes parameters change when rotating the scattering plane, the flux, the DLP and the DCP remain constant. For the flux and the DCP it is obvious: they only depend on constant parameters I and V. The DLP remains constant because $Q^2 + U^2$ does not depend on χ (see Eqs. 3.47 and 3.48).

3.4 Some general hypotheses

To set the scenario of the processes we are going to study, we state the following hypotheses:

Vacuum hypothesis: We are interested in studying the scattering of light by dust particles in the comae of comets. In these systems the density of the gaseous medium that surrounds the scatterers is supposed to be close to zero [10]. As a consequence, for our calculations we can assume that radiation propagates through vacuum, interacting with dust particles, but never with atoms or molecules of gas.

Natural incident light hypothesis: Throughout this work, we will consider the light coming from the source to be *natural light*, i.e., completely unpolarized. This hypothesis is based on the fact that solar light is unpolarized (see, e.g., [12]).

Monochromatic plane harmonic wave hypothesis: After Fourier's theorem (see, e.g. [7]), any incident light can be written as the sum of a number of monochromatic harmonic waves. Moreover, because of the linearity of the

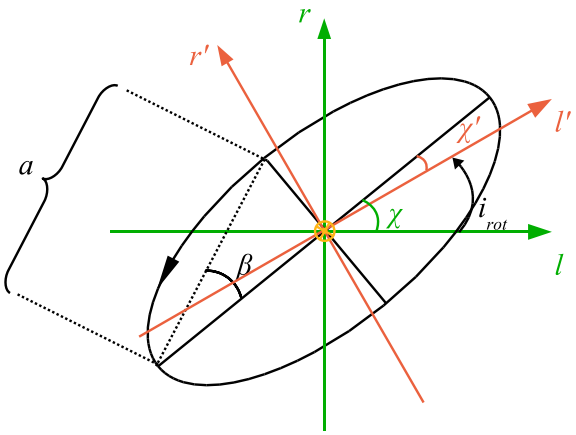

Figure 3.7: Polarization ellipse (light travelling into the paper), along with two systems of axes. The system (l', r') is rotated an angle i_{rot} anticlockwise with respect to (l, r). The orientation of the polarization ellipse changes when using a different system of reference, but neither the shape nor the size. This means that changing the plane of reference affects Q and U, but neither I nor V change.

Maxwell equations, the total scattered wave will be the sum of the individual scattered waves corresponding to all components of the incident wave. By joining both statements we conclude that we can reduce our study to incident monochromatic harmonic waves. Furthermore, as comets (scatterers) use to be at distances of the order of the AU ($1AU \approx 1.5 \cdot 10^{11}\ m$) from the Sun (source) and from the Earth (observer), and we are dealing with visible light, waves can be considered plane for both the incident and the scattered beams in the comet. In summary, we can simplify our work by assuming monochromatic plane harmonic waves.

Elastic scattering hypothesis: Hereafter, we will consider that the scattering is elastic (see Sec. 3.1 for definition). For a dielectric material, the tangential component of the electric field is continuous in the interface between vacuum and the particle [7], what implies that the wavelength of the light coming onto the particle is the same as that of the scattered light. As cometary dust grains are mainly formed by dielectric materials (see Sec. 2.3), assuming elastic scattering is reasonable.

3.5 The light scattering problem

In this section we present a summary of the widely used techniques for solving the *light scattering problem*, i.e., for obtaining the properties of the scattered light from the properties of the incident light and those of the scatterers.

When $x << 1$, we say that particles are in the *Rayleigh domain*. In that regime the DCP produced by the scatterers over the scattered light in a single scattering event tends to zero. A complete study of the scattering problem in the Rayleigh domain can be found in [35].

In the general case of any size parameter, there are two approaches to the problem:

1. To think of a particle as a spatial discontinuity in the refractive index of the medium and solve the Maxwell equations inside and outside the scatterers.

2. To think of a particle as an ensemble of charges affected by the incident field and calculate the radiated field.

Based on the first approach, a number of solutions of the scattering problem have been obtained (just for scatterers of simple shapes):

The analytical solution for isotropic and homogeneous spheres was achieved by Lorenz in 1890 [39], and independently by Love in 1899 [40], Mie in 1908

[47] and Debye in 1909 [11]. A solution for optically active spheres can be found in Bohren, 1974 [1]. In 1955, Wait gave a solution for homogeneous and isotropic infinite cylinders [70], which was extended by Bohren in 1978 [2] for the case of optically active cylinders. Finally, Oguchi in 1973 [58] and Asano & Yamamoto in 1975 [59] found a general solution for homogeneous and isotropic spheroids.

Also based on the first approach, two more advanced methods were developed. The first one is the *T-matrix* technique [51], which is devoted to the calculation of the scattering matrix of rotationally symmetrical particles, either in a fixed orientation or randomly oriented. There is a maximum size parameter of particles for which the code can be compiled. The superposition theorem makes it possible to solve the problem for aggregates of spheres with the T-matrix method [42]. This is a computationally fast algorithm that calculates accurate results because it makes the orientation average analytically. However, it is not able to perform calculations for asymmetrical compact particles, and there is an upper limit to the size of the grains it can deal with. The second advanced technique is the *Finite Difference in Time Domain (FDTD)* method [67], which numerically solves the Maxwell equations by using a finite differences technique. It can calculate the scattering matrix of particles of any shape and size, but it is much slower than the T-matrix. Its computational requirements (CPU time and memory) rise when increasing the size of the particles and the accuracy of the calculations, and in case we need an orientation average, it must be done numerically.

Finally, the *Discrete Dipole Approximation (DDA)* [16] follows the second approach. It makes a summation of the fields of the radiant dipoles taking into account the interaction between them. It is valid for grains of any shape and any size, but it is very expensive in terms of computational resources. The CPU time increases so fast when increasing the size parameter of the particles, that the practical size limitation of this method is comparable to that of T-matrix. Another drawback of DDA is that the orientation average is made numerically, what implies a lack of accuracy compared to T-matrix.

3.6 The light scattering matrix

Although we do not have an analytical solution for all shapes of the scatterers, we can deduce a general formalism for the scattering problem.

3.6.1 Definition of the light scattering matrix

Let us assume that the distance R from a particle to the observer of the scattered light is much larger than the maximum length in the scatterer (far field zone approximation), and also much larger than the wavelength. Then, there exists the linear relation between the electric field vectors of both the incident and the scattered waves in a single scattering event by a single particle [50]:

$$\begin{pmatrix} E_l^{sca} \\ E_r^{sca} \end{pmatrix} = \frac{\mathrm{e}^{-ikR+i\epsilon_0}}{ikR}\mathbf{S}\left(\theta,\varphi\right)\begin{pmatrix} E_l^{inc} \\ E_r^{inc} \end{pmatrix}, \tag{3.60}$$

where (R,θ,φ) are the spherical coordinates of the position of the observer, the origin being the scatterer cloud and the incident light beam travelling in the positive sense of the direction of axis z (see Fig. 3.8).

$\boldsymbol{S}$ is the so called *amplitude matrix*. It is a 2×2 matrix that depends on the direction of the scattered beam, the wavelength of the incident beam, the orientation of the scatterer particle and some intrinsic properties of it (size, shape and complex refractive index).

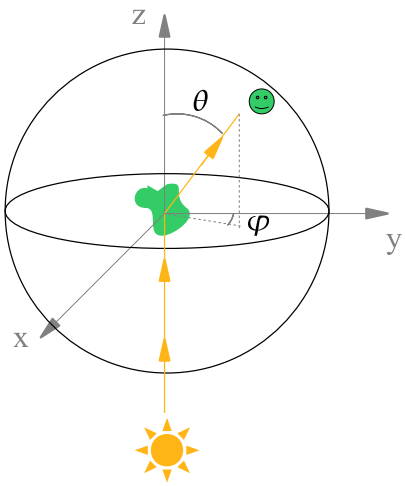

Figure 3.8: Spherical coordinates system assumed to describe the scattering event.

From the relation between the incident and scattered fields (Eq. 3.60), we can deduce the relation between the Stokes parameters of the incident

and scattered beams:

$$\mathbf{I^{sca}} = \frac{1}{k^2 R^2}\mathbf{F^p}\mathbf{I^{inc}}, \tag{3.61}$$

$\mathbf{F^p}$ being a 4×4 matrix called *scattering matrix*, given by:

$$F_{11}^p = \frac{1}{2}\left(|S_{11}|^2 + |S_{12}|^2 + |S_{21}|^2 + |S_{22}|^2\right), \tag{3.62}$$
$$F_{12}^p = \frac{1}{2}\left(|S_{11}|^2 - |S_{12}|^2 - |S_{21}|^2 + |S_{22}|^2\right), \tag{3.63}$$
$$F_{13}^p = \mathrm{Re}\left(S_{11}S_{12}^* + S_{22}S_{21}^*\right), \tag{3.64}$$
$$F_{14}^p = \mathrm{Im}\left(S_{11}S_{12}^* - S_{22}S_{21}^*\right), \tag{3.65}$$
$$F_{21}^p = \frac{1}{2}\left(|S_{11}|^2 + |S_{12}|^2 - |S_{21}|^2 - |S_{22}|^2\right), \tag{3.66}$$
$$F_{22}^p = \frac{1}{2}\left(|S_{11}|^2 - |S_{12}|^2 - |S_{21}|^2 + |S_{22}|^2\right), \tag{3.67}$$
$$F_{23}^p = \mathrm{Re}\left(S_{11}S_{12}^* - S_{22}S_{21}^*\right), \tag{3.68}$$
$$F_{24}^p = \mathrm{Im}\left(S_{11}S_{12}^* + S_{22}S_{21}^*\right), \tag{3.69}$$
$$F_{31}^p = \mathrm{Re}\left(S_{11}S_{21}^* + S_{22}S_{12}^*\right), \tag{3.70}$$
$$F_{32}^p = \mathrm{Re}\left(S_{11}S_{21}^* - S_{22}S_{12}^*\right), \tag{3.71}$$
$$F_{33}^p = \mathrm{Re}\left(S_{11}S_{22}^* + S_{12}S_{21}^*\right), \tag{3.72}$$
$$F_{34}^p = \mathrm{Im}\left(S_{11}S_{22}^* + S_{21}S_{12}^*\right), \tag{3.73}$$
$$F_{41}^p = \mathrm{Im}\left(S_{21}S_{11}^* + S_{22}S_{12}^*\right), \tag{3.74}$$
$$F_{42}^p = \mathrm{Im}\left(S_{21}S_{11}^* - S_{22}S_{12}^*\right), \tag{3.75}$$
$$F_{43}^p = \mathrm{Im}\left(S_{22}S_{11}^* - S_{12}S_{21}^*\right), \tag{3.76}$$
$$F_{44}^p = \mathrm{Re}\left(S_{22}S_{11}^* - S_{12}S_{21}^*\right). \tag{3.77}$$

The element F_{11} is usually called the *phase function*.

The scattering matrix depends on the same variables as the amplitude matrix. Obviously, as well as the amplitude matrix, the scattering matrix is dimensionless. We would also like to remark that Eq. 3.61 is valid just for a single scattering event by a single particle, as it was Eq. 3.60, from which it is derived.

Once we set the scattering plane, we can define it as the yz plane, so that we can set $\varphi = 0$ (Fig. 3.8). Then, the elements F_{ij}^p of the scattering matrix will depend on θ for that scattering plane, and θ is what we defined as the scattering angle in Fig. 3.1. Based on this, from now on we will write the elements of the scattering matrix as $F_{ij}^p(\theta)$. However, it is important to remark that in general the scattering matrix will be different for different scattering planes. One exception for this is the case that the sample of

scatterers is a cloud of randomly oriented particles. Then, all planes are equivalent, so the scattering matrix depends on the scattering angle, but not on φ.

So far, we have just talked about scattering by one single particle, but in real systems we find clouds of dust where lots of particles of different shapes, sizes, compositions and orientations are mixed up. Thanks to the additivity of the Stokes parameters (see Sec. 3.2.2), the formalism for a cloud of scatterers is directly derived from the formalism for a single particle: the scattering matrix of an ensemble of particles in conditions of single scattering can be written as the sum of the scattering matrices of the single particles (Eq. 3.79). Single scattering conditions must be imposed because otherwise Eq. 3.61 would not be fulfilled, and that equality is used in the proof presented in Eq. 3.78 (where marked with $*$):

$$\mathbf{I^{sca}} = \sum_{k=1}^{N} \mathbf{I_k^{sca}} \overset{*}{=} \sum_{k=1}^{N} \left(\mathbf{F_k^p I^{inc}}\right) = \left(\sum_{k=1}^{N} \mathbf{F_k^p}\right) \mathbf{I^{inc}} = \mathbf{F I^{inc}}. \tag{3.78}$$

Subindex k means the k-particle of the ensemble. According to Eq. 3.78 the scattering matrix $\mathbf{F}$ of an ensemble of N particles is given by:

$$\mathbf{F} = \sum_{k=1}^{N} \mathbf{F_k^p}. \tag{3.79}$$

For the particular case of natural incident light, $\mathbf{I^{inc}} = (I^{inc}, 0, 0, 0)^t$, just by using Eq. 3.78 in Eq. 3.56 we see that the DCP can be obtained as:

$$DCP\left(\theta\right) = \frac{F_{41}\left(\theta\right)}{F_{11}\left(\theta\right)}, \tag{3.80}$$

and the $EDLP$, from Eq. 3.55, is:

$$EDLP\left(\theta\right) = -\frac{F_{21}\left(\theta\right)}{F_{11}\left(\theta\right)}. \tag{3.81}$$

Usually, when more than one kind of particles (shape, size or composition) is present in a cloud of scatterers and the scattering matrix of every single type of particles is known, an *averaged scattering matrix* is used to calculate the properties of the scattered light given the Stokes parameters of the incident light, in conditions of single scattering. The reason for this is derived from Eq. 3.78: The scattering matrix of the whole sample $\mathbf{F_{tot}}$ is the sum of the scattering matrices of all particles in the sample. By using the average, we are actually taking $\frac{1}{N}\mathbf{F_{tot}}$ as the scattering matrix of the sample.

That introduces an error factor $\frac{1}{N}$ in the calculation of the Stokes parameters (Eq. 3.61), but it makes no difference when calculating the DLP, $EDLP$ or DCP, as defined in Eqs. 3.54 to 3.56. In conditions of multiple scattering the scattering matrix of the sample is not simply the sum of the scattering matrices of the individual grains, so the averaged scattering matrix is not a good approximation to solve the scattering problem.

3.6.2 Some properties of the light scattering matrix

Let us suppose a scattering experiment with a single scatterer in a certain orientation. We call the *reciprocal experiment* that in which the source and the observer have been interchanged, but the particle has remained the same. The reciprocal experiment can also be understood in the opposite sense: instead of interchange the source by the observer, we can reorient the grain in such a way that the experiment is the equivalent to the reciprocal. In such a case we say that we have substituted the particle by its *reciprocal particle*.

Reciprocity theorem [50]: Suppose that the conductivity, the electric permitivity and the magnetic permeability are symmetrical matrices for both the material the scatterer is made of and the propagation medium. Then, if the amplitude matrix for a scattering experiment in a certain configuration is $\mathbf{S}$, it will be $[\mathbf{S}]^{-t}$ for the reciprocal experiment. In other words, when changing a experiment by its reciprocal, the amplitude matrix is transformed as:

$$\begin{pmatrix} S_{11} & S_{12} \\ S_{21} & S_{22} \end{pmatrix} \longrightarrow \begin{pmatrix} S_{11} & -S_{21} \\ -S_{12} & S_{22} \end{pmatrix}. \tag{3.82}$$

As we assumed that the propagation medium is vacuum (Sec. 3.1), we are always fulfilling half of the hypothesis of the theorem (the part regarding the propagation medium). The other half (symmetrical matrices for the conductivity, the electrical permitivity and the magnetic permeability of the scatterer) means that optically active materials are excluded from the theorem.

A transformation in the amplitude matrix directly leads to a transformation of the scattering matrix through Eqs. 3.62 to 3.77. Let us call REC the application transforming the scattering matrix $\mathbf{F}$ of an scattering experiment into the scattering matrix $\mathbf{F}^{rec}$ of the reciprocal experiment.

The theorem cannot be extended for scattering samples made of many particles. By considering the additivity of the scattering matrices (Eq. 3.79):

$$\mathbf{F^{rec}} = \sum_{k=1}^{N} \mathbf{F_k^{rec}} = \sum_{k=1}^{N} REC\left(\mathbf{F_k}\right) \neq REC\left(\sum_{k=1}^{N} \mathbf{F_k}\right) = REC\left(\mathbf{F}\right), \tag{3.83}$$

because REC is not a linear application in the space of 4×4 real matrices. So in general, the fact that the reciprocity theorem is valid for every single particle of a sample does not assure that it is valid for the whole cloud.

We say that a sample has *reciprocity symmetry* if for each particle of the sample we can find one (only one) that is the reciprocal of the first.

Suppose a scattering event by a particle. We call the *mirror particle* of the first one to the specular image of it with respect to the scattering plane. If in a sample we change all particles by their mirror particles, the scattering matrix transforms as follows:

$$\begin{pmatrix} F_{11} & F_{12} & F_{13} & F_{14} \\ F_{21} & F_{22} & F_{23} & F_{24} \\ F_{31} & F_{32} & F_{33} & F_{34} \\ F_{41} & F_{42} & F_{43} & F_{44} \end{pmatrix} \longrightarrow \begin{pmatrix} F_{11} & F_{12} & -F_{13} & -F_{14} \\ F_{21} & F_{22} & -F_{23} & -F_{24} \\ -F_{31} & -F_{32} & F_{33} & F_{34} \\ -F_{41} & -F_{42} & F_{43} & F_{44} \end{pmatrix}. \tag{3.84}$$

The proof is simple: Suppose that initially we have a certain scattering problem. When changing all particles by their mirror particles, changing the sign of the coordinate E_r^{inc} of the electric field of the incident beam makes the problem equivalent to the initial scattering problem. Hence, the solution must be the same as that of the initial problem, but changing the sign of the component E_r^{sca} of the scattered light, i.e., for the mirror particle:

$$\begin{pmatrix} E_l^{sca} \\ -E_r^{sca} \end{pmatrix} \begin{pmatrix} S_{11} & S_{12} \\ S_{21} & S_{22} \end{pmatrix} \begin{pmatrix} E_l^{inc} \\ -E_r^{inc} \end{pmatrix}. \tag{3.85}$$

This is equivalent to:

$$\begin{pmatrix} E_l^{sca} \\ E_r^{sca} \end{pmatrix} \begin{pmatrix} S_{11} & -S_{12} \\ -S_{21} & S_{22} \end{pmatrix} \begin{pmatrix} E_l^{inc} \\ E_r^{inc} \end{pmatrix}. \tag{3.86}$$

So the amplitude matrix is transformed as:

$$\begin{pmatrix} S_{11} & S_{12} \\ S_{21} & S_{22} \end{pmatrix} \longrightarrow \begin{pmatrix} S_{11} & -S_{12} \\ -S_{21} & S_{22} \end{pmatrix}. \tag{3.87}$$

Considering Eq. 3.87 along with Eqs. 3.62 to 3.77, we obtain that the transformation of the scattering matrix when changing a particle by its mirror particle is exactly that in Eq. 3.84.

We say that there is *mirror symmetry* in a sample if for each particle we can find one (only one) that is the mirror particle of the first.

Considering the transformations of the scattering matrix when changing to the reciprocal sample ($\mathbf{F} \rightarrow REC\,[\mathbf{F}]$) and the mirror sample (Eq. 3.84), and considering the additivity of the scattering matrix (Ec. 3.79) as well, it is simple to proof the following properties of the scattering matrix:

1. If there is one (only one) reciprocal particle for each particle of a sample, the scattering matrix can be written as:

$$\begin{pmatrix} F_{11} & F_{12} & F_{13} & F_{14} \\ F_{12} & F_{22} & F_{23} & F_{24} \\ -F_{13} & -F_{23} & F_{33} & F_{34} \\ F_{14} & F_{24} & -F_{34} & F_{44} \end{pmatrix}. \tag{3.88}$$

   There are left just 10 independent quantities in this matrix (functions of the scattering angle).

2. If there is one (only one) mirror particle for each particle of a sample, the scattering matrix can be written as:

$$\begin{pmatrix} F_{11} & F_{12} & 0 & 0 \\ F_{21} & F_{22} & 0 & 0 \\ 0 & 0 & F_{33} & F_{34} \\ 0 & 0 & F_{43} & F_{44} \end{pmatrix}. \tag{3.89}$$

   There are left just 8 independent quantities in this matrix. In this case, the DCP given by the single scattering of natural light is zero, because $F_{41} = 0$ (Eq. 3.80).

3. The combination of both of the previous conditions obviously leads to:

$$\begin{pmatrix} F_{11} & F_{12} & 0 & 0 \\ F_{12} & F_{22} & 0 & 0 \\ 0 & 0 & F_{33} & F_{34} \\ 0 & 0 & -F_{34} & F_{44} \end{pmatrix}. \tag{3.90}$$

   There are left only 6 independent quantities in this matrix. A real scattering sample is usually made of lots of irregular particles in random orientation. The random orientation assures that the reciprocity simplification (Eq. 3.88) can be done in case that the reorientation of the particles is fast enough for a particle to be oriented in both an initial position and its reciprocal position during the time of a measurement. On the other hand, random orientation assures mirror symmetry if particles are symmetrical and again the reorientation is fast enough for a particle to orient in both any position and its mirror position during one single measurements. However, in most real cases, samples are made of irregular particles without any plane of symmetry, and such particles cannot become their own mirror images by re-orienting.

In that case, a large amount of different irregular grains is needed in order to have a particle similar to the mirror image of each one. With many different irregular particles we would also have a particle similar to the reciprocal for each one, so the random orientation would not be necessary if the number of irregular grains were high enough. The combination of both the presence of many different irregular particles and the random orientation makes the double approximation (Eq. 3.90) occurs in many practical cases, like measurements of scattering matrices of mineral dust samples in the *Amsterdam Light Scattering Laboratory* [27] and in the new *IAA Light Scattering Apparatus* in Granada [55].

4. Finally, the most simple scattering matrix is that corresponding to homogeneous and isotropic spheres [3]:

$$\begin{pmatrix} F_{11} & F_{12} & 0 & 0 \\ F_{12} & F_{11} & 0 & 0 \\ 0 & 0 & F_{33} & F_{34} \\ 0 & 0 & -F_{34} & F_{33} \end{pmatrix}. \tag{3.91}$$

Only 4 independent elements remain for this case.

In the case of Rayleigh scattering, the structure of the grains is not important, because it cannot be distinguished. As a consequence, in the Rayleigh domain, the same scattering matrix corresponds to particles of all shapes for a fixed size. In particular, grains of all shapes have the same scattering matrix as a sphere (see Eq. 3.91), for a given size. Fig. 3.9 shows an example of the independent non-zero elements of the scattering matrix of a spherical particle with $x = 0.001$, normalized to the phase function (the phase function normalized to 1 at 30°). The refractive index is set to $m = 1.5 + i0.001$.

3.6.3 Coherency test for the light scattering matrix

A compendium of necessary conditions that scattering matrices must fulfill was given by Hovenier & Van der Mee in 1996 [29]. In that paper, they also put forward a necessary and sufficient condition for a matrix to be a scattering matrix. This condition is called the *Coherency test*, and was first proposed by Cloude in 1986 [8]. It is quite a useful test for checking calculated or measured scattering matrices. If we make a calculation or a measurement of the scattering matrix $\mathbf{F}$ corresponding to a certain sample, and the test is passed, we will not be able to assure that $\mathbf{F}$ is the scattering matrix of the sample, but that it will surely correspond to the scattering matrix of some sample.

The test is quite simple to apply. If $\mathbf{F} = (F_{ij})$ is the matrix we want to check, its coherency matrix $\mathbf{T} = (T_{ij})$ is defined as:

$$T_{11} = \frac{1}{2}\left(F_{11} + F_{22} + F_{33} + F_{44}\right), \tag{3.92}$$

$$T_{22} = \frac{1}{2}\left(F_{11} + F_{22} - F_{33} - F_{44}\right), \tag{3.93}$$

$$T_{33} = \frac{1}{2}\left(F_{11} - F_{22} + F_{33} - F_{44}\right), \tag{3.94}$$

$$T_{44} = \frac{1}{2}\left(F_{11} - F_{22} - F_{33} + F_{44}\right), \tag{3.95}$$

$$T_{14} = \frac{1}{2}\left(F_{14} - iF_{23} + iF_{32} + F_{41}\right), \tag{3.96}$$

$$T_{23} = \frac{1}{2}\left(iF_{14} + F_{23} + F_{32} - iF_{41}\right), \tag{3.97}$$

$$T_{32} = \frac{1}{2}\left(-iF_{14} + F_{23} + F_{32} + iF_{41}\right), \tag{3.98}$$

$$T_{41} = \frac{1}{2}\left(F_{14} + iF_{23} - F_{32} + F_{41}\right), \tag{3.99}$$

$$T_{12} = \frac{1}{2}\left(F_{12} + iF_{21} - iF_{34} + iF_{43}\right), \tag{3.100}$$

$$T_{21} = \frac{1}{2}\left(F_{12} + F_{21} + iF_{34} - iF_{43}\right), \tag{3.101}$$

$$T_{34} = \frac{1}{2}\left(iF_{12} - iF_{21} + F_{34} + F_{43}\right), \tag{3.102}$$

$$T_{43} = \frac{1}{2}\left(-iF_{12} + iF_{21} + F_{34} + F_{43}\right), \tag{3.103}$$

$$T_{13} = \frac{1}{2}\left(F_{13} + F_{31} + iF_{24} - iF_{42}\right), \tag{3.104}$$

$$T_{31} = \frac{1}{2}\left(F_{13} + F_{31} - iF_{24} + iF_{42}\right), \tag{3.105}$$

$$T_{24} = \frac{1}{2}\left(-iF_{13} + iF_{31} + F_{24} + F_{42}\right), \tag{3.106}$$

$$T_{42} = \frac{1}{2}\left(iF_{13} - iF_{31} + F_{24} + F_{42}\right). \tag{3.107}$$

This matrix has always four real eigenvalues. The test is passed if none of them is negative.

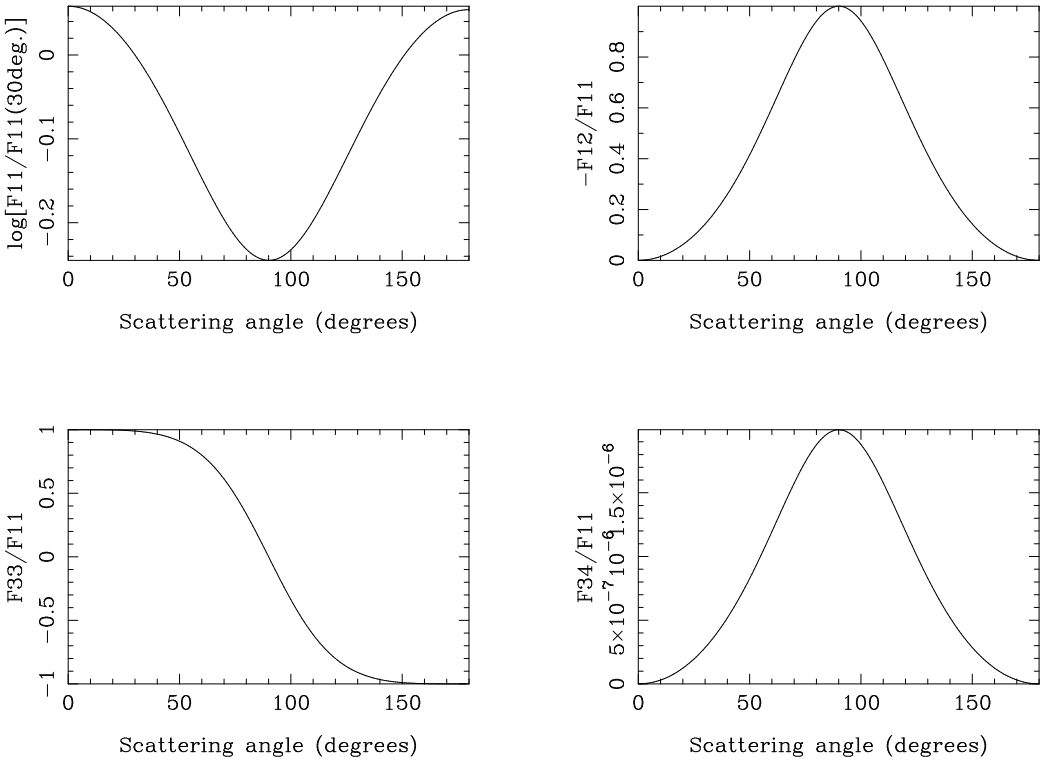

Figure 3.9: Independent non-zero relative elements of the scattering matrix of an ensemble of spheres in the Rayleigh regime: $x = 0.001$. The refractive index is set to $m = 1.5 + i0.001$.

Chapter 4

Summary of observations

Abstract

A compilation of the published observations of the DCP in comets is presented. Their common properties are emphasized so as to serve as a guide for the study of the possible mechanisms producing circularly polarized light in comets.

4.1 Introduction

In the 80's, at the time of last Halley's perihelion passage (1986), observations of the DCP of light scattered by comets were no reliable: they strongly depended on the used instrument (see, e.g., the differences between observations of Halley by Metz & Haefner [46] and Dollfus & Suchail [14]) and in many cases the errors were comparable to the mean values (see, e.g., [54]). Hence, observations of Comet Halley are not very informative regarding CP. The better information we can retrieve from them is that a persistent non-zero DCP appears in the light scattered by that comet. By the time of Hale-Bopp apparition in 1997, technology had evolved enough so as to reduce the width of the error bars by a factor 5-10 (see, e.g., [63]). Since then, observations of the DCP in comets have been more frequent, and they have become much more informative, because now the error bars are small enough for us to recognize features in the curves of the DCP.

4.2 Observations of comets

A list of some significant observations of the DCP of light scattered in comets is presented below. The more relevant features are pointed out.

Halley by Morozhenko et al. [54]

The authors observed the head of Comet Halley by using a slit of $2.7'' \times 81''$, which was set sun-ward with respect to comet's optocenter (it did not cover the nucleus). During the observations, performed in April 1986, the phase angle changed from 34.8° to 21.1° and finally increased up to 27.8°. They obtained both positive and negative values of the DCP. For a wavelength of 514 nm, the minimum was $(-0.76 \pm 0.27)\%$ and the maximum $(0.37 \pm 0.20)\%$. Mainly positive values were obtained for a wavelength of 484 nm, $(-0.05 \pm 0.15)\%$ to $(0.70 \pm 0.28)\%$). In both cases the DCP was very variable in time, not following a constant tendency.

Halley by Metz & Haefner [46]

Metz and Haefner [46] carried out other observations of Comet P/Halley when the phase angle was near 66.1°, with a filter centered at a wavelength of $\lambda = 560$ nm. They used three different diaphragms of $10''$, $15''$ and $20''$, with $10''$ corresponding to a length of roughly 9000 km at Halley's distance. Several parts of the comet were observed: central core, North, South, East and West, although no further details are given in the paper regarding the exact location of these regions. The authors obtained values of the DCP in the range $(-0.7 \pm 0.0)\%$ to $(-2.2 \pm 0.1)\%$, which were highly variable on a short time scale (of the order of minutes only). The values of the DCP obtained for the central core did not presented any special feature compared to those for other regions. In the paper they claimed that the DCP was reduced by a factor 3 when the aperture of $10''$ was replaced by that of $21''$.

Halley by Dollfus & Suchail [14]

Right and left handed CP of the light scattered by various regions of the coma of Comet P/Halley was also observed by Dollfus and Suchail [14]. They used a wide band filter covering the whole visible spectrum. The observed DCP ranged from $(-0.65 \pm 0.39)\%$ to $(1.18 \pm 0.48)\%$. The observations were performed when the phase angle varied from 40.7° to 22.5°. The DCP was very variable in time for the same region. However, a significant decrease of the DCP could be noticed when the aperture diameter changed from 7.3" to a wider diaphragm ($16.2''$ and $28.1''$). Not a large difference can be found between the observed DCP for diaphragms of $16.2''$ and $28.1''$, because the mean values are so small for those slits, that they are comparable to the error bars. No special values or tendency was found for observations of regions close to the nucleus of the comet. Dollfus & Suchail suggested in their paper that results of observations by Metz & Haefner [46] may need confirmation.

Hale-Bopp by Manset & Bastien [43]

The authors observed comet C/1995 O1 (Hale-Bopp) in April 1997. Their values for the DCP at 684 nm ranged from $(-0.24\pm0.02)\%$ to $(0.20\pm0.04)\%$, for phase angles between 40° and 47.4°. Most of the observations they carried out corresponded to the nuclear region, and the obtained values of the DCP were quite smaller than those of Comet Halley. Also in this case, a high time variability of the DCP was found, and both positive and negative values were equally obtained. All observations but one were performed by using an aperture of 15.5″. No significant difference was found for an observation of the nuclear region with an aperture of 31.1″.

Hale-Bopp by Rosenbush et al. [63]

Rosenbush et al. [63] found only negative circularly polarized light with the DCP smaller than $(0.26 \pm 0.02)\%$ for several areas of the coma of Hale-Bopp and less than 0.08% at the nucleus (see Fig. 4.1). The observations were made for a phase angle $\phi = 46°$. They used a blue-centered filter at $\lambda = 485 \pm 1$ nm. They did perform just one observation of each region, so we can say nothing about the time variability in this case. A fixed 10″ aperture was used.

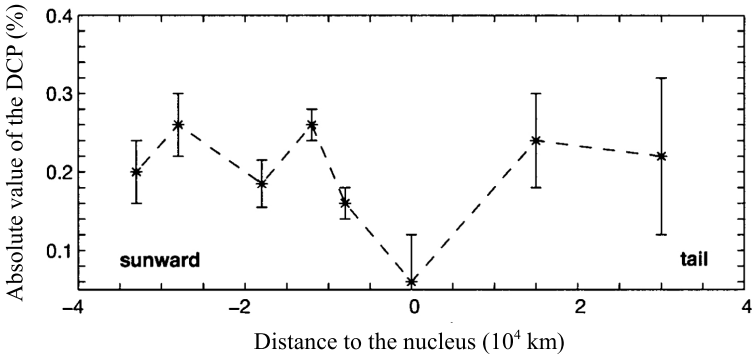

Figure 4.1: Variation of the absolute value of the DCP of light scattered in Comet Hale-Bopp with the distance to the nucleus. All values of the DCP are actually negative. The DCP goes to zero when approaching the nucleus. **Credit: Rosenbush et al. [63].**

C/1999 S4 (LINEAR) by Rosenbush et al. [62]

The authors observed the DCP of light scattered by this comet in three separate observing runs: June 28th - July 2nd, July 8th-9th and July 21st - 22nd, 2000, when the phase angle ranged from 60.9° to 122.1°. The maximum DCP reached up to $\approx 2\%$. Both positive and negative values were observed along the runs: In June 28th, only positive DCP was detected. The next day, mainly positive values were obtained, and positive and negative were observed later, until mainly negative DCP was observed the last two days (see Fig. 4.2). During this evolution, the phase angle was increasing all the time from 60.9° to 122.1°.

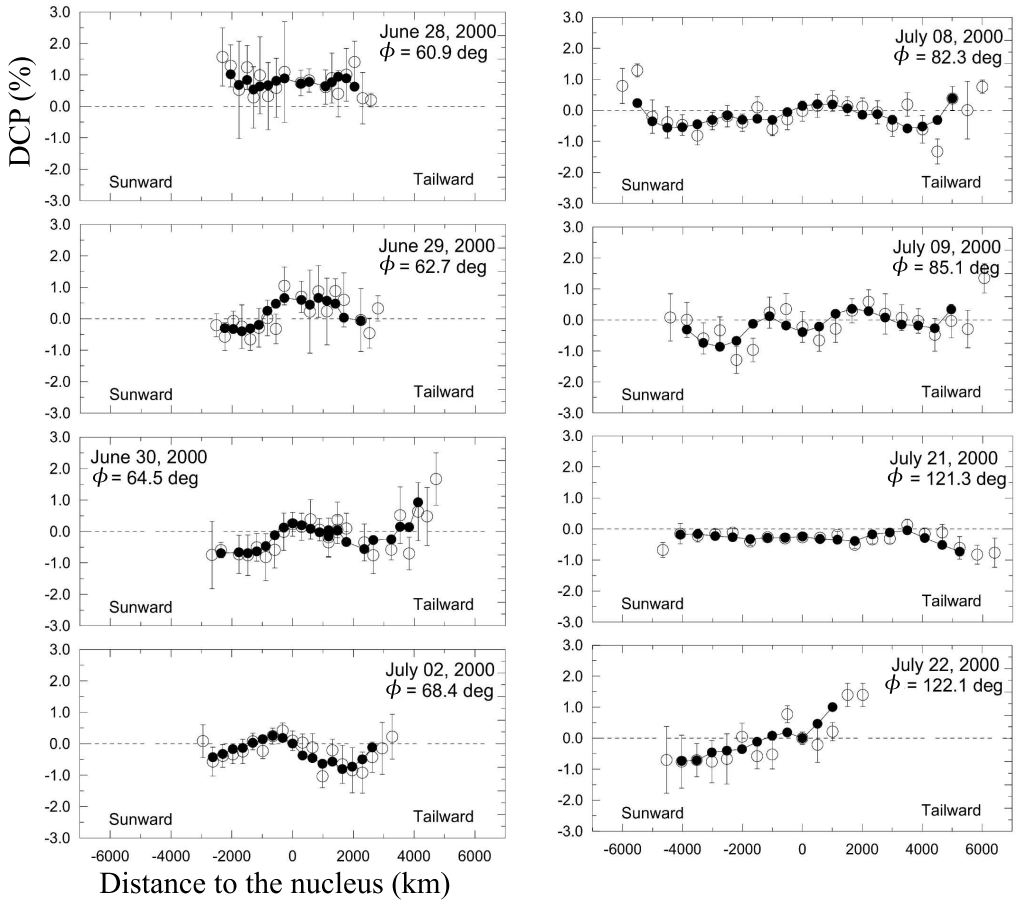

Figure 4.2: Empty circles represent the DCP along several cuts through the coma and nucleus of Comet C/1999 S4 (LINEAR). Filled circles correspond to a fit to the data. **Credit: Rosenbush et al. [62].**

As shown in Fig. 4.2, for most days, there exists a tendency of the DCP

to approach zero in the nucleus vicinity.

C/2001 Q4 (NEAT) by Rosenbush et al. [61]

By using a wide R filter and a 10″ diaphragm (4350 km at the comet distance), the authors carried out DCP observations of Comet C/2001 Q4 (NEAT) from May 21st, 2004 to May 23rd, when the phase angle was $\phi = 76°$. The higher observed DCP (in absolute value) was 0.4% approximately. A high variability could be found between the results for the last two days. A general tendency in all days is that the DCP approaches zero near the nucleus region. The curves of the DCP as a function of the distance to the nucleus is shown in Fig. 4.3.

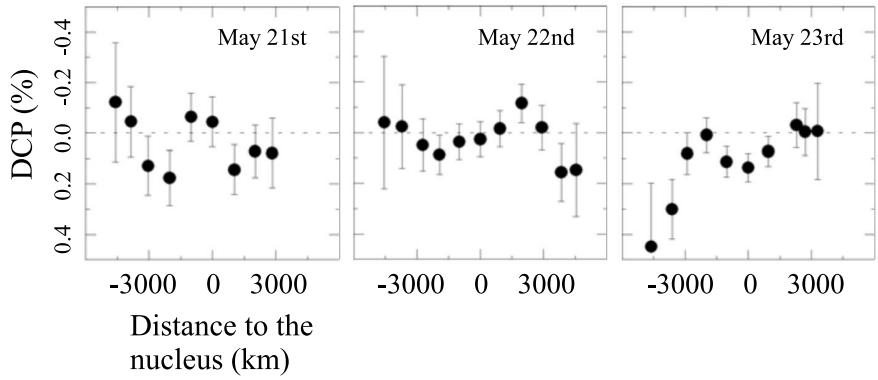

Figure 4.3: DCP along several cuts in coma of Comet C/2001 Q4 (NEAT). Except for the observations corresponding to May 23rd, the DCP approaches zero in the nuclear region. **Credit: Rosenbush et al. [61].**

4.3 Conclusions

From the observational data reviewed in the previous section, we extract the following conclusions:

- In all cases, the observed DCP for a certain region of the comet is highly variable in time (day-to-day and even minute-to-minute variations).

- The DCP approaches zero when the aperture of the diaphragm increases in observations of Halley.

- For accurate observations, such as those of Hale-Bopp, and others acquired later, the DCP approaches zero when looking at the nuclear region of the comet.

- In most cases, both positive and negative values of the DCP are obtained, except for two exceptions: observations of Hale-Bopp by Rosenbush et al. [63], where all obtained values were negative, and observations of Comet C/1999 S4. For the latter case, all observed values were positive for the smallest phase angle (60.9°). Then both positive and negative values appeared at intermediate values of ϕ, becoming finally mostly negative at $\phi \approx 120°$.

Chapter 5

Candidate mechanisms to produce circular polarization

Abstract

Based on symmetry arguments, a necessary condition for an ensemble of particles to circularly polarize the scattered light is derived. According to this condition, a complete list of candidate mechanisms to produce CP is proposed.

5.1 Introduction

Several mechanisms that may give rise to CP in astrophysical environments have been historically proposed:

- *Alignment of non-spherical particles*: this mechanism was first proposed by Dolginov & Mitrofanov in 1976 [13]. The possible alignment mechanisms have been widely studied (see, e.g. [38]), but a good agreement between the values of DCP observed in comets and calculations for particles aligned by any of these mechanisms has never been achieved.

- *Asymmetrical particles in random orientation*: In 2006, Kolokolova et al.[37] found values of the DCP much smaller than the observations of comets by calculations of single scattering by some irregular aggregates composed of identical optically inactive homogeneous spheres in random orientation.

- *Optical activity*: To our knowledge, there are no explicit calculations of the values that the DCP can achieve if the grains of the coma

were optically active, although the mechanism is generally invoked as a possible explanation to the observation of the DCP in comets (see, e.g. [62, 61]).

- *Multiple scattering*: This mechanism is just mentioned by some authors as a possibility (see, e.g. [46, 62]), but without proof.

We could just have tried the mechanisms listed above and may have serendipitously found a good agreement between the results on the DCP given by any of them and the observations in the scenario we are interested in (comets in our case). However, a rigorous search for the origin of the observed DCP needs for a systematic method to find a complete set of candidate mechanisms, i.e., we must be able to make a list of possible mechanisms giving rise to CP and assure that the actual responsible of the observed values of the DCP is within that list.

To find a complete list we first studied a necessary condition for a mechanism to produce CP. Later, we thought about all mechanisms fulfilling that condition.

5.2 Necessary condition for circular polarization[1]

Let us consider a cloud of particles which is perfectly symmetrical around the direction of the incident light. Such a system possesses certain symmetries, which means that it remains invariant after certain transformations, for instance the reflection with respect to a plane through the axis of the system, and the rotation by π *rad* about the same axis. Let us assume that the DCP observed at a certain observation position O_1 (Fig. 5.1) is right-handed and consider what happens after applying both of the above transformations. By applying the reflection with respect to a plane through the system axis we obtain left-handed circularly polarized light when observing from O_2, the opposite point of O_1 (see left panel of Fig. 5.1). Rotating it by π *rad* around the axis leads to right-handed CP in O_2 (right panel of Fig. 5.1). As light cannot be right-handed and left-handed polarized in a certain point at the same time, we deduce that the light scattered by a perfectly

[1]The result given in this section is included in the peer-reviewed publication [24], and it was presented in three conferences: the *41st annual meeting of the Division for Planetary Sciences of the American Astronomical Society* (oral presentation), the *10th Asteroids, Comets, Meteors meeting* (poster presentation) and the *XI Conference on Electromagnetic & Light Scattering by Non-Spherical Particles* (oral presentation).

azimuthally symmetrical system around the direction of the incident light cannot be circularly polarized at any scattering direction.

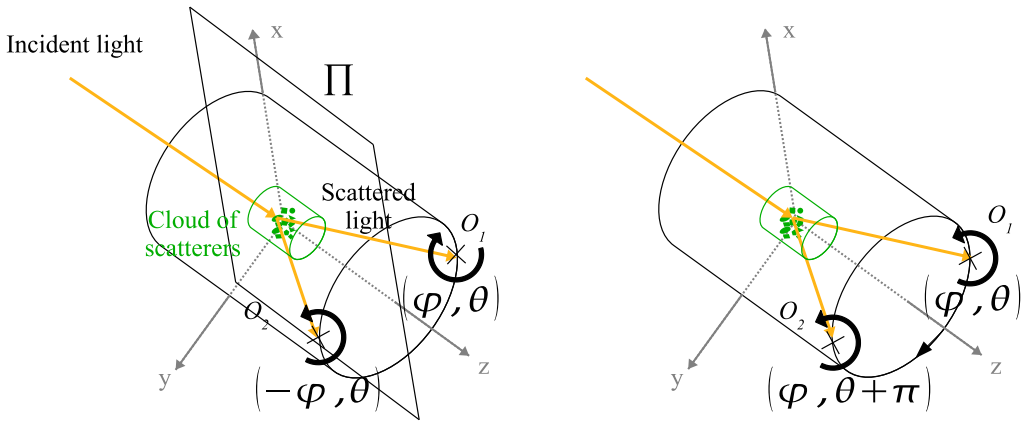

Figure 5.1: Transformations of circularly polarized light observed at a certain point, under a mirror symmetry with respect to a plane through the direction of the incident light (left) and upon a rotation by π *rad* around the same direction (right). Angles φ and θ are the usual spherical coordinates.

The condition deduced above gives us a way to find mechanisms that may circularly polarize light: anyone that breaks the symmetry of the system around the direction of the incident light is a candidate. As the condition is necessary, but not sufficient, we cannot be sure that all mechanisms breaking the azimuthal symmetry are producing CP. We must check them one by one.

5.3 Possible mechanisms to produce circular polarization

The condition deduced in Sec. 5.2 makes a constrain on the set of candidates to give rise to the DCP: we just have to look for mechanisms that break the symmetry around the optical axis. If we enumerate all ways to achieve such asymmetry we will have a complete list.

The asymmetry of the system around the direction of the incident light can be achieved by either the asymmetry of the ensemble of scatteres as a whole (a), the asymmetry of the scatterers individually (b) or both (c). In our particular case the whole cloud is a comet, and the individual scatterers are the particles of the coma plus the nucleus.

a. Let us assume that the scatterers (both the particles of the coma and the nucleus) are perfectly symmetrical (spherical homogeneous and isotropic

grains)[2]. The only way of such a system to achieve asymmetry is the *inhomogeneous distribution of particles in the coma*.

We would like to remark the fact that we are calling "cloud of scatterers" to the part of the comet that the observer is looking at, i.e., if a diaphragm is used to observe a comet, only light coming from a local region will be received, so that region will be the cloud of scatterers of the scattering problem, instead of the whole comet. This means that even an ensemble of spherical homogeneous and isotropic scatterers symmetrically distributed around the direction of light may lead to an asymmetrical scattering scenario if the observer focusses only on light coming from a certain part of the comet, which is not placed in its center (see Fig. 5.2).

Let us assume that light coming from a non-central local region of a comet (R_1 in Fig. 5.2) is circularly polarized by any means. Then, if the comet is symmetrical with respect to the direction of the incident light, the DCP of light coming from the opposite region R_2 will cancel that of the light coming from R_1. Let us prove it: if we observe light coming from R_1 and R_2 at the same time, we are looking at a system that possesses at least two symmetries (rotation of π *rad* around the direction of light and reflection on the plane Π indicated in Fig. 5.2). That is the same scenario as presented in Sec. 5.2 to prove that an azimuthally symmetrical comet around the optical axis cannot circularly polarized light. Thus, we deduce that light coming from the system formed by regions R_1 plus R_2 cannot be circularly polarized when seen from any scattering direction. This means that the DCP of light coming from R_1 (if it is non-zero by any means), is canceled by that of light coming from R_2.

As a corollary, if a region located in the geometric center of the comet is observed, the DCP of light coming from it must be exactly zero at all scattering directions.

In contrast, according to the previous statements, the *local observation of a non-central region* of the coma is another candidate mechanism to circularly polarize light scattered by comets. It is quite important to consider this mechanism, because polarimetric observations of comets are usually done with a diaphragm so that only photons coming from a small region of the comet are taken into account (see Chap. 4).

b. Let us suppose now that the distribution of particles in a comet is perfectly

[2]In a real situation, however, the particles of the coma may be quite irregular [5], and the nuclei are known to have irregular shapes, as well as some active areas and jets on its surface [9].

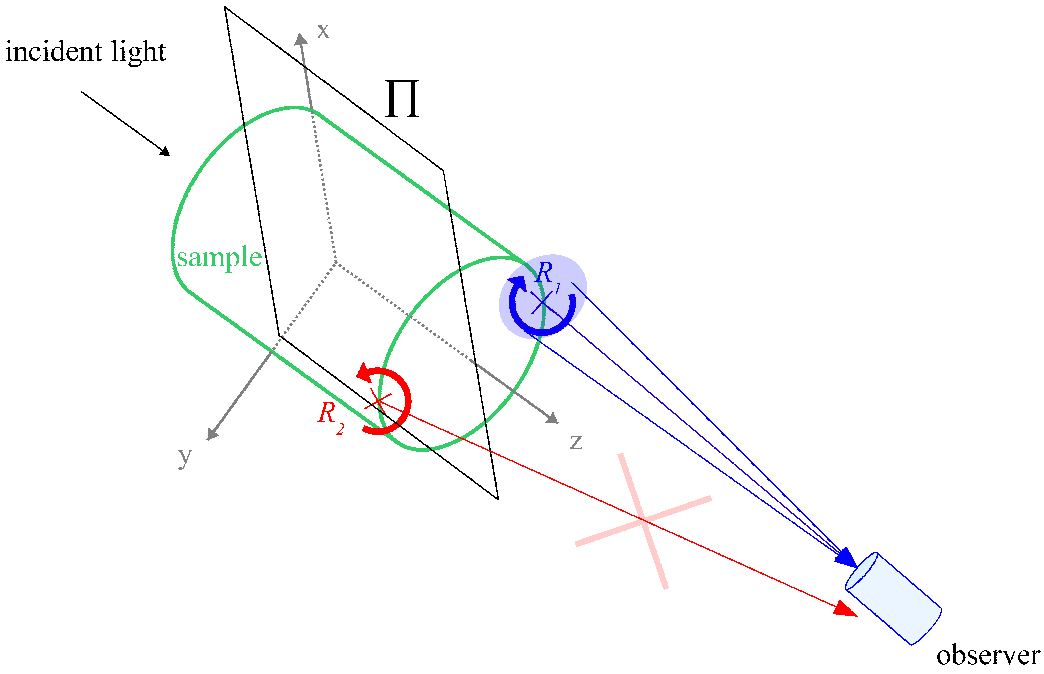

Figure 5.2: A non-zero DCP may arise in light coming from any non-central region R_1 of an azimuthally symmetrical sample. If only that region is observed, the possible DCP will not be cancelled by the one of light coming from the opposite region R_2, so the observer may detect a non-zero DCP.

symmetrical around the optical axis[3].

First of all, the grains might be either randomly oriented or not. Hereafter we will say that the particles are aligned if the are not in random orientation, no matter whether they are in a fixed orientation or moving somehow with less than three rotational degrees of freedom. For instance, we say that a sample of prolate spheroids with their longest axes forming 90° with the direction of the incident light and 45° with the x axis are aligned, but the same spheroids randomly oriented in a plane through the optical axis are aligned too. The *alignment of non-spherical particles* can break the symmetry around the direction of the incident beam, so it is another mechanism to take into account.

In case that the particles of the coma are randomly oriented they can still break the symmetry of the sample if they are asymmetrical themselves: they have no planes of symmetry (macroscopically and/or microscopi-

[3]In a real case, the distribution of scatterers is inhomogeneous because of the presence of active areas and/or jets on the surface of the nucleus [9], for instance.

cally). In such a case, once we set a particle in a fixed orientation, there is no way to find its mirror image by re-orienting it. This leads to an asymmetry around the optical axis of the comet that can be understood as follows: imagine a sample of identical asymmetrical particles. If at a certain instant one of them is located in P_1 (see Fig. 5.3) with a certain orientation, there is no chance at all to find its mirror particle in P_2, even if the grains are randomly oriented, because mirror images are impossible just by reorientation in the case of asymmetrical particles. This causes that the system do not remain invariant under a reflection on any plane through the direction of the incident light. As a consequence, we conclude that the system is not azimuthally symmetrical with respect to the optical axis and hence the scattered light may be circularly polarized.

Asymmetry of particles can be understood in two ways: macroscopic and microscopic.

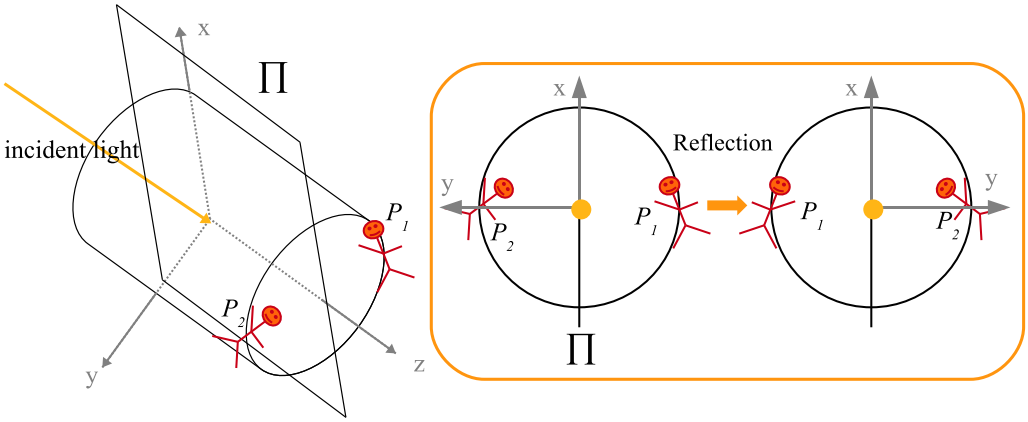

Figure 5.3: When we apply a reflection on a plane containing the direction of the incident light in a symmetrical distribution of asymmetrical particles, the result is not an equivalent system to the first.

Hereafter, we will refer to the macroscopic mirror symmetry just as "mirror symmetry". According to the above discussion, the *breaking of the mirror symmetry* of the particles (coma made of particles with asymmetrical shapes) is a candidate to produce CP.

We will refer to the microscopic asymmetry as *optical activity*. We distinguish two kinds of optical activities: the one by mineral grains and the one by organic substances. In mineral particles, molecules are much smaller than the wavelengths of visible light, so they behave as Rayleigh scatteres, i.e., point particles whose structure cannot be distinguished by light. In

such a case the asymmetry of the molecules themselves is not important, but the point is the non-symmetrical distribution of them in the particles: grains of crystalline minerals that crystallize in a non-symmetrical system are microscopically asymmetric. Amorphous minerals or cubic crystals, for instance, are ruled out from the optical activity, because a macroscopically symmetrical particle made of such materials could become its own mirror image just by reorientation. Regarding organic materials, the situation is quite different, because they are made of macromolecules, with sizes quite closer to the wavelengths of visible light than mineral molecules (so light can distinguish its structure). If these molecules were asymmetrical (like helixes, for example), they would break the symmetry by themselves as though they were small particles, independently of how they are distributed into a grain. The *optical activity* of both mineral and organic particles is another candidate to give rise CP.

The *asymmetry of the nucleus of the comet* is also a possibility to break the symmetry, around the optical axis. The asymmetry could be due to different reasons, such as irregular shape, albedo inhomogeneities, etc.

c. A combination of the above mechanisms would lead to a combination of asymmetry of the scatterers and the comet as a whole.

We have considered all possibilities, so now we have a complete list of possible mechanisms. We will study them in detail in the following chapters: alignment of non-spherical grains in Chap. 6, breaking of the mirror symmetry in Chaps. 7 and 8, in Chap. 9, optical activity, and finally, local observation of a non-central region of the comet, inhomogeneous distribution of particles in the coma, and the effect of an asymmetrical nucleus, in Chap. 10.

5.4 Conclusions

- The breaking of the symmetry of a comet around the direction of the incident light is a necessary condition for a mechanism to circularly polarize the scattered light.

- A complete list of candidates to produce CP of light scattered in comets is the following:

    1. Alignment of non-spherical grains.
    2. Breaking of the mirror symmetry.

3. Optical activity of the material composing the particles.
4. Local observation of a non-central region.
5. Inhomogeneous distribution of particles in the coma.
6. Asymmetrical nucleus of the comet.

Chapter 6

Circular polarization of light scattered by aligned particles

Abstract

The bombardment of non-spherical grains of the cometary coma by the particles of the solar wind is studied as a mechanism to produce the alignment of the grains. It is found that micron-sized elongated particles can be aligned in a few hours by this mechanism. Nevertheless, no CP at all is derived from this alignment because the resulting system is symmetrical around the direction of the solar incident light.

6.1 Introduction

As we stated in Sec. 5.3, we consider that particles are aligned if they are not in random orientation, no matter whether they are in a fixed orientation or not.

A long list of possible mechanisms for aligning particles has been proposed since Dolginov & Motrofanov paper in 1976 [13]. In that paper the authors already proposed four possible mechanisms for the alignment of dust in the coma of comets: paramagnetic relaxation, gas streams and interaction of the solar radiation and the solar wind with the grains. They deduced under restrictive assumptions that the particles in the part of the coma turned towards the Sun are aligned by radiative pressure, and the DCP of the scattered light could reach 4% for silicate-like particles. After that paper, a considerable progress has been made regarding the alignment mechanisms: a recent complete review can be found in [38]. In spite of this, it is not clear yet if the alignment really happens in cometary comae, and, in case it takes place, what mechanism is the main responsible for that.

6.2 Mechanism producing the alignment

If the alignment of non-spherical particles is the cause of the observed DCP of light scattered in comets, the mechanism that aligns particles must be fast, because a non-zero DCP is observed in the coma, even in regions relatively close to the nucleus, and most of the particles in that zone were ejected from the surface of the nucleus just some hours or days before [9]. As results coming from previous works are not conclusive (see Sec. 6.1), we decided to make an investigation by our own. We did not try to study all alignment mechanisms one by one because this is beyond the scope of the present work. Instead, we wondered how would grains align and what would it be the typical alignment time for some simple mechanism over some simple kind of particles. We considered rectangular prisms as grains of the coma, and we developed a Monte Carlo model of bombardment by particles of the solar wind in order to simulate their alignment. So the alignment mechanism that we studied was *interaction of dust particles with the solar wind*. We chose this one for two reasons:

- Comets, when observed, are located at a distance from the Sun of the order of the AU, where the interaction of the dust grains of the coma with the solar wind may be significant.
- To our knowledge, there are not explicit calculations of the alignment time of particles by the interaction with the solar wind. Thus we wanted to make a contribution to the solution of the problem of the alignment by this study.

6.3 Description of the Monte Carlo bombardment model

First of all, as we just wanted to investigate the effect of the alignment of the particles, we considered a cometary nucleus and a distribution of grains in the coma that are azimuthally symmetrical around the direction of light. Let us now carefully describe what kind of dust particles of the coma we assumed, what are the parameters describing the solar wind and how the particles of the solar wind interact with the dust grains.

- *Dust particles*: For simplicity we supposed a comet located at $1AU$ from the Sun. The reason for that is that at this position, the solar wind is well characterized and it has a significant effect.

We chose rectangular prisms (compact particles) as dust grains. We used two shapes: a prolate prism with axes ratios 1:1:2 (A) and an oblate prism with 2:2:1 (B). We set the dimensions of the particle (A) as $0.1\ \mu m \times 0.1\ \mu m \times 0.2\ \mu m$. The dimensions of (B) are calculated so that the volumes of both particles (A and B) are equal. We assumed a density of 3 gcm^{-3} for the grains. This is a typical value for silicates, and we already stated that silicates are one of the main components of the cometary dust (see Sec. 2.3).

As we did not have any information on the initial state of rotation of the grains, we supposed a certain initial angular velocity instead of assuming the particles to be at rest. In this way, the alignment may be slower than for particles at rest, and we wanted to consider the most unfavorable scenario. We assumed an initial angular velocity $\omega_0 = 0.7\ rad\ s^{-1}$. The actual initial rotation velocity might be much higher, for instance, if the grains are dragged by a stream of gas ejected at high velocity from the surface of the nucleus. However, we do not have any quantitative information about this effect. The best we could do was to assume an scenario closer to reality than having the particles at rest at $t = 0$. We took as the initial rotation axis the longest, because that corresponds to the more stable rotational state, and we supposed that particles quickly go to that state by dissipating heat. The dissipation could take place because grains are not perfect solid bodies, and there might be some internal frictions when particles are deformed due to rotation. Particle (A) was initially set with its longest axis parallel to the direction of incidence of the flux, and particle (B) started the simulation oriented with its shorter axis parallel to the flux.

- *Solar wind*: We assumed two important hypotheses:

  1. The particles of the solar wind propagate in a uniform and constant flux in the direction (and sense) of light. Here, we are implicitly making the assumption that the solar wind is not significantly deviated from the radial direction of propagation by the magnetic field.
  2. The particles of the solar wind interact with the dust grains of the coma as if the grains were in vacuum, i.e., it is assumed that there is no interaction of the solar wind with the gas. We based this hypothesis in the low vapor density of the coma.

Table 6.1 shows the main characteristics of the solar wind at $1AU$ [57].

Composition	50% electrons, 48% protons, and 2% ions He^+
Velocity v_F	350 kms^{-1}
Flux density	$3 \cdot 10^8$ $cm^{-2}s^{-1}$

Table 6.1: Some properties of the solar wind used in the model of bombardment.

- *Interaction*: Collisions were considered completely inelastic. This hypothesis simplifies the calculations, as in this way we know that a solar wind particle transfers all its angular momentum to the dust grain it hits. Hence, the increment of the angular momentum of a grain after a collision is $d\mathbf{L} = \mathbf{r} \times \mathbf{p_p}$, where $\mathbf{p_p}$ is the linear momentum of the particle of solar wind before the collision ($\mathbf{p_p} = m\mathbf{v_F}$, where $\mathbf{v_F}$ is the velocity of incidence of the solar wind particle and m is its mass). From $d\mathbf{L}$, the new angular momentum of the grain is given as $\mathbf{L}' = \mathbf{L} + d\mathbf{L}$. Then, by calculating the inverse of the inertia tensor $\mathbf{I}$ of the grain, we obtain its new angular velocity as $\boldsymbol{\omega} = \mathbf{I}^{-1}\mathbf{L}$. With the new angular velocity, we apply a differential rotation, and get the position of the grain an elemental time dt later. This process is repeated with particles sequentially randomly hitting on the visible side of the grain, at the rate given by the flux density specified in Table 6.1.

To quantify the alignment of the grains, we define two orthogonal systems of reference. One is fixed in the particle and the other one is external. The system fixed in the particle has its axes coincident with the principal axes of the prism. The external system of reference has the z axis in the direction of propagation of the solar wind, but in the opposite sense (see 6.1).

6.4 Results on the alignment

As shown in Fig. 6.2, the prolate grain (A) is aligned with its longest axis perpendicular to the direction of the incident flux. Despite its initial orientation was the most unfavorable to achieve the alignment, it happens in less than $1.8 \cdot 10^4$ s. Once it is aligned, (A) quickly rotates around its longest axis, and that axis slowly randomly rotates around the direction of the solar wind. As shown in Fig. 6.3, the oblate prism is not aligned even in a

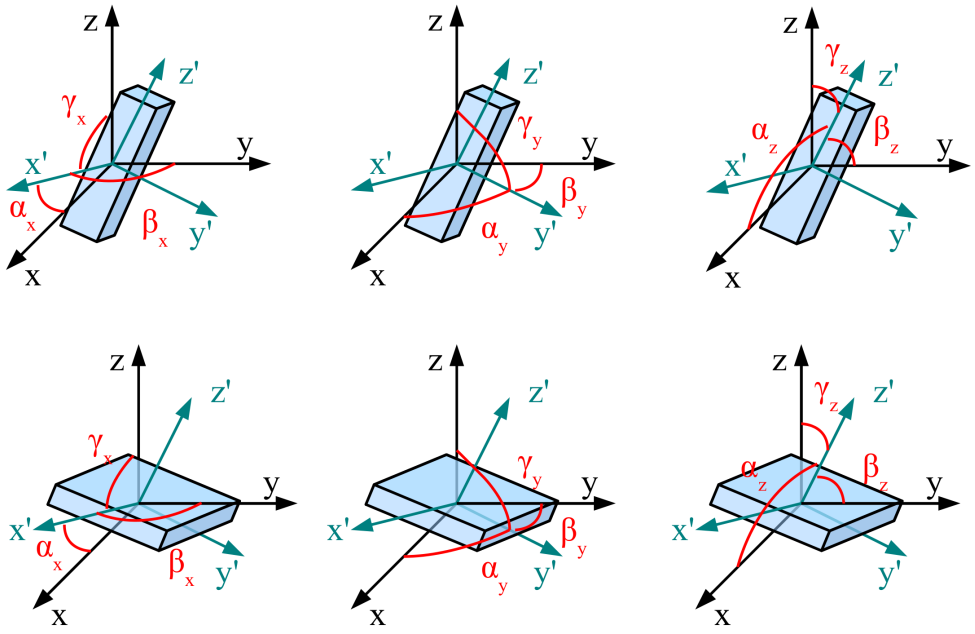

Figure 6.1: Particle and external systems of reference used to study the alignment. The three upper plots correspond to particle labeled as (A), and the lower panels to particle (B). The angles to quantify the alignment are plotted too. The z axis of the external system is parallel to the direction of the incident flux of solar wind particles, but points to the opposite sense.

longer time ($2.4 \cdot 10^5$ s) than the prolate, despite it starts with its longest axis perpendicular to the direction of the incident flux, which is the alignment configuration of particle (A).

Thus, we can conclude that particles are aligned with their longest axis perpendicular to the direction of the incident flux of the impinging particles. As oblate particles do not have a well differentiated longest axis, they cannot be aligned (at least as fast as prolate grains).

On the other hand, the alignment of (A) occurs in just a few hours, so if this kind of alignment was the responsible for the observed DCP in comets, we would have found a good candidate for mechanism to align the grains, because it acts quite fast.

Nevertheless, this kind of alignment does not circularly polarize light at all. The reason is that once the grains are aligned, their longest axes can freely rotate around the direction of the solar wind (which is the same as the direction of the incident light), and that is an azimuthally symmetrical scenario around the optical axis of the system. Hence, according to Sec. 5.2,

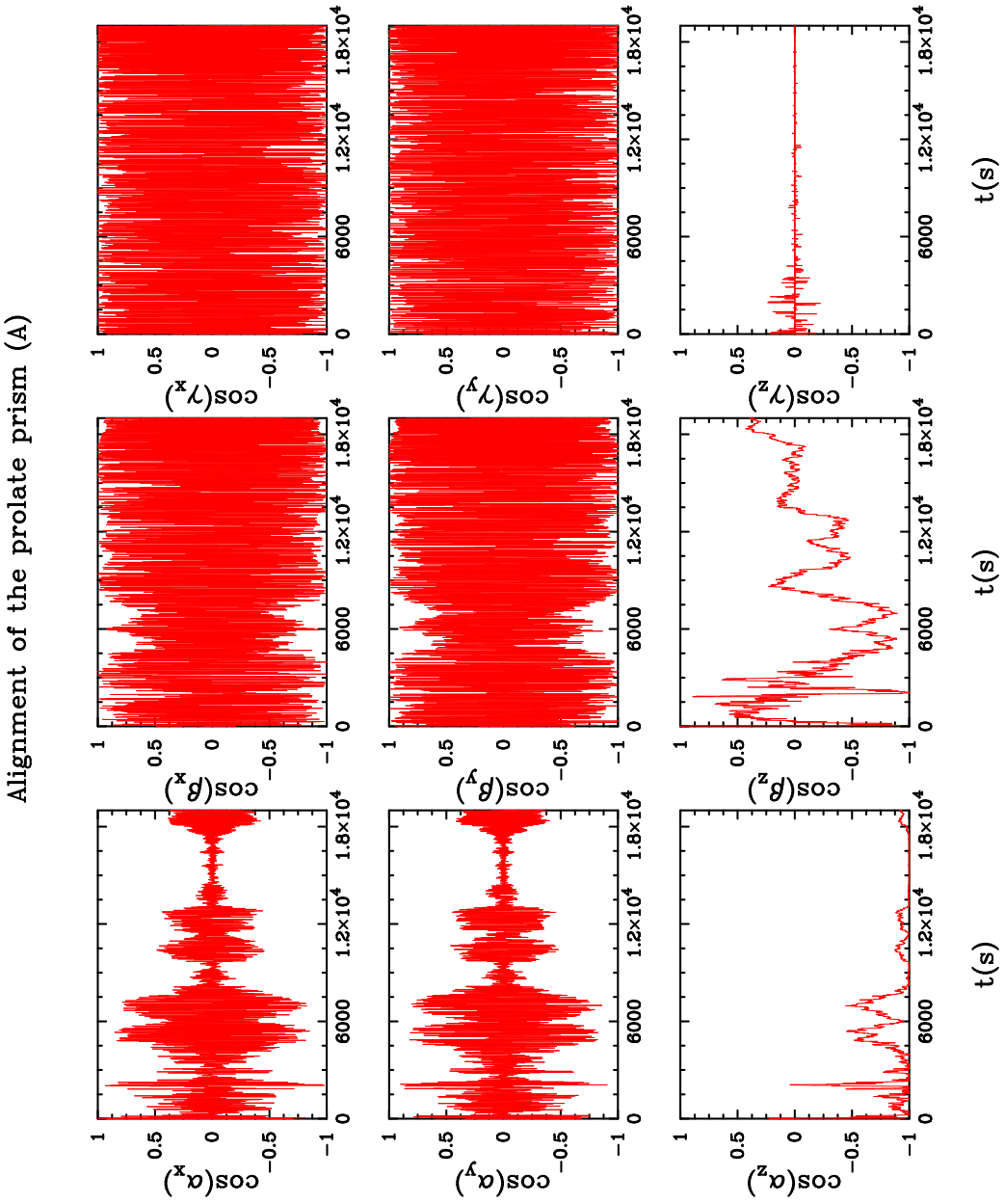

Figure 6.2: Evolution of the rotation of the prolate grain of dimensions 0.1 $\mu m \times 0.1\ \mu m \times 0.2\ \mu m$ and density of 3 gcm^{-3}, under bombardment by the solar wind. In less than $1.8 \cdot 10^4\ s$, it is aligned with its longest axis perpendicular to the direction of the incident flux.

no CP can be achieved by this mechanism.

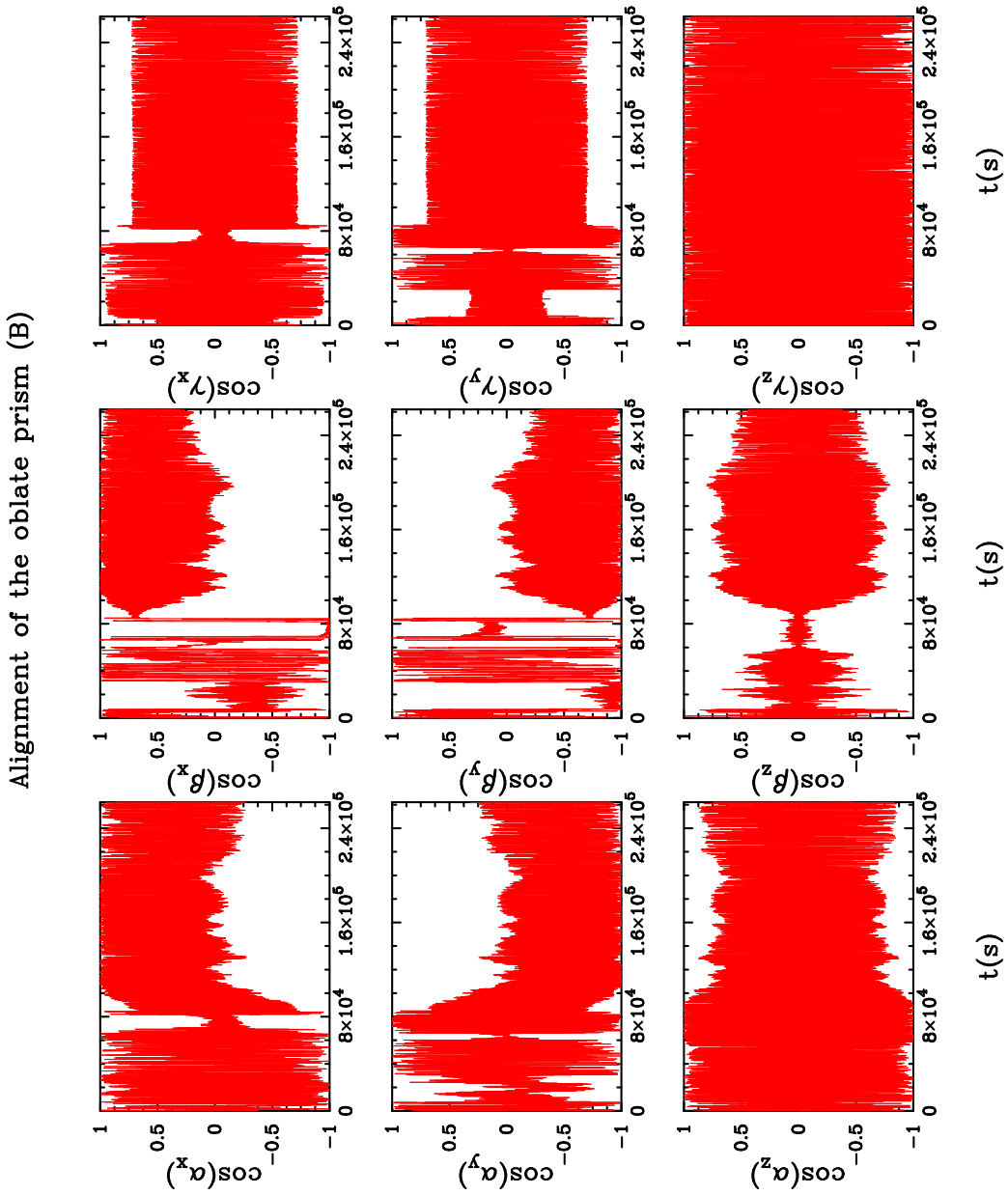

Figure 6.3: Evolution of the rotation of the oblate particle with axes ratios $2:2:1$, and the same volume and density as (A), under bombardment by the solar wind. There is no alignment in $2.4 \cdot 10^5$ s.

6.5 Conclusions

- Prolate rectangular prisms of dimensions $0.1\ \mu m \times 0.1\ \mu m \times 0.2\ \mu m$ with a density of 3 gcm^{-3} are aligned in $1.8 \cdot 10^4$ s due to the bombardment

by the solar wind particles at an heliocentric distance of $1AU$.

- The alignment occurs with the longest axis of the particle oriented perpendicularly to the direction of the incident light.
- Oblate particles with the same volume and density as the prolate ones, but with axes ratios 2:2:1, are not aligned even in $2.4 \cdot 10^5$ s.
- If particles in comets were actually aligned and the responsible mechanism for the alignment was the bombardment by the solar wind, we would not obtained any non-zero DCP, because the cloud of aligned particles would be symmetrical around the direction of the incident light.

Chapter 7

Circular polarization of light scattered by asymmetrical model particles

This chapter is based on the peer-reviewed paper by Guirado et al. entitled *Circular polarization of light scattered by asymmetrical particles* [22]. Some of theses results were presented in the *IX Conference on Electromagnetic & Light Scattering by Non-Spherical Particles*.

Abstract

To clarify the possible contribution of asymmetry of particles to CP in comets, some calculations of the DCP of light singly scattered by some kinds of asymmetrical model particles were performed. We considered aggregates of optically inactive homogeneous identical spheres in random orientation. We analyzed the effect of changing the size of the particles, and performed a size average. The effect of changing the refractive index and the shape of the grains was studied too. The values of the computed DCP are generally in the range of the observed ones for light scattered by comets (Chap. 4).

7.1 Introduction

As we stated in Sec. 5.3, if the particles in the coma of a comet are asymmetrical, there is a chance for the scattered light to be circularly polarized, even if the grains are in random orientation and homogeneously distributed around a symmetrical nucleus.

Along this chapter we will be dealing with the calculation of the maximum DCP that a sample of randomly oriented asymmetrical particles can

produce. Since we are primarily interested in the application to the cometary environment, we will assume similar sizes and refractive index as have been found for dust in comets (see Secs. 2.4 and 2.3). In this chapter, our purpose is not to build a realistic model of a cometary coma to try to reproduce the observations. Instead, we just want to develop the most simple model that can tell us whether or not we must rule out single scattering by optically inactive asymmetrical particles in random orientation as a mechanism producing a significant DCP in comets. If we obtain very small values of the DCP compared to the observations by assuming a very asymmetrical model particle, this mechanism can be ruled out. If we obtain values of the DCP of the order of the observations or larger, we will give another step by building up a more realistic model.

In Sec. 7.2 we explain the theoretical basis of the mechanism that makes asymmetrical particles circularly polarize the scattered light. Sec. 7.3 contains the description of the model, and Sec. 7.4 includes an analysis of some available codes to perform the required calculations plus a brief review of the computational method that we finally chose. Numerical results are shown and discussed in Sec. 7.5. Finally, in Sec. 7.7, the main conclusions are given.

7.2 How asymmetrical particles produce circular polarization

We already discussed in Sec. 5.3 that, based on the condition given in Sec. 5.2, the presence of asymmetrical particles in the coma of a comet may lead to a certain DCP of the scattered light. In this section, we present another proof of the possibility of having CP by this mechanism. This proof is based on symmetry arguments applied to the Stokes parameters. It is just valid for the breaking of the mirror symmetry, and we are presenting it in order to better understand how the mechanism works.

Suppose a collection of randomly oriented asymmetrical particles illuminated by a plane-parallel beam of unpolarized light with flux vector $(1, 0, 0, 0)^t$. The flux vector of the singly scattered light at a certain distance, can generally be written as $(a, b, c, d)^t$, using the scattering plane as the plane of reference for the Stokes parameters. This flux vector depends on the scattering angle and the properties of the scattering particles. In what follows we keep the scattering angle fixed. Let us now replace each particle by its own mirror particle, but keeping the incident light unchanged. Because of symmetry, the scattered beam will become the mirror image with respect to the

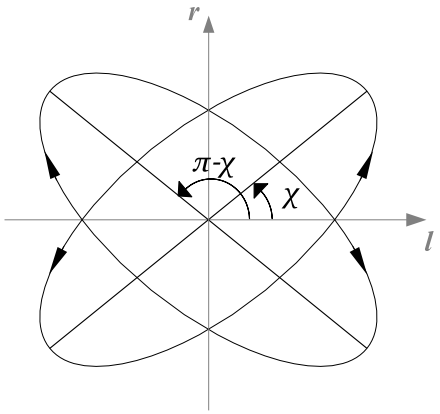

Figure 7.1: Vibration ellipses of two beams of light traveling in the direction (and sense) given by the vector product $\hat{\mathbf{r}} \times \hat{\mathbf{l}}$. The plane through $\hat{\mathbf{l}}$ perpendicular to $\hat{\mathbf{r}}$ is the scattering plane. The two beams are each other's mirror image with respect to the scattering plane. The orientations of the major axes of the vibration ellipses are given by the angles χ and $\pi - \chi$ while the handedness of the beams is opposite.

scattering plane of the original beam. Therefore, the flux vector of the scattered beam can now be written as $(a, b, -c, -d)^t$, since the last two Stokes parameters must have changed their sign, as follows from their definitions and Fig. 7.1. For details we refer to Hovenier et al. [28].

Next, we consider a collection of randomly oriented particles in which each particle is accompanied by its own mirror particle. In this case the flux vector of the scattered beam is the sum $(a, b, c, d)^t + (a, b, -c, -d)^t = 2(a, b, 0, 0)^t$. Clearly, the same is true for a collection of particles having a plane of symmetry (like spheres, spheroids, cubes, etc.), since these are their own mirror images. So the DCP is d/a, $-d/a$ and zero, respectively, in the three cases considered. This explains how single scattering of unpolarized light by randomly oriented particles can generate a non-zero DCP. Obviously, this can also occur for a collection of particles in which a number of asymmetrical particles is not accompanied by their own mirror particles, but a certain unbalance exists.

7.3 Description of the model

In order to simplify the study, we did not take into account either the distribution of the particles on the coma or the presence of the nucleus. We

considered a sample of optically inactive particles in random orientation and calculated the DCP after single scattering of natural light. So, instead of building a radiative transfer model of the comet, we just calculated the scattering matrix of a sample of randomly oriented particles of a certain size, shape and refractive index, and then apply Eq. 3.80 to obtain the DCP, (also Eq. 3.81 to obtain the $EDLP$).

As we were interested in obtaining the largest possible DCP, we used some model particles especially designed with very asymmetrical shapes. The used particles are described in each section. Although compact grains have been proven to explain many of the observed properties of cometary dust [52], we used aggregates of spheres for our calculations because of the following reason: We needed accurate calculations since the observed values of the DCP are close to zero. Moreover, we needed to calculate the DCP for the largest possible particles in order to approach the sizes of the real grains in comets (see Sec. 2.4). The T-matrix technique for aggregates of spheres is the best choice to solve this problem, because it makes the orientation average analytically, so it is more accurate and faster than the other methods (see Sec. 3.5).

Hereafter, when we refer to aggregates, we will denote by x the size parameter of the monomers of the particle, and by X the size parameter of the whole aggregate.

Along the present chapter, we will consider a wavelength $\lambda = 500\ nm$.

7.4 Choice and description of the numerical method

There exist at least two public available codes implementing the T-matrix technique for multi-spheres: Mackowki & Mishchenko's [42] and Xu's [71]. In this section, we present an a analysis to determine which one is the most appropriate for our calculations of the DCP. For such purpose, we made some comparisons between T-matrix and DDA, and we eventually compared results from both implementations of T-matrix.

The more widely checked DDA code is the one developed by Draine & Flatau [17], although a recent new implementation by Yurkin & Hoekstra [72] has arisen, which introduces some numerical improvements that reduce the CPU time and memory consumption for calculations (see comparison in [60]). However, this new code has not been optimized yet for randomly oriented particles, and regarding this type of calculations it gives less accurate results than Draine's code [60]. Thus, we chose Draine's implementation of

the DDA method.

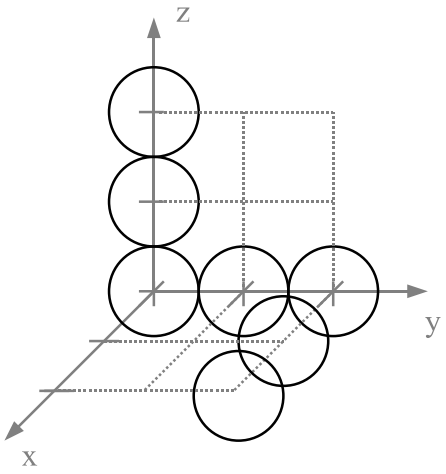

Figure 7.2: Asymmetrical model particle used for comparison of DDA and Mackowski & Mishchenko's T-matrix method. It is composed of 7 monomers. All monomers are equal in size and refractive index.

First of all, we compared DDA Draine's results with those by Mackowski & Mishchenko's T-matrix code. We used as a test particle the one described in Fig. 7.2. We chose $m = 1.5 + i0.001$ as refractive index. Figs. 7.3 and 7.4 show the calculated DCP for the particle in random orientation for two sizes: $x = 0.5$ and $x = 1$ respectively (or $X = 0.96$ and $X = 1.91$). In both cases we built the particle with 69443 dipoles for DDA calculations. The choice of the large number of dipoles was made to fulfill the criterion $|m|kd < 0.1$ (see [17] for an explanation). For calculations of flux and the $EDLP$, $|m|kd < 0.5$ is enough, as stated in [17], but for the DCP we need better accuracy. We made an average over 16000 orientations.

There is a good agreement between the results given by both methods, so we can rely on both of them to calculate the DCP as a function of the scattering angle with high accuracy.

In any case, we also checked Xu's code by comparing its results to Mackowki & Mishchenko's. We used the particle defined in the right panel of Fig. 7.5. The size parameter of each monomer was set to $x = 1$, so the size parameter of the whole grain became $X = 2.92$. This time we calculated the $EDLP$ for the particle in random orientation (Fig. 7.6) as well as the DCP (Fig. 7.7) by both Mackowski & Mishchenko's and Xu's codes for multi-spheres. We found significant discrepancies when comparing the computed results to each other, especially in the DCP. This means that one of the

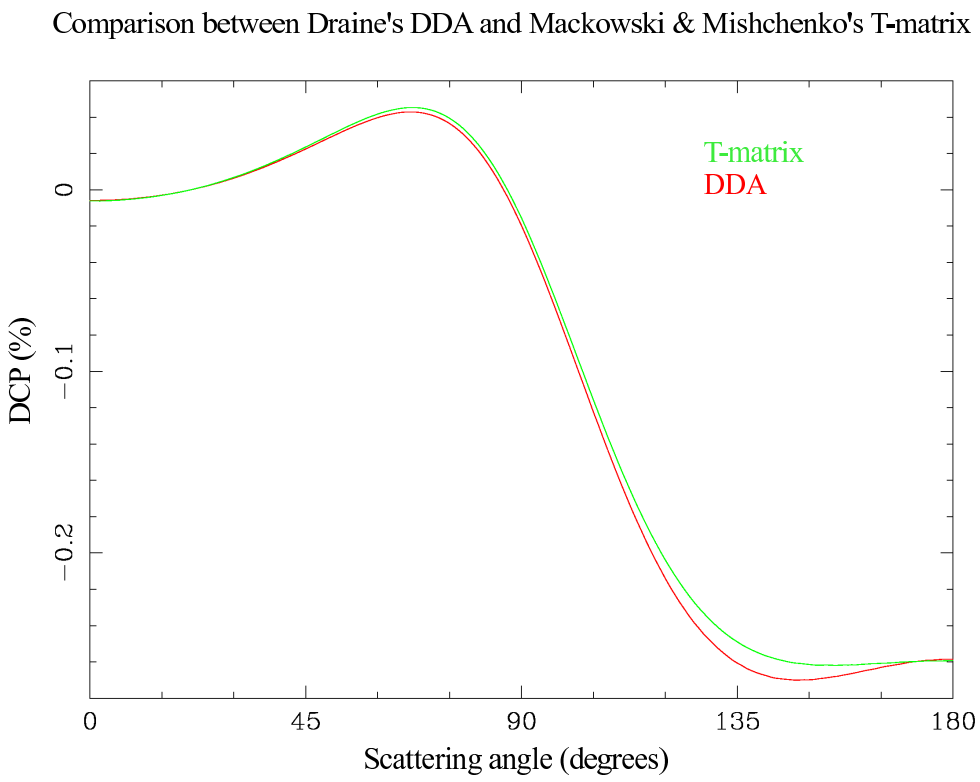

Figure 7.3: DCP as a function of the scattering angle, calculated with DDA and Mackowski & Mishchenko's T-matrix, for the particle defined in Fig. 7.2, in random orientation. The size parameter of all monomers is $x = 0.5$ ($X = 0.9565$), and $m = 1.5 + i0.001$.

codes is not doing well. We had already checked Mackowski & Mishchenko's code, but, what is more, as seen in Fig. 7.6, Xu's program gives some values of the $EDLP$ larger than 100%, what makes no sense. Hence, we definitively ruled out Xu's code for multi-spheres.

Based on the above analysis, we chose the freely available double precision superposition T-matrix code by Mackowski & Mishchenko [42] for our calculations. As the results depend somewhat on the accuracy parameters of the code, and we needed very accurate calculations because we expected to obtain values of the DCP very close to zero, we changed the accuracy parameters until the results became stable. The criterion for stability was the following: we defined the relative error for each element of the scattering matrix as $\frac{F_{ij}(parameters_1)-F_{ij}(parameters_2)}{F_{ij}(parameters_2)}$, with $parameters_2$ ten times smaller than $parameters_1$. Then, we changed the parameters until the error was smaller than 10^{-9} for all elements F_{ij} of the scattering matrix. In order to

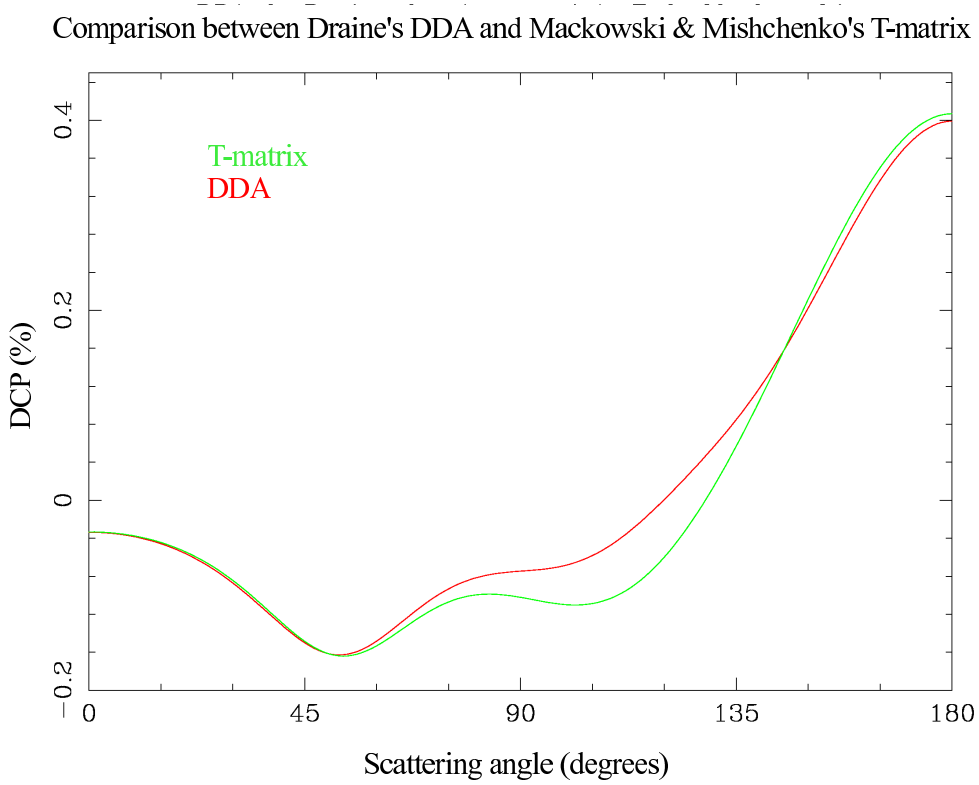

Figure 7.4: DCP as a function of the scattering angle, calculated with DDA and Mackowski & Mishchenko's T-matrix, for the particle defined in Fig. 7.2, in random orientation. The size parameter of all monomers is $x = 1$ ($X = 1.913$), and $m = 1.5 + i0.001$.

make another checking of the results, we repeated some calculations using DDA, and in all cases we found good agreement with results by T-matrix.

7.5 Results and discussion

In this section, we present results of a systematic study of the behavior of the DCP when changing different physical parameters of the scatterers. In all cases, the DCP is plotted as a function of the scattering angle.

7.5.1 The effect of changing the size of the particles

Let us consider a sample of identical aggregates. Each aggregate is made of seven identical spherical monomers (left side of Fig. 7.5). We call these

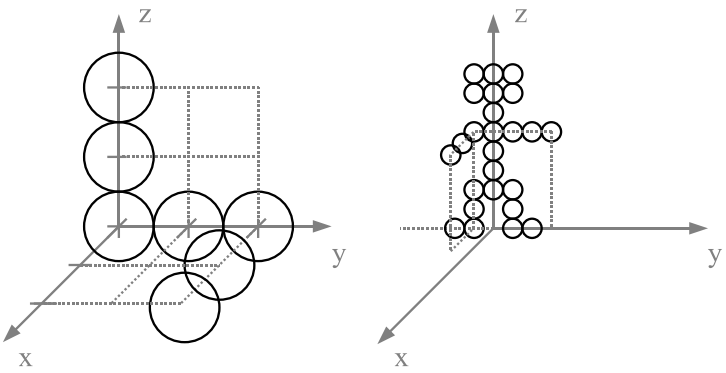

Figure 7.5: Asymmetrical particles used for the calculations. The left particle ("snake particle"), is an aggregate of 7 homogeneous identical spheres. The right one ("Mr Sanchez"), is made of 25 of these spheres.

particles "snake particles". The refractive index is set to $m = 1.5 + i0.001$, and the aggregates are randomly oriented. If we change the size of the aggregates, while keeping constant the wavelength of the incident light, the DCP changes as shown in Figs. 7.8 to 7.10.

From these plots, we can obtain three important conclusions. The first one is that the DCP becomes generally higher (in absolute value) as the size parameter grows from zero to a maximum. In this case the maximum occurs for $x = 1.8$. For larger values of x, the mean amplitude of the curve of the DCP gradually tends to zero, being reduced to almost zero at $x = 10$. Obviously, for very small particles, the DCP is close to zero, as corresponds to the Rayleigh regime (see Sec. 3.6.2). The second conclusion is that, as the size parameter increases, the curve of the DCP always becomes more complex, i.e. the number of maxima and minima becomes higher, so that the DCP reaches both positive and negative values in a small range of scattering angles for large aggregates. A possible explanation for this phenomenon might be the following: when the size of the grains increases so that the size of the monomers is comparable to the wavelength, light is able to perceive the entire structure of the target, resulting in a more complex DCP curve. The third and most important conclusion is that it is possible to produce a DCP of the order of the observed values or larger, with a sample of particles in random orientation, at least for the asymmetrical model particles that we used. This result is based on test particles whose shape is surely very different from the real particles, but as the DCP obtained is so large, we cannot rule out the possibility of obtaining large values also for some kind of

real grains.

7.5.2 Size distribution

In the previous section, we considered samples of identical particles. In a real sample, however, particles of many different sizes coexist, and the scattering matrix of the whole sample is the sum of the matrices corresponding to the individual particles, weighted by the size distribution. According to this, we investigated whether the DCP given by a sample of model aggregates of different sizes is much smaller than the observed values. For this purpose, we took the results of section 7.5.1 and some additional sizes, and we calculated the DCP of the sample from the size-averaged elements of the scattering matrix. To this end, we used a power-law size distribution with exponent

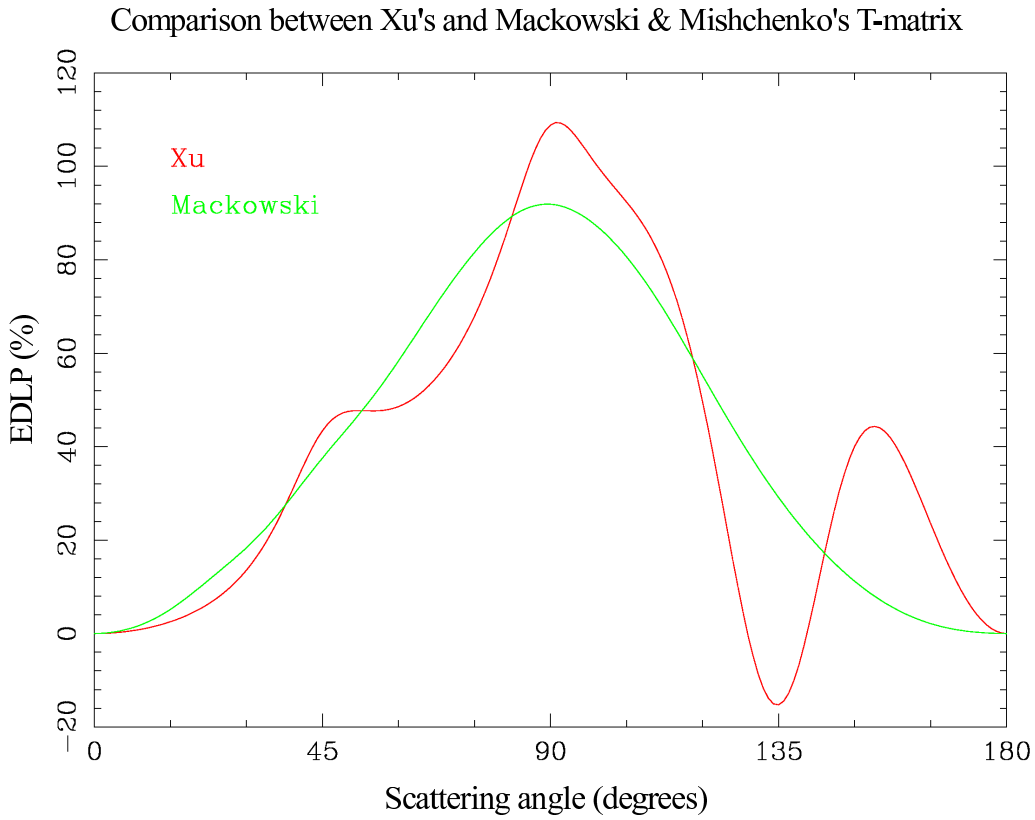

Figure 7.6: $EDLP$ as a function of the scattering angle, calculated with Xu's and Mackoski & Mishchenko's T-matrix codes, for the particle defined on the right panel of Fig. 7.5, in random orientation. The size parameter of all monomers is $x = 1$ ($X = 1.913$), and m=1.5+i0.001.

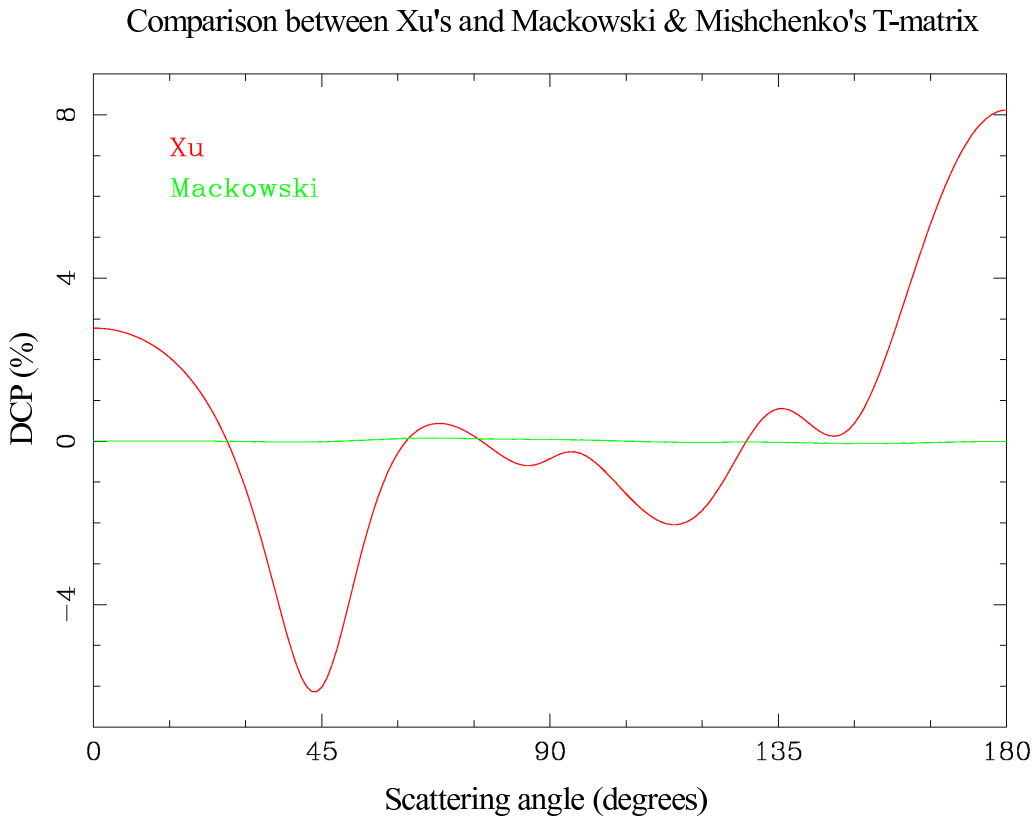

Figure 7.7: DCP as a function of the scattering angle, calculated with Xu's and Mackowsi & Mishchenko's T-matrix codes, for the particle defined on the right panel of Fig. 7.5, in random orientation. The size parameter of all monomers is $x = 1$ ($X = 1.913$), and $m = 1.5 + i0.001$.

-3, which is within the range of the values inferred for cometary dust (see Sec. 2.4). Progressively increasing the number of elements in the average led us to conclude that 26 different sizes, between 0.046 μm and 1.5 μm, are enough to achieve convergence of the DCP for the snake-like aggregates. Most of the points of the size distribution were concentrated in the range of small radii, where the distribution function changes more rapidly.

In Fig. 7.11 we show that, even when we have a size distribution, we obtain an appreciable DCP, that reaches a maximum of about 0.13%. This value is of the order of the observations (see Chap. 4), so we cannot rule out single scattering by optically inactive asymmetrical particles in random orientation as a significant mechanism producing CP in different astrophysical environments. It is still possible that some kind of real particles make a significant contribution by this mechanism to the observed DCP. In order to

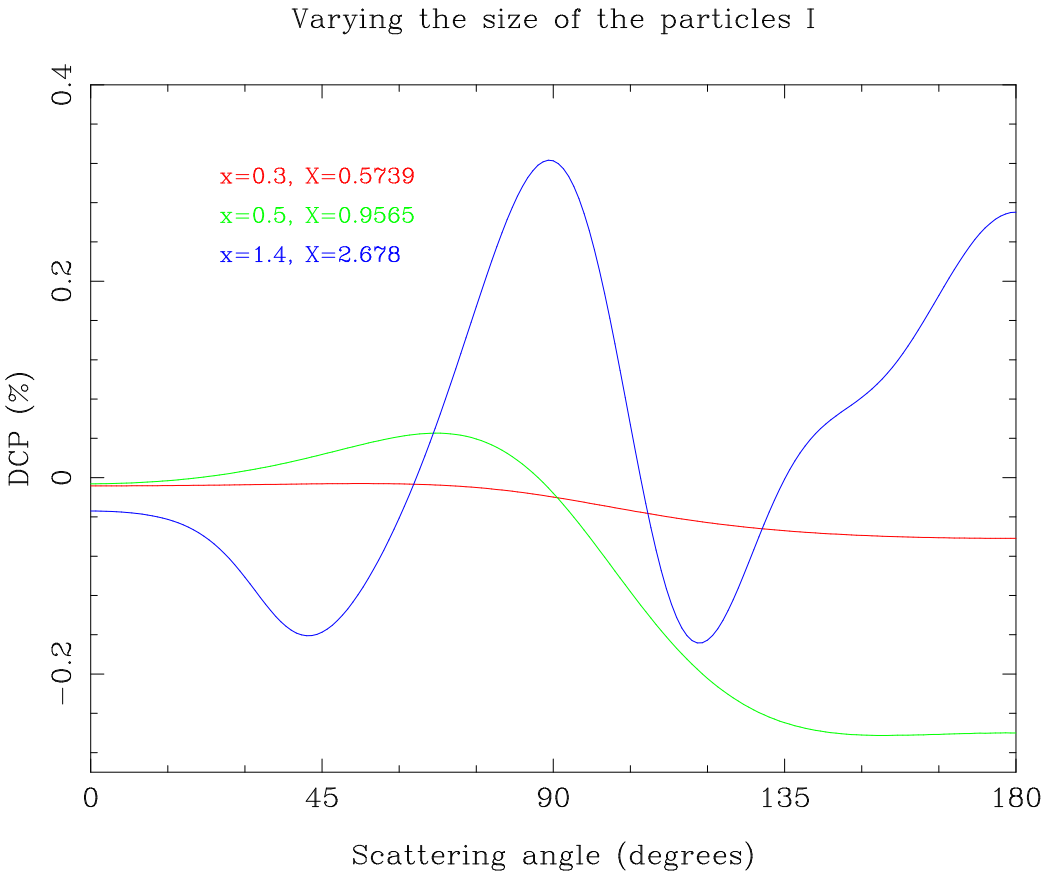

Figure 7.8: DCP as a function of the scattering angle for different size parameters. The particles are snake-like aggregates composed of 7 monomers (see left panel of Fig. 7.5). The refractive index is $m = 1.5 + i0.001$. The curves correspond to small size parameters (Rayleigh domain), so the values of the DCP are close to zero.

search for those particles, we have to find out what is the essential property of the particles of Secs. 7.5.1 and 7.5.2 that makes them to give such a large DCP.

7.5.3 Changing the absorption

In Secs. 7.5.1 and 7.5.2 we used a refractive index that is typical for silicates at visible wavelengths. The reason is that silicates have been clearly identified as one of the main components of dust in comets (see Sec. 2.3). However, amorphous carbon, which has a higher value of $Im(m)$, is an important component of cometary dust too. In this section, we present an analysis of the sensitivity of the DCP to variations in the imaginary part of the

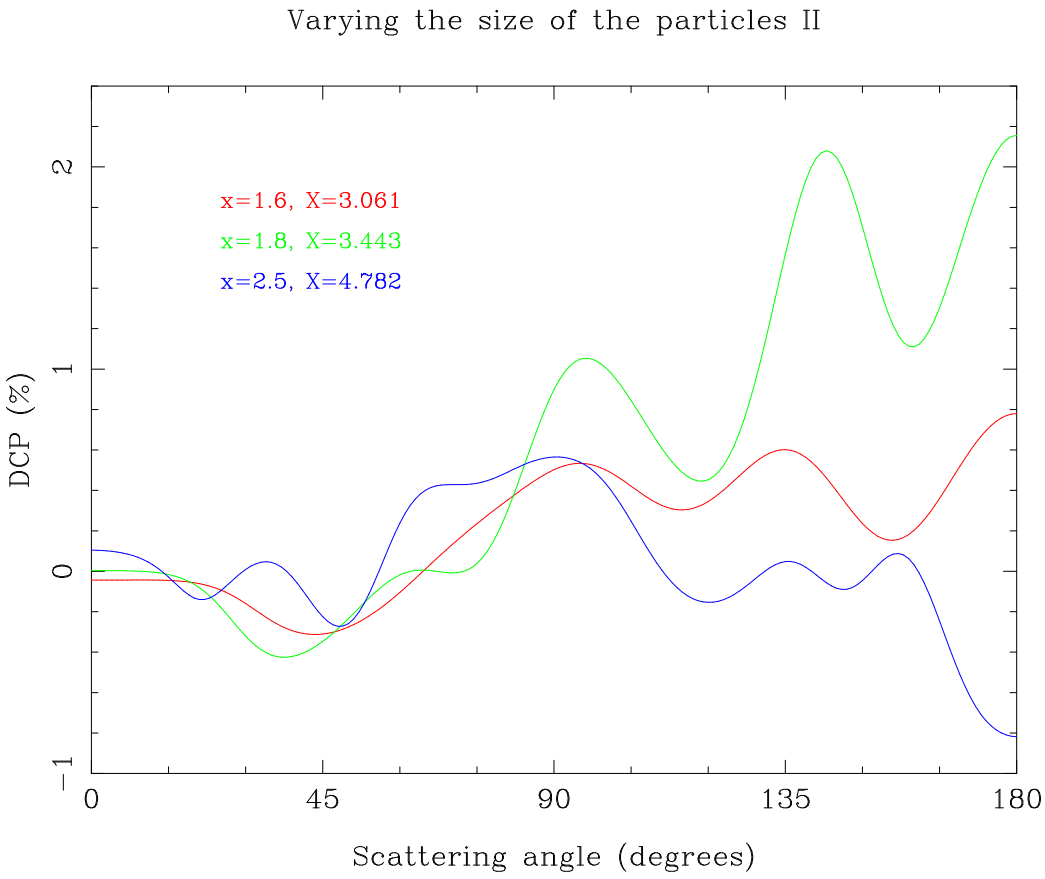

Figure 7.9: DCP as a function of the scattering angle for different size parameters. The particles are snake-like aggregates composed of 7 monomers (see left panel of Fig. 7.5). The refractive index is $m = 1.5 + i0.001$. The curves correspond to the size parameters for which the highest values of the DCP are reached.

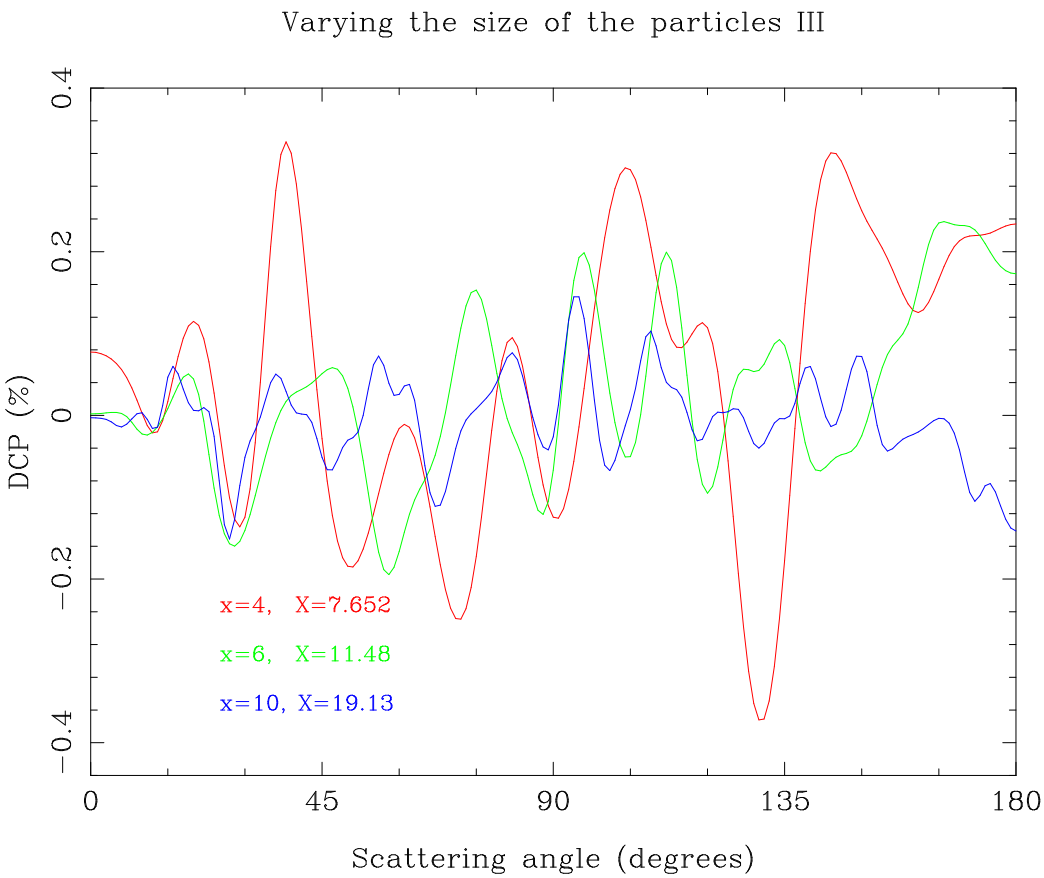

Figure 7.10: DCP as a function of the scattering angle for different size parameters. The particles are snake-like aggregates composed of 7 monomers (see left panel of Fig. 7.5). The refractive index is $m = 1.5 + i0.001$. The curves correspond to large size parameters.

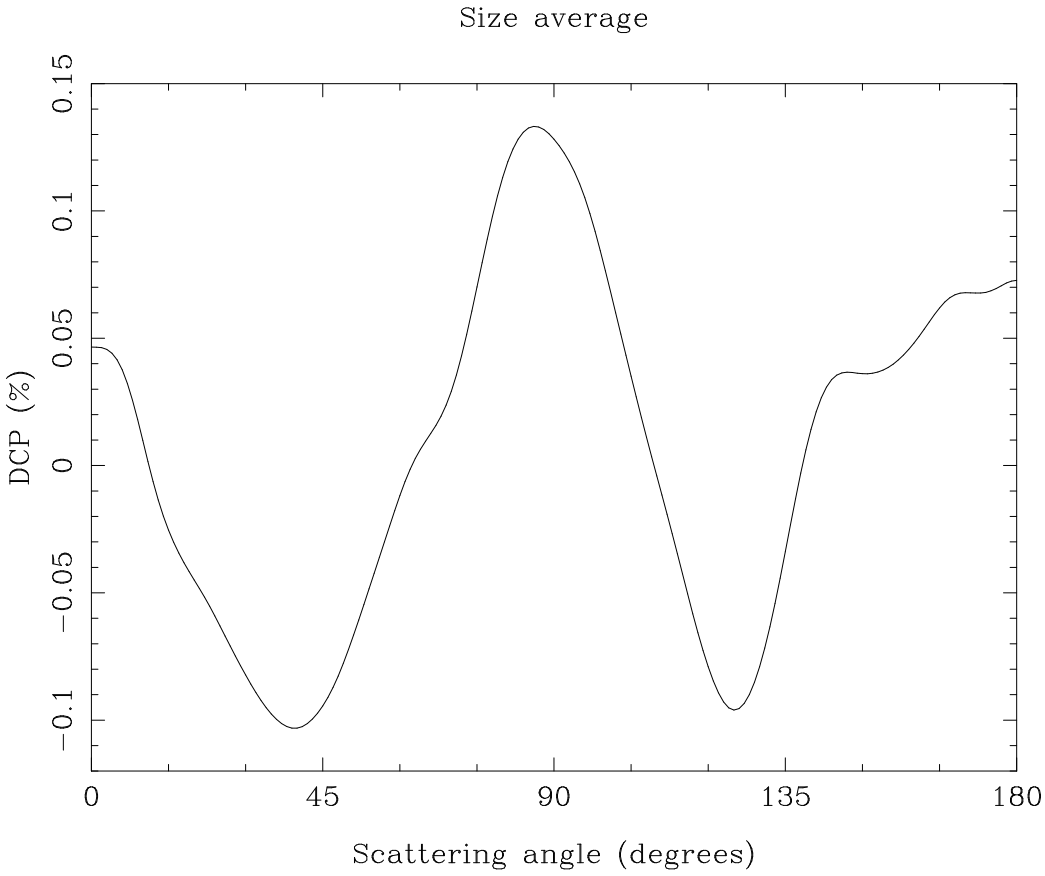

Figure 7.11: DCP as a function of the scattering angle for a power-law size distribution of particles with exponent -3. The particles are snake-like aggregates made of seven monomers (see left panel of Fig. 7.5). The refractive index is $m = 1.5 + i0.001$. The computations were performed for 26 sizes with r_{eq} between 0.046 μm and 1.5 μm, with a wavelength $\lambda = 0.5$ μm. Most of the used sizes are placed in the range of small radii.

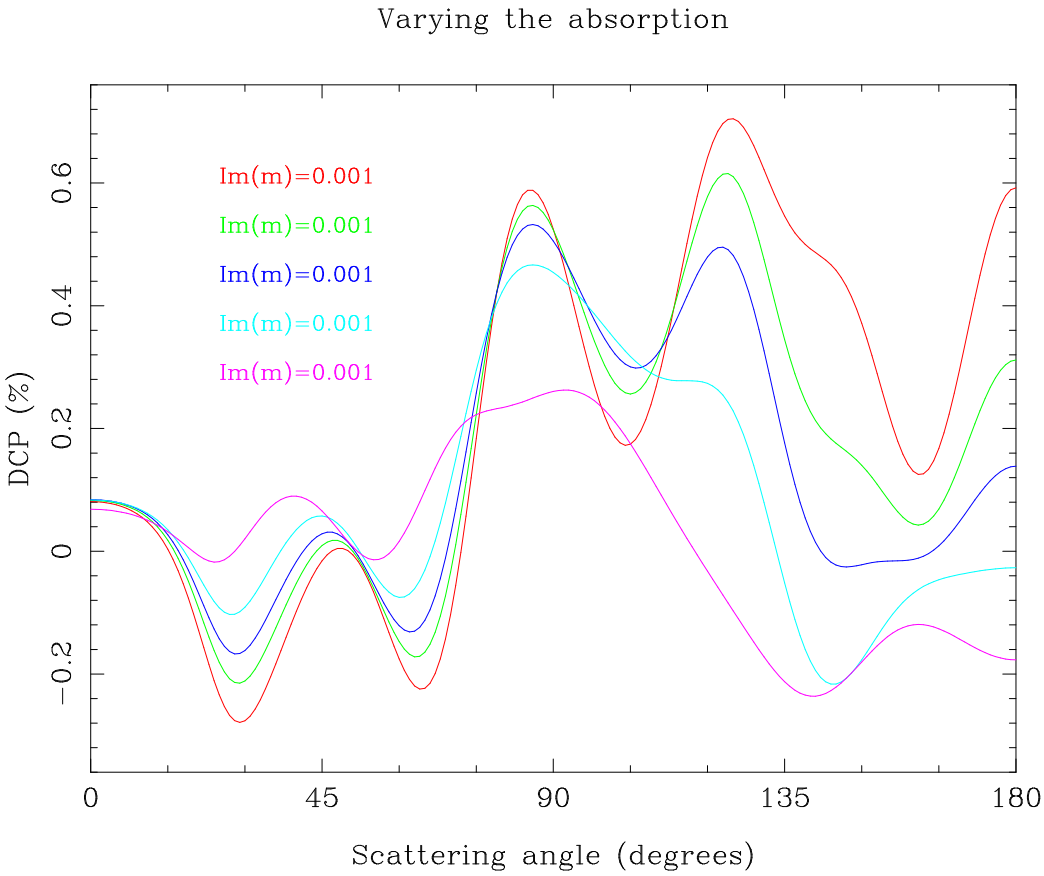

Figure 7.12: DCP as a function of the scattering angle for different absorptions. The particles are snake-like aggregates composed of 7 monomers (see left panel of Fig. 7.5). The size parameter of the monomers that form the aggregate is $x = 2$ ($X = 3.826$), and the real part of the refractive index is fixed to $Re(m) = 1.5$.

refractive index. For this purpose, we considered samples made of only one kind of particles (regarding shape) of a fixed size. The particles are again snake-like aggregates made of seven monomers (see left panel of Fig. 7.5). The size parameter of a monomer is $x = 2$, so $X = 3.826$. The real part of the refractive index is 1.5. We calculated the DCP as a function of the scattering angle for several values of the absorption, from $Im(m) = 10^{-6}$ to $Im(m) = 0.5$. The curves for $Im(m)$ smaller than 10^{-3} are not included in Fig. 7.12, since they are very close to the curve for $Im(m) = 10^{-3}$. We conclude from Fig. 7.12 that the curves of the DCP tend to zero as the absorption increases.

We also made some calculations for larger size parameters and we came

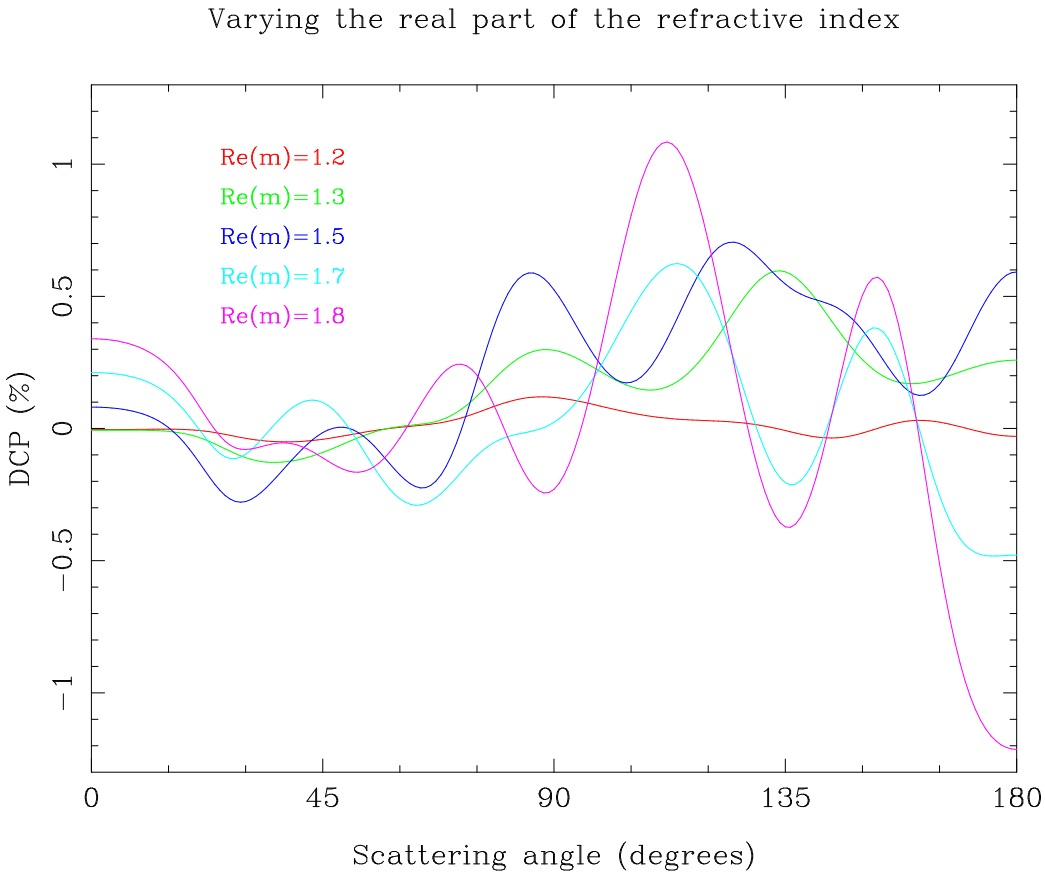

Figure 7.13: DCP as a function of the scattering angle for different values of the real part of the refractive index. The particles are snake-like aggregates composed of 7 monomers (see left panel of Fig. 7.5). The size parameter of the monomers that form the aggregates is $x = 2$ ($X = 3.826$), and the imaginary part of the refractive index is fixed to $Im(m) = 0.001$.

to the same conclusion.

7.5.4 Changing the real part of the refractive index

Regarding the real part of the refractive index, we performed a study similar to that in Sec. 7.5.3. The imaginary part was fixed to $Im(m) = 0.001$, and the real part varied from $Re(m) = 1.2$ to $Re(m) = 1.8$. The results are shown in Fig. 7.13. The behavior of the DCP in this case is exactly the opposite to that obtained by changing $Im(m)$, i.e., the values of the DCP become generally larger (in absolute value) as the real part of the refractive index increases.

When $Re(m)$ tends to one, we enter the domain of Rayleigh-Gans scattering [68], where the DCP must get close to zero for all scattering angles. This might be an explanation for the behavior observed in Fig. 7.13.

7.5.5 Changing the number of monomers of an aggregate of constant size

In this section we start studying to what extent the exact shape of the particles determines the shape of the curve of the DCP as a function of the scattering angle. As a first step, we analyzed the effect of changing the number of component monomers of the aggregate, keeping the size of the whole particle constant. Again we took a snake-like shape, but this time the aggregates were composed of 4, 13, 16 and 25 monomers respectively (see Fig. 7.14).

The size of the aggregates was $X = 3.826$ and we chose $m = 1.5 + i0.001$. The results (see Fig. 7.15) clearly tell us that the higher the number of component monomers is, the closer to zero the mean amplitude of the DCP becomes. This behavior suggests that we would need aggregates made of only a few monomers to reproduce high values of DCP. We can also see in Fig. 7.15 how the complexity of the curves increases with the number of monomers.

A possible explanation for the results of this section may be the following. The peaks of the curves of the DCP are due to resonances in the interference of light after interacting with the asymmetrical particle. These resonances largely remain after averaging over all possible orientations. The number of peaks of the curves of the DCP depends on the number of monomers composing the aggregate. Indeed, as the number of monomers of the particle increases, the number of maxima and minima of the curves of the DCP also increases. The scattering angle of the peaks and their amplitudes might be determined by the spatial distribution of the monomers in the aggregate and the relation between the size of the monomers and the wavelength. In fact, the mean amplitude of the curves decreases as the monomers become smaller. This could be due to the fact that the optimal size-wavelength relation for the resonance is lost.

7.5.6 Monomers of different sizes in the same aggregate

So far, we have just used aggregates in which all constituent spheres have the same size. It might be possible that the results we are obtaining are due

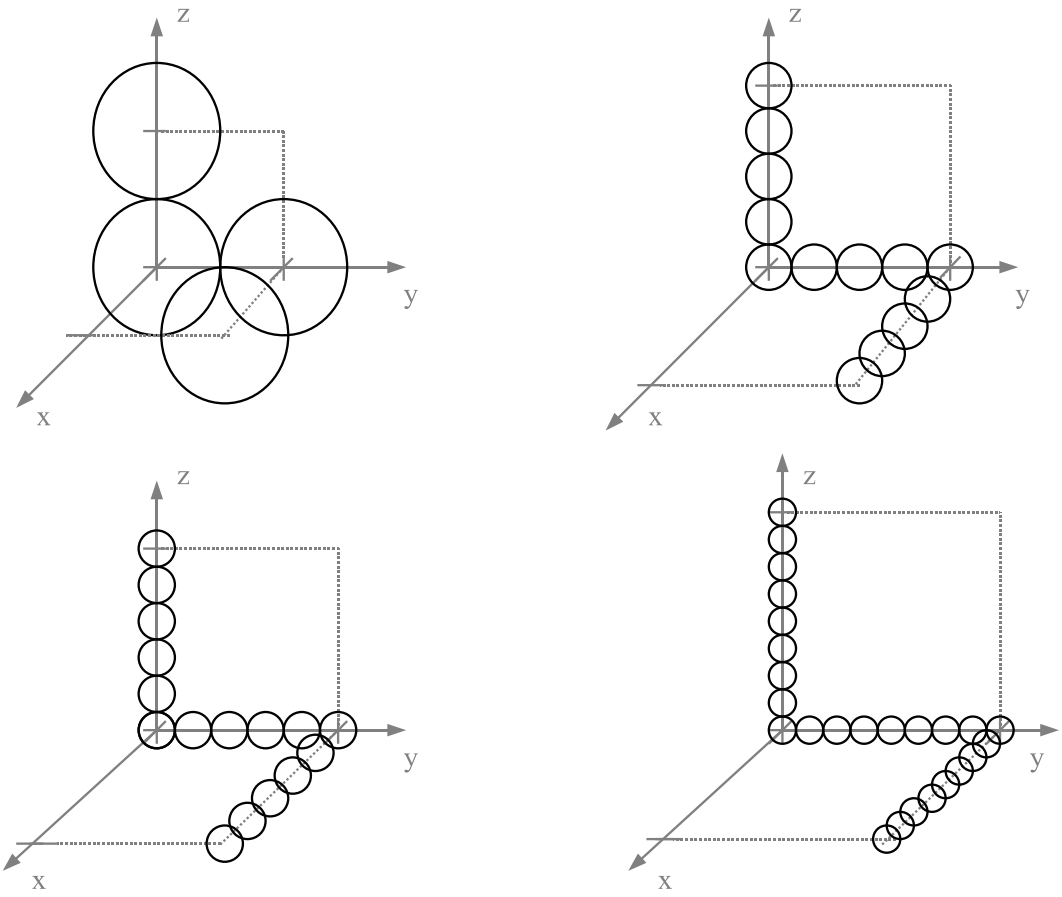

Figure 7.14: Snake-like aggregates with different numbers of monomers. The size parameter is the same for all aggregates, so the size parameter of the monomers decreases as the number of monomers increases. Aggregates made of 4, 13 16 and 25 monomers are shown.

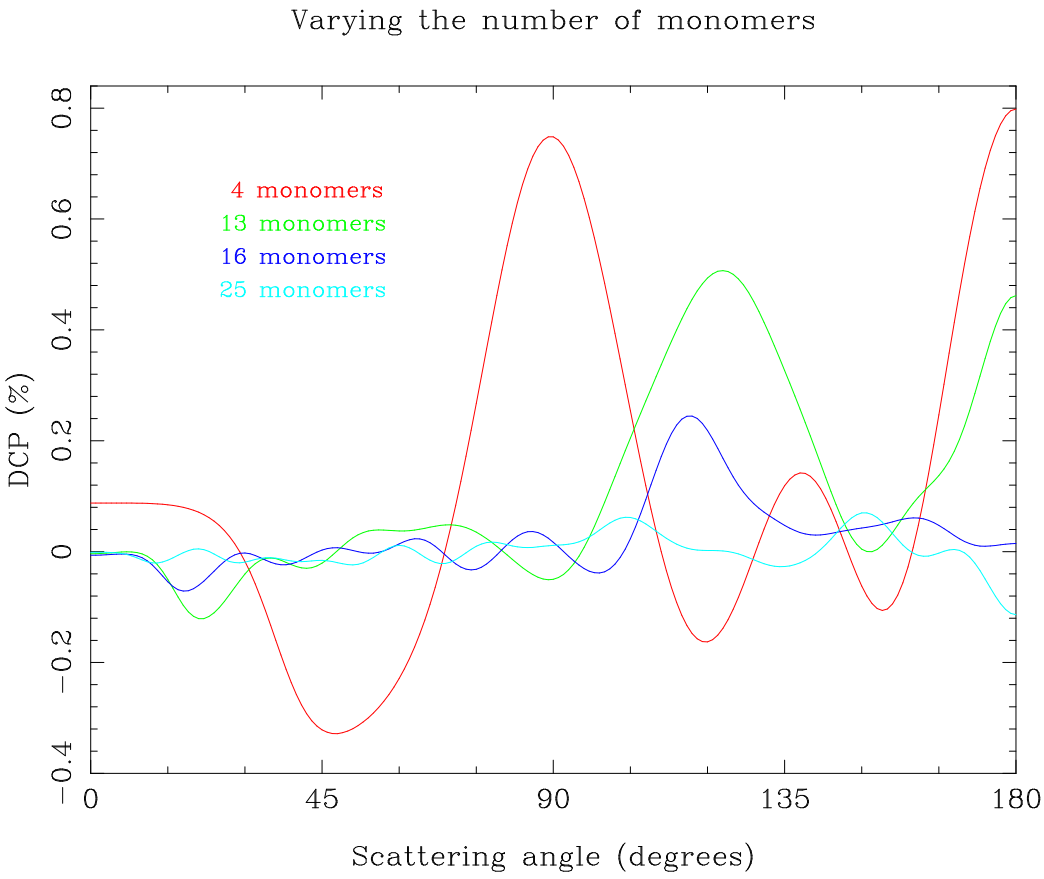

Figure 7.15: DCP as a function of the scattering angle for snake-like aggregates composed of different numbers of monomers (see Fig. 7.14). The size parameter of the aggregates is fixed to $X = 3.826$, and the refractive index is $m = 1.5 + i0.001$.

to that particular feature of the particles. In order to check this possibility, we compared some of the results we already obtained with some other calculations for particles formed by monomers of different sizes. We built a particle made of monomers of tree different sizes, distributed as indicated in Fig. 7.16. The volumes of the monomers are $V_0 \pm \Delta V$, where V_0 is a certain reference volume, and ΔV is 0%, 10%, 20%, 30% and 50%. Note that all particles have the same volume for the comparison to make sense.

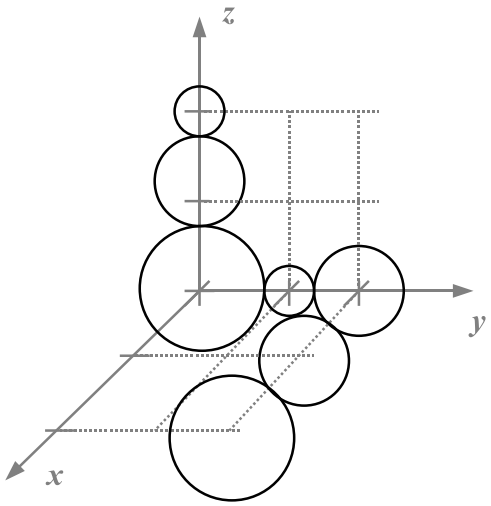

Figure 7.16: Aggregate formed by 7 monomers of different sizes. There are spheres of tree volumes: V_0, $V_0 + \Delta V$ and $V_0 - \Delta V$, and the total volume of the particle is the same as if the volume of all monomers of the aggregate was V_0.

In Fig. 7.17 we can see that there are not important differences (either qualitative or quantitative) between the results corresponding to $\Delta V = 0\%$, $\Delta V = 10\%$, $\Delta V = 20\%$ and $\Delta V = 30\%$. However, somewhere between $\Delta V = 30\%$ and $\Delta V = 50\%$, the DCP suddenly goes to zero for all scattering angles. An explanation might be that the observable features of the DCP curves are due to resonances that depend on relations between some substructures of the particles. For monomers with very different sizes those relations are not fulfilled and the resonances disappear. This result gives us a certain freedom in the configuration of the aggregate, allowing us to consider more realistic particles without loosing the high values for the DCP.

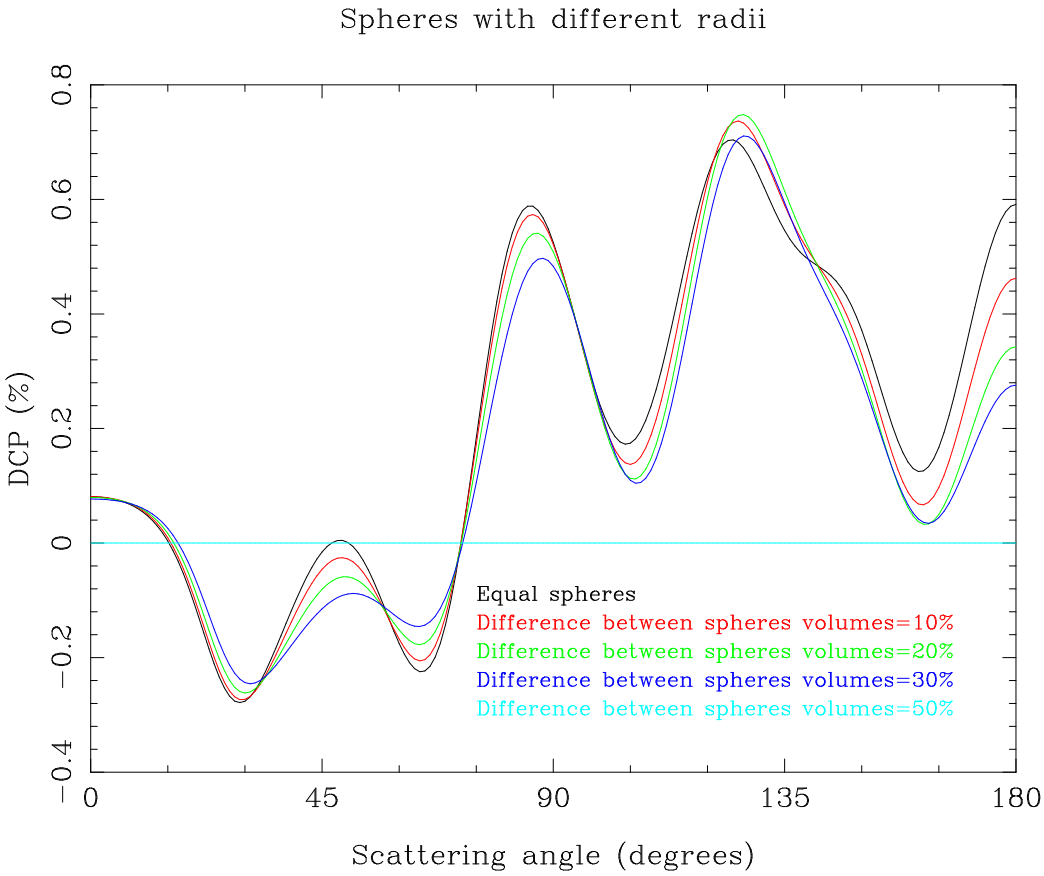

Figure 7.17: DCP as a function of the scattering angle for snake-like aggregates made of differently-sized monomers (see Fig. 7.16). The size parameter of the aggregates is fixed to $X = 3.826$, and the refractive index is $m = 1.5 + i0.001$. The percentages indicated in the legend are the differences in volume among the monomers composing the aggregate.

7.5.7 Changing the shape

The last step is to change the shape by a completely different one, and compare the results with the ones coming from the snake-like shape for some sizes (Sec. 7.5.1). The new shape is that of the *Mr Sanchez* particle, described in the right panel of Fig. 7.5. It is made of 25 identical homogeneous spherical monomers.

Figs. 7.18 and 7.19 show the results. In the first one we can see that for small size parameters *Mr Sanchez* produces in general a lower DCP than the *snake* particle. However, for large sizes, the mean amplitude of the curves of the *snake* particle and *Mr Sanchez* are comparable, as shown in Fig. 7.19.

For a given size of the whole aggregate, the monomers composing *Mr*

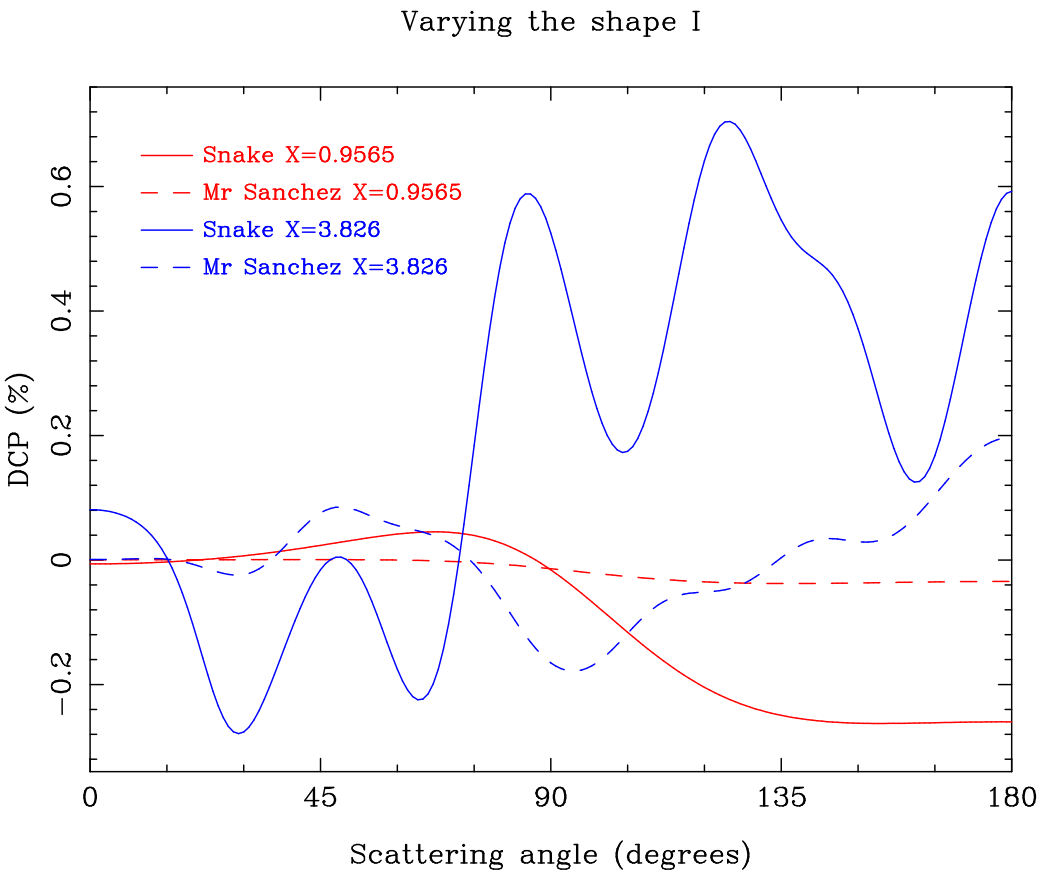

Figure 7.18: DCP as a function of the scattering angle for two different shapes and two different sizes. The refractive index is $m = 1.5 + i0.001$. The curves correspond to small size parameters.

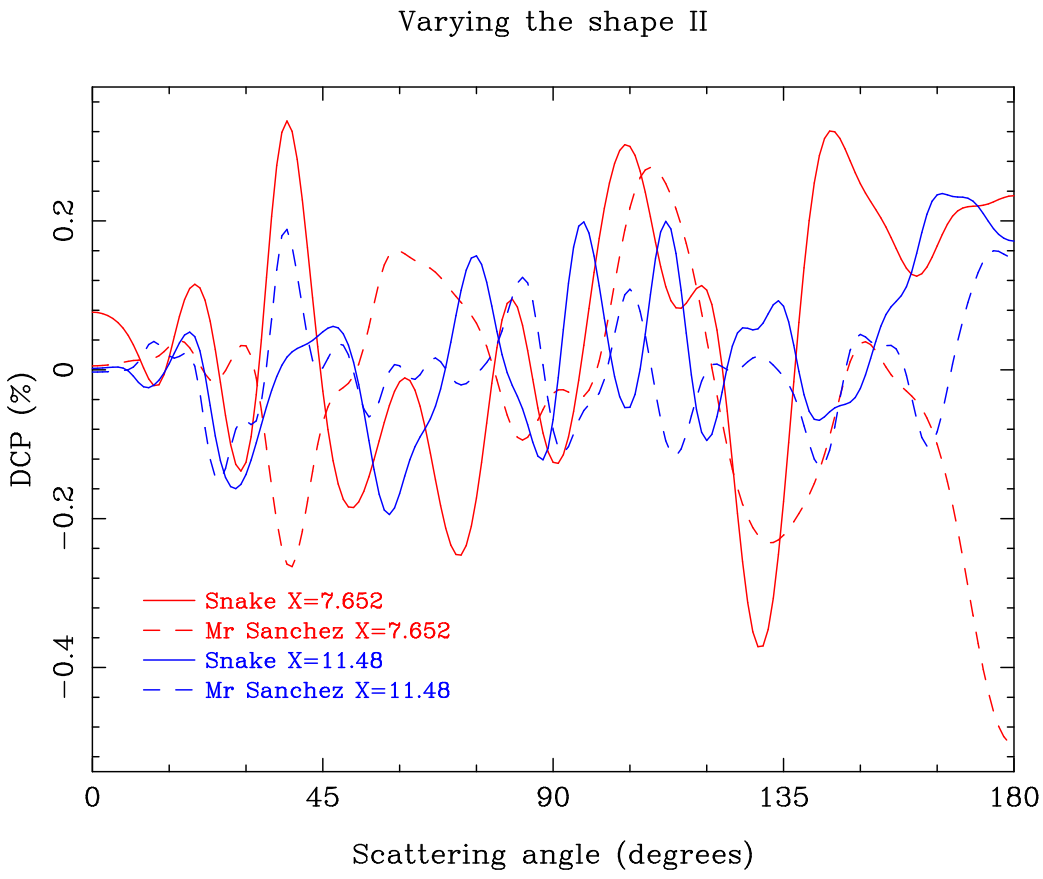

Figure 7.19: DCP as a function of the scattering angle for two different shapes and two different sizes. The refractive index is $m = 1.5 + i0.001$. The curves correspond to large size parameters.

Sanchez are substantially smaller than those of the snake-shaped particle. Consequently, if the argument posed in section 7.5.5 is valid, we should always obtain a smaller amplitude for the curve of the DCP corresponding to *Mr Sanchez* than the one corresponding to the *snake*. However, the amplitudes are comparable for large size parameters. An explanation could be that for large sizes, the groups of monomers of *Mr Sanchez*, namely his head, his arms and his legs work as a monomer of a size close to the optimal for the resonance.

This theory suggests that it might be possible to obtain large values of the DCP for samples of real particles if their shape is asymmetrical and the substructures responsible for the asymmetry are comparable in size to the wavelength.

7.6 Primary and secondary peaks

A common explanation to results given in Secs. 7.5.1, 7.5.2, 7.5.5, 7.5.6 and 7.5.7 has been already suggested within the discussions corresponding to some of those sections. Nevertheless, we would like to summarize that in the present section, and clearly define the concepts of primary and secondary peaks, because they will be used in the next chapter.

While increasing the size of particles for a fixed wavelength, two important features appear in the curves of the DCP as a function of the scattering angle:

- When the size parameter of a grain rises over a certain limit X_p, the substructures of the particle that produce the asymmetry (groups of monomers), start to be non-negligible in size compared to the wavelength of the incident light. Then, some peaks (maxima and minima) appear in the curve: the *primary peaks*. Obviously, X_p is over the size parameters corresponding to the Rayleigh domain (see Sec. 3.6.2). The primary peaks are just a few, and both the number of them and the scattering angles they are located at, remain fixed when varying the size of the particles. The amplitude of these peaks do change with the size of the grains: it is maximum when an optimal ratio exists between the size of the substructures that produce the asymmetry in a particle and the wavelength of the incident light, and decreases for smaller and larger sizes.

- If we keep increasing the size of the grains up to a size parameter $X_s > X_p$, other features appear in the curve: the *secondary peaks*. This happens when the size of the individual monomers becomes non-negligible compared to the wavelength. The number of these peaks

systematically increases while the size of the grains rises. The scattering angles they correspond to, are not fixed, but they change with the size of the grains. The amplitude of the secondary peaks is maximum when an optimal ratio exists between the size of the individual monomers of an aggregate, and the wavelength. For the model particles studied in the present chapter, the amplitudes of the secondary peaks are smaller than those of the primary peaks.

Based on the above description, primary peaks seem to be due to resonances by the substructures of the particles that produce the asymmetry, and secondary peaks seem to correspond to resonances between the monomers.

Primary and secondary peaks, as described above, are an explanation of the appearance and evolution of the different features of the curves of the DCP as a function of the scattering angle, while increasing the size of the grains (Sec. 7.5.1). They also can explain the result of the size average in Sec. 7.5.2: As the secondary peaks appear at different scattering angles for different sizes, they vanish in the average when enough sizes are considered. On the contrary, primary peaks always appear at the same positions, so they remain after adding the scattering matrices corresponding to different sizes. As for both the size average and the case of $X = 2.678$, the DCP curves are exclusively due to the primary peaks, the plot in Fig. 7.11 looks quite similar to the blue line of Fig 7.8: same number of peaks, with the same shape at the same positions appear at both plots. Increasing the number of monomers of the snake-like particle in Sec. 7.5.5 makes the primary peaks to disappear because the optimal size ratio between the substructures that produce the asymmetry in the particle and the wavelength is lost. At the same time, more secondary peaks arise while more monomers are added to the particle, because new resonances appear. Using monomers of very different sizes to form the grains makes all resonances to disappear, so both, the primary and secondary peaks vanish.

7.7 Conclusions

- For the snake-like shape with seven monomers and $m = 1.5 + i0.001$, the mean amplitude of the curve of the DCP is close to zero for small size parameters (as corresponds to the Rayleigh domain), and then grows as the size parameters of the monomers increases to $x = 1.8$, in which case a maximum larger than 2% is found. When the size parameter becomes larger than $x = 1.8$, the amplitude decreases gradually, becoming essentially zero for $x = 10$.

- For the snake-like shape with seven monomers and $m = 1.5+i0.001$, the complexity of the curves of the DCP increases always when increasing the size of the particle.

- Single scattering of optically inactive asymmetrical particles in random orientations can give large values of the DCP of the scattered light (more than 2%), at least for a snake-like aggregate composed of seven spherical monomers with $m = 1.5 + i0.001$.

- If we use a typical power-law size distribution, the curves of the DCP corresponding to snake-like aggregates made of 7 monomers with $m = 1.5+i0.001$ still show values of the DCP of the order of the observations ($\approx 0.1\%$ or less).

- Increasing the absorption of the particles makes the main amplitude of the curves of the DCP to decrease, at least for snake-like aggregates of seven monomers with $x = 2$ and $Re(m) = 1.5$. However, the effect is the opposite if the imaginary part of the refractive index is fixed to $Im(m) = 0.001$ and the real part is increased.

- By increasing the number of monomers of an aggregate, but keeping the whole size constant, the number of maxima and minima of DCP curves increases and the amplitudes of these decreases, at least for snake-like particles with $x = 2$ and $m = 1.5 + i0.001$.

- It is not necessary that monomers composing the aggregates are equal-sized to obtain high values of the DCP. In fact, the *snake* particle gives almost identical curves of the DCP even taking for the monomers volumes as different as V_0, $V_0 + 30\%V_0$ and $V_0 - 30\%V_0$.

- If the *snake* particle made of 7 monomers is compared to the *Mr Sanchez* particle (made of 25 monomers and more complex), the mean amplitude of the curve of the DCP is larger for the *snake* at small size parameters ($X \lesssim 4$), but it is comparable for both shapes if the size of the aggregates is large enough ($X \gtrsim 7$).

- The peaks of the curves of the DCP may be due to resonances. There exist two types of peaks: primary peaks (fixed number, at fixed scattering angles and due to resonances by the substructures that produce the asymmetry of the particle), and secondary peaks (the number increases with the size of the grain, not at fixed scattering angles and due to resonances by the monomers).

Chapter 8

Circular polarization of light scattered by irregular particles

Some of the results included in this chapter were published in [23] and presented in the *X Conference on Electromagnetic & Light Scattering by Non-Spherical Particles.*

Abstract

A collection of irregular aggregates of identical spheres was built by using a Monte Carlo implementation of a cluster-cluster aggregation model. The behavior of the DCP as a function of the scattering angle was studied for those particles. After averaging over a few sizes and shapes, the DCP rapidly tended to zero, so we deduced that the asymmetry of the particles cannot account for the observed DCP in comets.

8.1 Introduction

The results of the previous chapter did not definitively rule out the asymmetry of randomly oriented particles as the responsible mechanism of the observed DCP in comets, because the calculated values of the DCP were comparable to the observations, even when averaging over sizes for a specific model shape. As a consequence, a study regarding a collection of irregularly shaped particles must be carried out. It is obvious that averaging over a large number of randomly irregularly shaped particles will finally yield a zero DCP, because there will be always a particle similar to the mirror particle of some other, so mirror symmetry will be achieved in the sample. In the present chapter, we are not questioning this fact, but we are trying to asses how many different shapes are needed to obtain a asymthotic behavior of the DCP towards zero. For instance, if twenty or fifty different shapes

are enough, we can inmediately disregard this mechanism, but if a number larger than present in a comet is needed, the asymmetry of particles would make a significant contribution to the DCP of light scattered in comets.

8.2 Building the aggregates[1]

We again work with aggregates of identical spheres as in the previous chapter, because calculations of the scattering matrix of such particles is fast and accurate by using the T-matrix method along with the superposition theorem (see Sec. 7.4).

For the generation of the aggregates, we made a Fortran implementation of both a particle-cluster aggregation (PCA) and a cluster-cluster aggregation (CCA) Monte Carlo methods. The PCA process starts with a single sphere in a fixed position (see the upper part of Fig. 8.1). A new sphere is then attached to it in a random direction. From then on, the procedure consists of adding a new sphere to any of the previously added in a random direction. Then, it must be checked that the new monomer does not overlap with any of the others. If it does, the last aggregated sphere has to be removed, and a new attempt to aggregate a non-overlapping monomer is performed. For CCA, several PCA clusters are built first, and then they are joined together (see the lower part of Fig. 8.1). We stick them together in the following way: we set one of the clusters in the origin, and we put another one far away from the first (in such a way that they do not overlap), in a random direction. Then we make the second cluster to approach the part of the aggregate that is already formed, until both parts get in touch. For both PCA and CCA methods, the coagulation process finished when the maximum distance between any pair of monomers of the aggregate exceeds a certain upper limit (d_c for PCA and d_p for CCA). This criterion is realistic, because the actual limitation in the size of an aggregate is given by the maximum length of the particle: the larger this length is, the stronger the centrifugal force may become for the monomers at the edge. As the forces sticking together the monomers is constant, aggregates are broken as a consequence of their rotation when they exceed a certain size.

After building some random aggregates by both of these methods, we made some preliminar calculations of the DCP derived from single scattering by these particles in random orientation. We found that CCA clusters

[1]The cluster-cluster aggregation model presented in this section was included in the peer-reviewed paper by R. Vilaplana, J. Cantó, F. Moreno and D. Guirado entitled *The influence of particle shapes and sizes in the CO ice stretching mode*, accepted for publication in Earth, Planets and Space in 2009 [69].

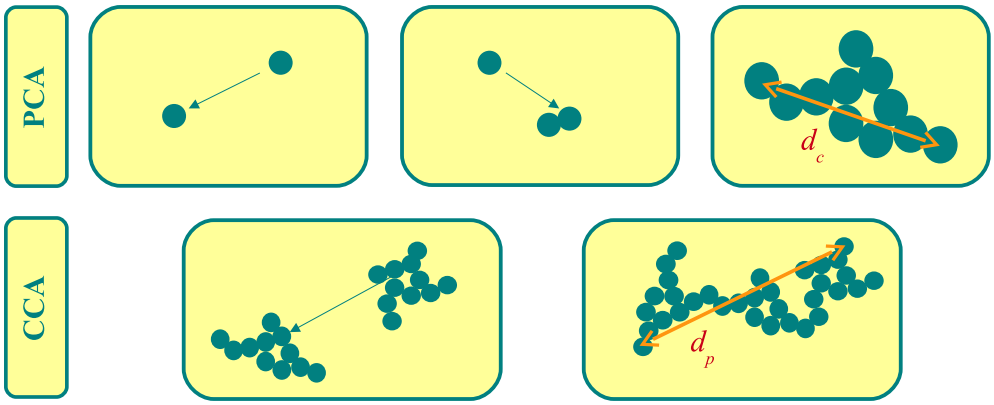

Figure 8.1: Models of aggregation to build the particles. For PCA, identical monomers are sticked together sequentially to the particle until the maximum distance between two monomers is larger than a certain limit d_c. For CCA, several PCA aggregates a joined together until the maxium distance between two monomers of the particle becomes larger than d_p.

give higher values of the DCP, which makes sense, because CCA produces aggregates with elongated substructures, which is favourable to the asymmetry of the formed particles. Fig. 8.2 shows the difference between a PCA and a CCA generated aggregate.

According to this, only CCA aggregates were considered for the rest of this chapter. Some of the generated CCA shapes used for calculations in Secs. 8.5 and 8.6 are shown in Fig. 8.5.

8.3 Description and validation of the numerical method

As we already stated in Sec. 7.4, the implementation of the T-matrix technique by Mackowski & Mishchenko [42] is the best choice for our calculations. Since only some checks for model particles have been performed on the code so far (see Sec. 7.4), we add at this point some comparisons between the results given by Mackowski & Mishchenko's T-matrix and Draine's DDA [17] for randomly built (irregular) grains. We made calculations for the three aggregates shown if Fig. 8.4. A silicate-like refractive index was set for the grains ($Im(m) = 1.5+i0.001$), for the same reasons as in the previous chapter (see Sec. 7.4).

Results on the DCP as a function of the scattering angle are shown in Fig. 8.5. A satisfactory agreement between both methods was found.

To assure the accuracy of the calculations, we adopted two aditional criteria:

- Checking that all calculated scattering matrices fulfill the coherency test (see Sec. 3.6.3).
- Imposing the same criterion for stability of the calculations as in the previous chapter (see Sec. 7.4).

8.4 Some examples for individual particles

Let us take any of the generated irregular aggregates, for instance, the one shown in Fig. 8.6. We calculated the DCP of light scattered by this particle in random orientation as a function of the scattering angle for $m = 1.5 + i0.001$. Results for several sizes of the particle are shown in Fig. 8.7. We found a number of features in this plot, that we compared to the those corresponding to the snake-like model particle given in Fig. 7.2:

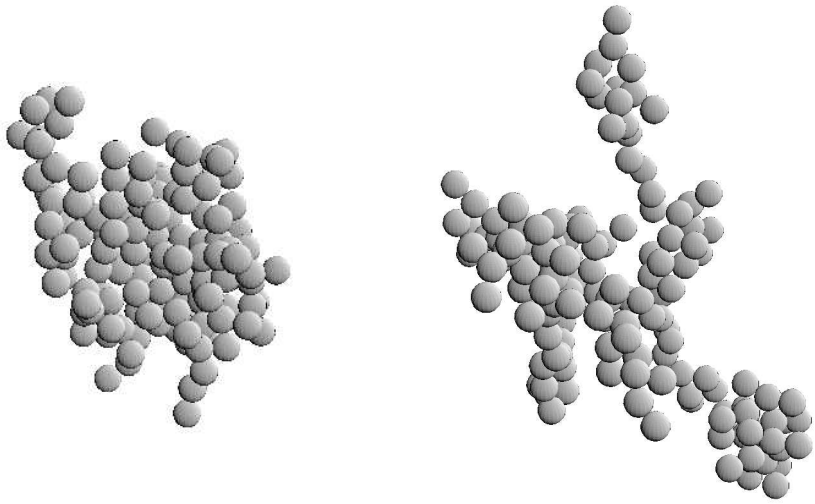

Figure 8.2: Two examples of randomly built aggregates. The particle on the left side is formed by 151 monomers, and it was constructed by the PCA method. The one on the right side is a CCA aggregate composed of 145 monomers. It is clear that PCA aggregates are more compact and close to a symmetrically shaped particle than CCA. CCA particles are more likely to be asymmetrical.

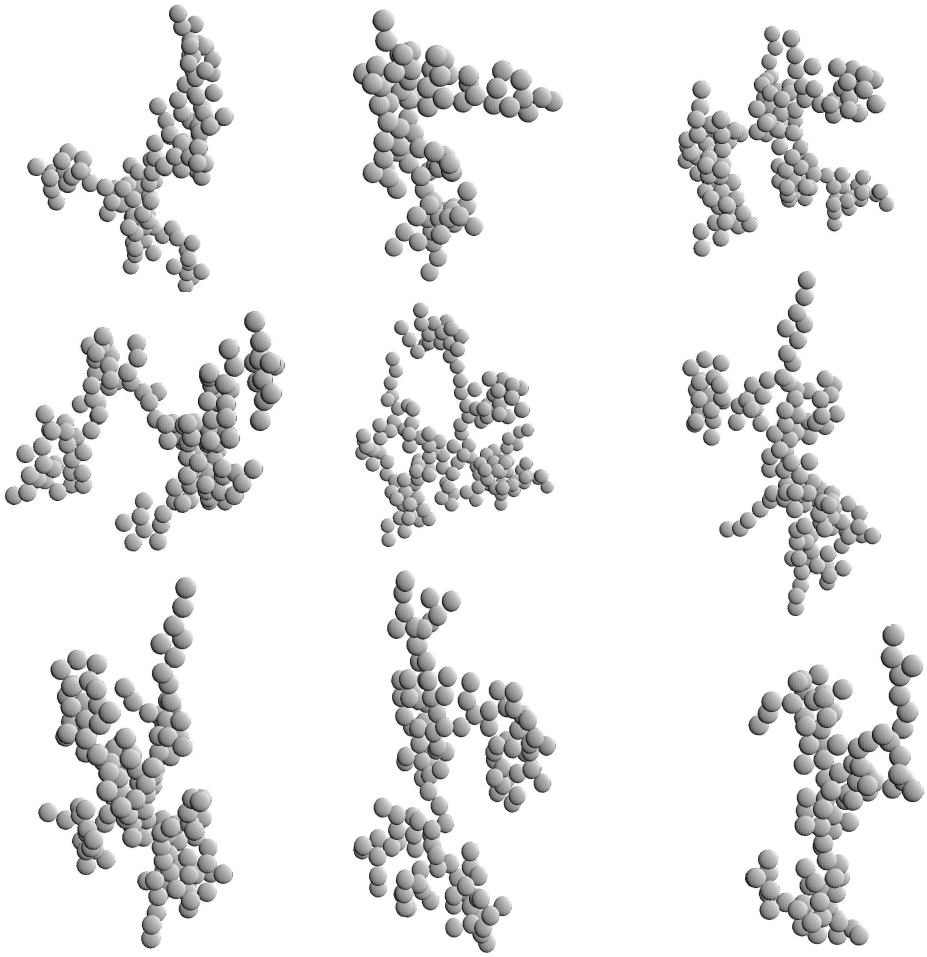

Figure 8.3: Some of the generated CCA clusters that were used for calculations of the DCP.

- At small sizes, the primary peaks appear for the irregular particle as well as for the model particle (see Fig. 7.8). It happens because the light starts distinguishing the substructures of the aggregate (groups of monomers) that produce the asymmetry, i.e., the size of such structures becomes not negligible compared to the wavelength of the incoming light.

- For larger sizes, the primary peaks increase their amplitude as in the case of the model grains (Fig. 7.9). The reason is that the size of the substructures producing the asymmetry of the particle becomes comparable to the wavelength.

- The secondary peaks arise for larger values of the size parameter, as in the model particle (Fig. 7.10). We explained this fact by assuming that for these sizes, the radius of the monomers is not negligible compared to the wavelength (light starts to distinguish the individual monomers of the particle, so a lot of resonances appear).

- All the above features are similarities between the DCP given by asymmetrical model particles and irregular scatterers. The difference is that, contrary to model aggregates, for irregular particles the primary peaks have smaller amplitude than the secondary. This may be due to the fact that the substructures producing the asymmetry are not as noticeable in the irregular particles as they were in the model grains.

8.5 Averaging over sizes for individual shapes

As in Sec. 7.5.2, we assumed a power-law size distribution of particles with an exponent -3. We considered one shape at a time and performed the size average of the scattering matrix of particles of that shape in random

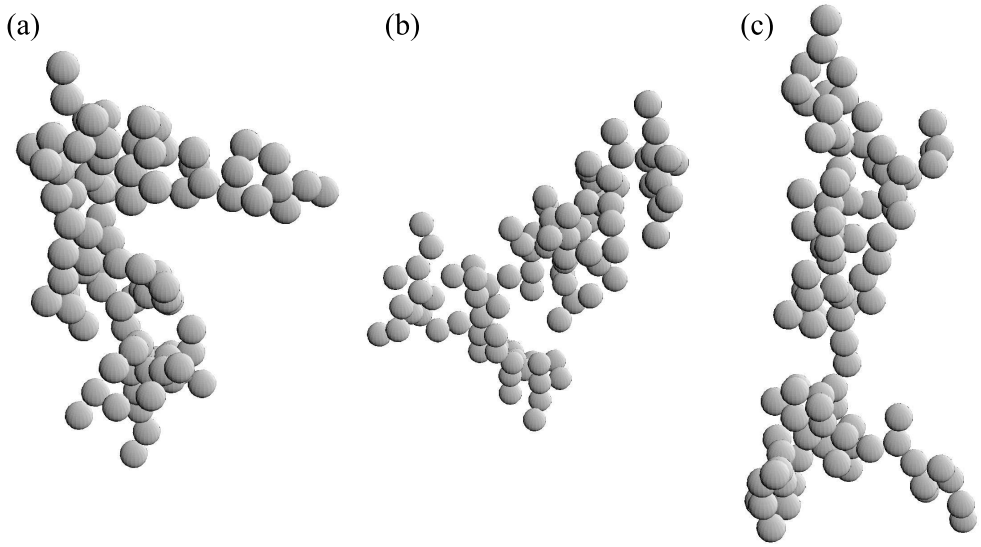

Figure 8.4: Three irregular aggregates of identical spheres. The size parameter of the monomers is $x = 0.26$ for all cases. Aggregate (a) is made of 93 monomers, so the size parameter of the whole particle is $X = 1.19$. For (b), the number of monomers is 96, what yields $X = 1.20$. Particle (c) has a size parameter of $X = 1.14$ because it is made of 83 monomers.

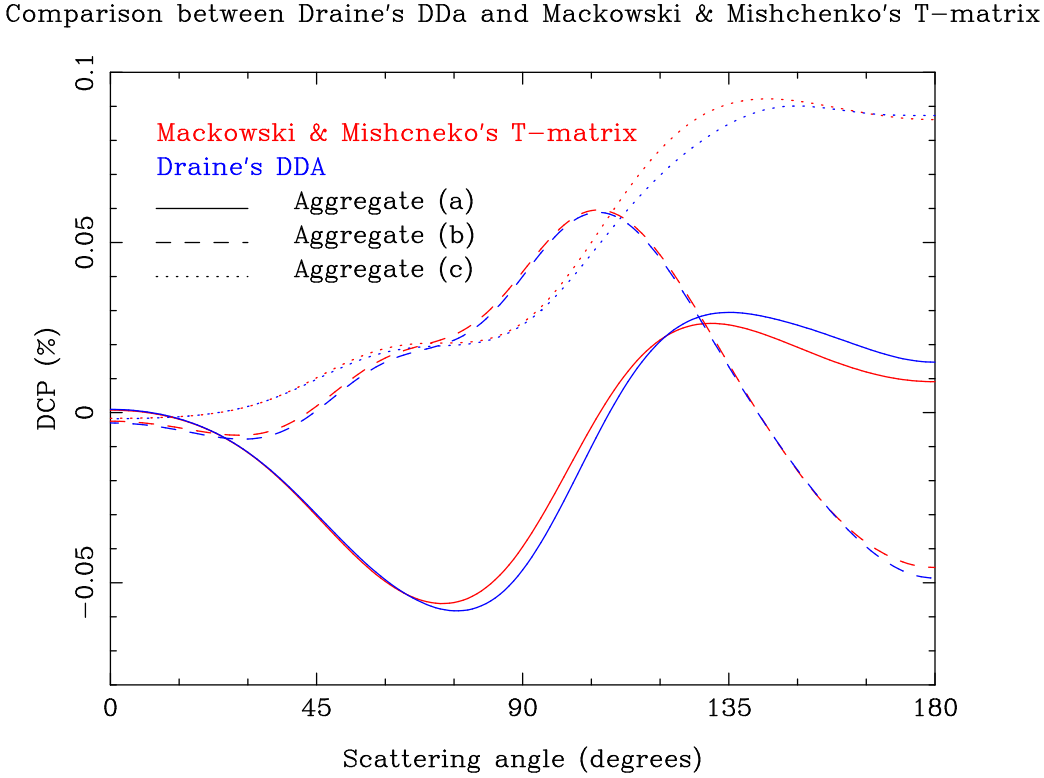

Figure 8.5: Comparison of Mackowski & Mishchenko's T-matrix code results with Draine's DDA calculations for the three irregular aggregates of identical spheres plotted in Fig 8.4.

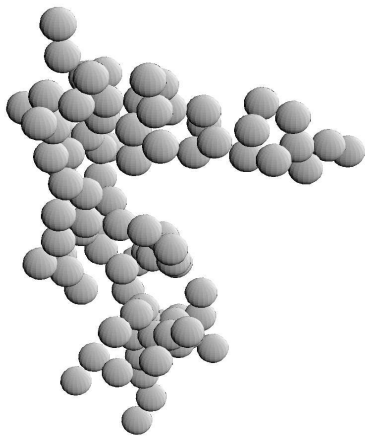

Figure 8.6: Randomly built CCA particle made of 93 identical monomers.

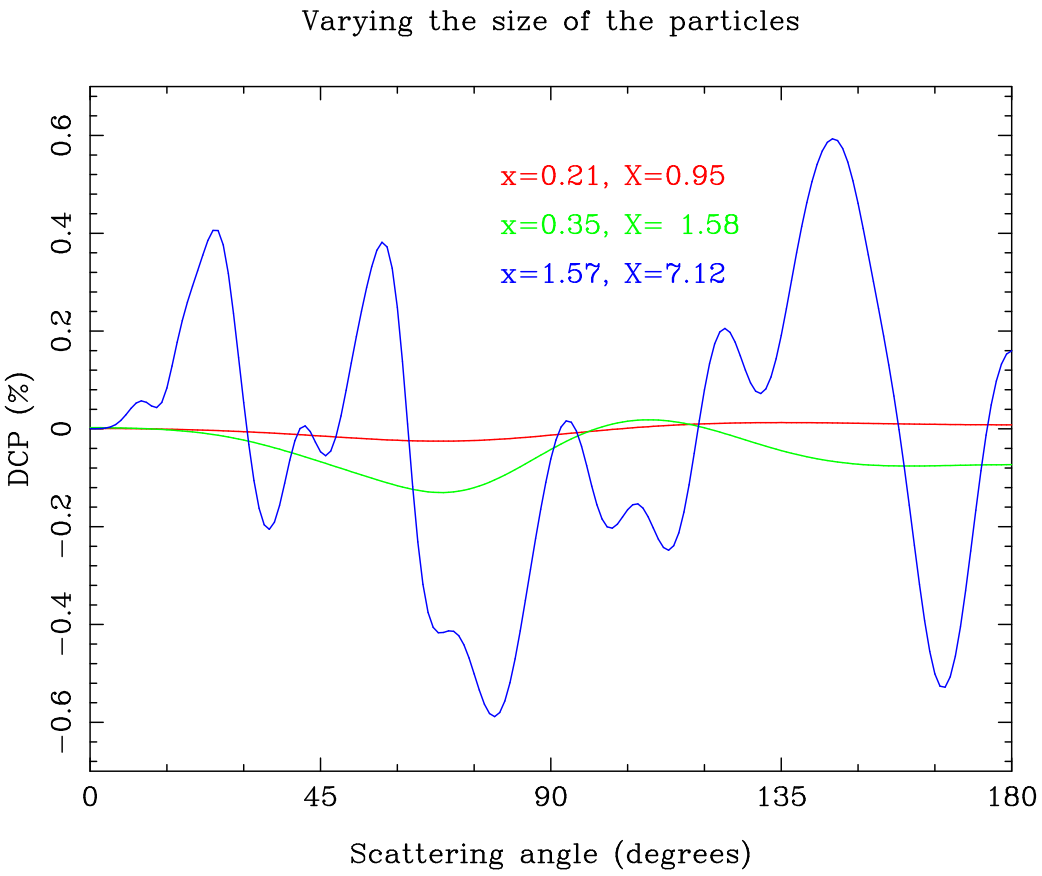

Figure 8.7: The DCP as a function of the scattering angle for particle given in Fig. 8.6. Three size parameters were considered for the same shape. The refractive index is set to $m = 1.5 + i0.001$.

orientation. In order to perform an adequate sampling of the chosen size distribution (power-law), we needed to consider a relatively larger amount of particles in the lower size limit than in the upper size limit, as the power-law function changes very rapidly for small sizes. Thus, we chose thirteen different monomer size parameters x as follows: : 0.21, 0.22, 0.24, 0.26, 0.29, 0.31, 0.35, 0.39, 0.45, 0.52, 0.63. 0.79 and 1.05. The size parameter of an aggregate made of $NMON$ monomers can be calculated as $X = (NMON)^{1/3}x$.

A representative example of the result after performing the average is given in Fig. 8.8. It corresponds to the particle shown in Fig. 8.6, with $m = 1.5 + i0.001$. The general appearance of the resulting curve is that of the primary peaks: they appear because they are always located at the same scattering angles and because they are produced by small particles, which have a larger weight in the average according to the power-law size

distribution. There is a little distorsion by the secondary peaks in the case of randomly built aggregates because for this case they have a larger amplitude than the primary ones. But they still do appear at varying scattering angles depending on the size of the aggregate, so they should not make any contribution to an average with a sufficiently high number of sizes sampling the size distribution. When the secondary peaks dissapear, only the primary peaks (with a small amplitude compared to model particles), remain. This means that randomly built aggregates averaged over sizes for a fixed shape produce a lower DCP that the model particles of Fig. 7.5.

Size averages were calculated for twelve different shapes. Table 8.1 shows the maximum DCP (in absolute value) obtained for each average.

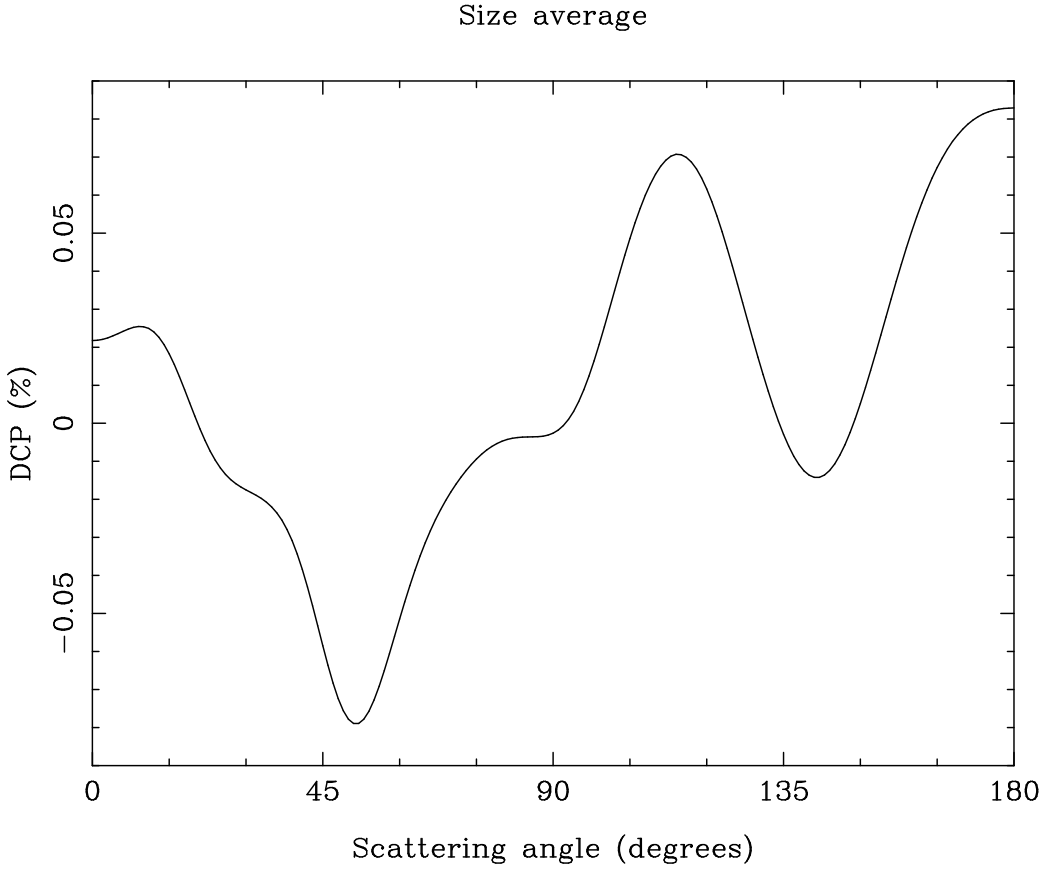

Figure 8.8: Average of the DCP as a function of the scattering angle, over thirteen sizes, all of them corresponding to the same particle shown in Fig. 8.6. The refractive index was set to $m = 1.5 + i0.001$.

Aggregate	max $\|DCP\|$ (%)
CCA1	0.083
CCA2	0.056
CCA3	0.308
CCA4	0.061
CCA5	0.082
CCA6	0.035
CCA7	0.170
CCA8	0.085
CCA9	0.106
CCA10	0.093
CCA11	0.094
CCA12	0.088

Table 8.1: Maximum values of the DCP as a function of the scattering angle, obtained by size averages of twelve individual different shapes.

8.6 Averaging over shapes the size averages

Results on the effect of averaging over 12 shapes the sizes averages are plotted in Fig. 8.9. Averaging the DCP curves over a number of shapes rapidly leads to zero values of the DCP because the primary peaks are located at different scattering angles for different shapes, so no constructive addition is made when workin with the shape-averaged sample. According to this, single scattering by randomly oriented irregular particles must be ruled out as the responsible mechanism of the observed DCP in comets.

8.7 Conclusions

- Primary peaks have smaller amplitudes in randomly built aggregates than in the asymmetrical model particles used in the previous chapter.
- Secondary peaks have larger amplitudes than primary ones in randomly built aggregates.
- The DCP of a sample of particles averaged over sizes for a fixed shape is mainly determined by the primary peaks, as in the case of model particles.
- A lower DCP arises from a size-averaged sample of randomly built aggregates of a fixed shape than for that of model grains.

- The DCP rapidly tends to zero when building a sample with just a few size-averaged shapes.
- Single scattering by asymmetrical particles in random orientation does not make a significant contribution of the observed DCP in comets.

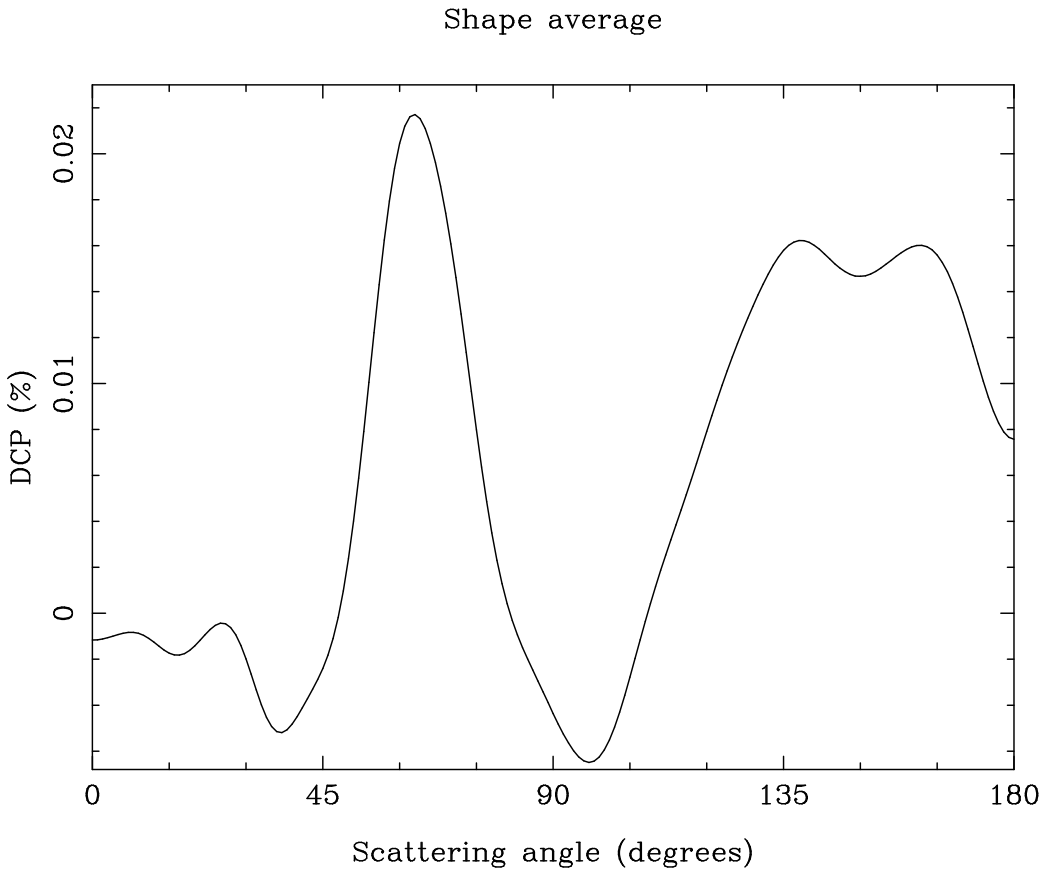

Figure 8.9: DCP as a function of the scattering angle for a sample averaged over twelve shapes, each one averaged over thirteen sizes.

Chapter 9

Circular polarization of light scattered by optically active materials

Although all studies reveal that optically active materials are not the main components of cometary dust, they must be carefully considered, because a small percentage of those materials in the composition of dust grains could be enough to circularly polarize the scattered light significantly.

Regarding mineral particles, searching for optically active materials means searching for crystalline minerals with a non-symmetric christalization system, as previously stated in Sec. 5.3. The only information we could obtain about such materials in comets, is given by Min et al. [48]: they deduced a volume abundance of 1.3% of chrystalline *enstatite* in Comet Hale-Bopp. Enstatite usually chrystallizes in the orthorrombic system, but at temperatures as low as those prevailing in cometary environments, it might be present in form of monoclinic chrystals, which are asymmetrical, so that they can circularly polarize light.

Organic materials [65], and in particular some amines [21], were found at very low abundances in the collected particles of Comet Wild 2 by Stardust mission. Some of these amines are optically active.

As explained above, there exist evidences that optically active materials are present in comets. Hence, the relevant question at this point is whether they are abundant enough to produce a DCP on the scattered light comparable to the observed. We decided not no initiate such an analysis, because the mechanism of optical activity do not match with the main features of the observations that we enumerated in Sec. 4.3: if optically active materials are present in cometary comae, in principle there is no reason to think that the distribution of them inside the coma is not homogeneous (in relative

abundance). If it is homogeneous, it makes no sense that the observed DCP decreases when increasing the aperture of the diaphragm, and there is no reason for the DCP to tend to zero in the vicinity of the nucleus. According to this, we decided to directly rule out this mechanism without any further consideration.

Nevertheless, we would like to remark that some authors claim that the observed DCP in comets has a predominant sign (see, e.g., [61]). Each optically active substance polarizes light always in the same sense, so the ocurrence of a predominant sense of CP would support the idea that the optical activity is the responsible for the observed DCP in comets. Rosenbush et al. [63] obtained only negative values of the DCP for different regions of the coma of Comet Hale-Bopp at a phase angle of 46°. Manset & Bastien [43] observed mainly negative values as well for the same comet, the phase angle varying from 47.4° to 40.0°. However, we would like to point out that observations at one single phase angle, or in a very narrow range of them, are not enough to assure that the CP has a predominant sense in a comet. There might be some dependence of the DCP on the phase angle. In fact, Comet C/1999 S4 (LINEAR) was observed by Rosenbush et al. [61] for eight phase angles varying from 60.9° to 122.1°, and it is clear from the plots presented in the paper, that the DCP is mainly possitive for the smallest phase angle, and then it progressively changes to negative as the phase angle increases. In conclusion, the predominant sign of the DCP in a comet could be due to a phase angle dependence.

Chapter 10

Monte Carlo model of radiative transfer in comets

Some results on the radiative transfer model described in the present chapter were published in [24] and presented in three conferences: *41st annual meeting of the Division for Planetary Sciences of the American Astronomical Society* (oral presentation), the *10th Asteroids, Comets, Meteors meeting* (poster presentation) and the *XI Conference on Electromagnetic & Light Scattering by Non-Spherical Particles* (oral presentation).

Abstract

A Monte Carlo model of radiative transfer in comets has been developed. It calculates the four Stokes parameters of the light scattered by particles in the coma, assuming a certain distribution of the grains around a spherical nucleus. By applying this model, non-negligible values of the DCP were obtained just by assuming conditions of multiple scattering by spherical optically inactive particles, and considering only light coming from a non central small region of the coma of the comet, an asymmetrical distribution of dust in the coma, or both. Nevertheless, these values are one or two orders of magnitude below the observed, at least for silicate-like spherical particles.

10.1 Introduction

We have already analyzed all mechanisms regarding the particles of cometary comae that are candidates to circularly polarize light. For none of those mechanisms was necessary to consider the structure of the comet (a nucleus and a certain distribution of particles in the coma). For the aligned particles (Chap. 6), it was enough to consider a single grain, to calculate how it is aligned and finally deduce that no CP could arise from grains that are aligned

that way. In Chaps. 7 and 8 we just had to calculate averaged scattering matrices of different ensembles of particles. To study the rest of the proposed mechanisms in Sec. 5.4, it is necessary to consider the whole structure of the comet: size and albedo of the nucleus, number density distribution of dust particles in the coma, etc. Our model must account for facts like the interaction of photons with the nucleus, the possibility of multiple scattering of a photon before it escapes from the comet and the possibility to observe light coming from a small region of the comet.

Available options for modelling were the *the doubling adding method* [28] and a *Monte Carlo* model. The doubling adding thecnique is not suitable for our study because it is meant for plane-parallel atmospheres. We could have made the approximation of local plane-parallel atmosphere in a comet, but that would not have permitted us to investigate the effects of the actual structure of the comet on the scattered light. Therefore, we chose the Monte Carlo technique. Our Monte Carlo model consist of launching photons into a certain target, tracking their evolution until they are extinguished, and recording all contributions they make to the outgoing light. Although large computational resources (especially computational time) are needed to run Monte Carlo codes, they are the most exact models to reproduce a real radiative transfer process. New multicore desktop computers offer the possibility of easily reaching statistical stability of the results of a Monte Carlo code in a reasonably short computational time. We think that Monte Carlo models should become the first option for modelling atmospheres in the near future.

There exist, at least, two previous approaches to the Monte Carlo modelling of radiative transfer in comets. The first one was developed by Salo in 1988 [64]. It consists of a model to compute the incoming energy to the nucleus of a comet, considering external solar radiation and internal infrared thermal re-radiation by the particles in the coma. The second one was developed by Moreno et al. in 2002 [53], and it deals with the outgoing radiation of comets when illuminated by the Sun. Althoug this model calculates the four Stokes parameters of light scattered in the comet, only results on the flux and $EDLP$ were presented, and no results were given on the DCP.

In this chapter, we present a similar model to that by Moreno et al., implemented in a new code built from the begining with better routines and numerical methods in order to improve the accuracy of the results and to reduce the computational time to achieve statistical stability. These improvements are necessary to get reliable results concerning CP, because, as seen in Chap. 4, we expect the calculated DCP to be close to zero.

10.2 Multiple scattering as a mechanism to produce circular polarization on a single photon

Let us consider one single photon of natural light singly scattered by a sample of particles fulfilling both the reciprocity and mirror symmetry conditions. The initial Stokes vector of the photon is proportional to $(1,0,0,0)^t$, and multiplying this vector by the scattering matrix of the sample (Eq. 3.90) gives us the Stokes parameters of the scattered photon, which is proportional to $(F_{11}, F_{12}, 0, 0)^t$. The DCP of the singly scattered photon is zero, because the last Stokes parameter V_{sca} is null (see definition in Eq. 3.56). It does not matter how many photons compose the incident light beam, after adding the Stokes vectors of all photons scattered in a certain direction (all with $V_{sca} = 0$), the DCP of the integrated light will be zero. This means that in conditions of single scattering, it is not possible to achieve any DCP even in the case that the system is asymmetrical around the direction of the incident light. This statement works as an example of the fact that the condition for CP given in 5.2 is just necessary, but not sufficient.

Nevertheless, multiple scattering can circularly polarize a single photon. The proof is simple: in the second scattering event, the scattering plane changes, so the Stokes parameters of the singly scattered photon must be transformed according to Eq. 3.59. After rotating the scattering plane by an angle i_{rot}, $(F_{11}, F_{12}, 0, 0)^t$ becomes $(F_{11}, F_{12}\cos 2i_{rot}, -F_{12}\sin 2i_{rot}, 0)^t$. Still the DCP is zero, as expected because I and V do not depend on the plane of reference (Sec. 3.3). Multiplying the new Stokes vector by the scattering matrix leads to:

$$(F_{11}^2+F_{12}^2\cos 2i_{rot}, F_{11}F_{12}+F_{22}F_{12}\cos 2i_{rot}, -F_{12}F_{33}\sin 2i_{rot}, F_{12}F_{34}\sin 2i_{rot})^t.$$

Thus, the DCP of a single photon may be different from zero after two scattering events.

Based on the last discussion, we have now two necessary conditions for a comet to produce CP if the particles forming its coma are symmetrical, optically inactive and randomly oriented:

- The part of the comet we are observing must be rotationally asymmetrical around the direction of the incident light.

- There must be some multiple scattering.

10.3 Description of the model

Let us represent a comet by a spherical cloud of dust with a spherical solid shell of radius R_N in its center (see Fig. 10.1). The cloud extends to the infinity but its particle number density distribution varies as $\frac{1}{r^2}$ with the distance r to the center of the system. Suppose that the relative abundances of particles of each size is the same at all volume elements dV. This is called the hypothesis of *homogeneous coma*, but it does not mean that the coma is homogeneous, because the number density of particles may be different at each part. The cloud is illuminated from a far distance by a plane-parallel source much wider than the solid nucleus. Photons of natural light are launched from the source, their paths are tracked and when they escape to the infinity, their Stokes parameters are transformed into spherical coordinates and finally recorded along with the direction (θ, φ) of escape (see Fig. 10.1). In this way, a complete map of the Stokes parameters can be obtained by adding the Stokes vectors of those photons escaping in a given direction.

The system of reference used along the present chapter is also defined in Fig. 10.1.

10.3.1 The particles of the coma

As we studied in Chaps. 6 to 9, there exist several mechanisms by which particles may produce some DCP on the scattered light under certain conditions. Since we did not want them to mix up with the multiple scattering by an asymmetrical comet, we assumed spherical optically inactive particles for the coma. We calculated the scattering matrices of the grains by using Bohren & Huffman's implementation of the Mie theory [3]. However, we must note that the versatility of the model allows us to use any type of particles. An average scattering matrix over a size distribution was calculated in all cases, and that is the matrix we used for every single scattering event. This represents a real case in conditions of single scattering (see Sec. 3.6), but if multiple scattering arises, it is just an approximation. The correct option would be to use a different scattering matrix for each sphere size, and use the size distribution to decide which one to use for each scattering event. However, this would make the code much slower, so we decided to use the approximation of average scattering matrix, even in conditions of multiple scattering.

It is important to remark that for non-spherical grains in the coma, the orientation average is also valid only for single scattering conditions. A scattering matrix of all particles at each orientation should be calculated, and one of them should be used at each scattering event for an exact representation

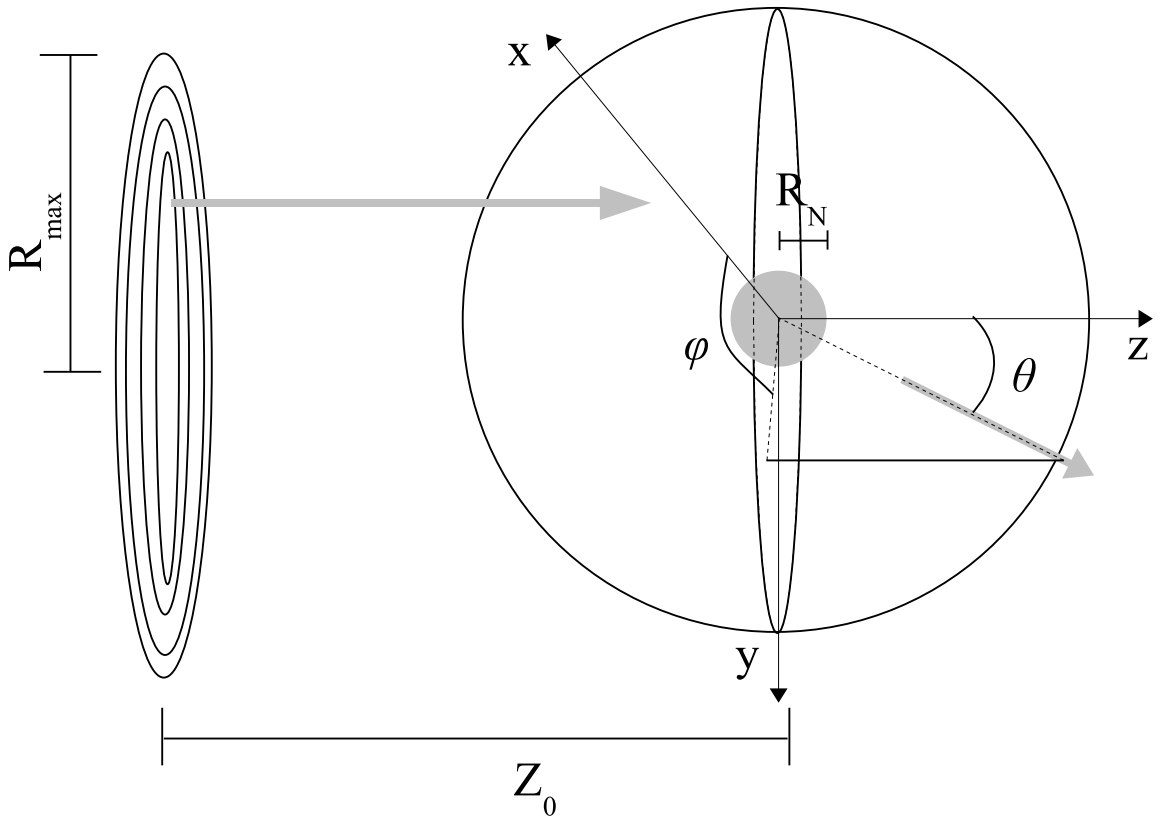

Figure 10.1: Spherical cloud of dust with a solid spherical core. The system is illuminated by a far plane-parallel source. Photons escape from the cloud in any direction (θ, φ). The coordinate axes used along the present chapter are set in the plot.

of a real comet.

10.3.2 Packets of photons

As we already stated in Sec. 3.4, natural light is used as incident light in our model. The reason is that light coming from the Sun is quite close to be totally unpolarized [12].

According to the *photoelectric effect* theory [18], when a photon interacts with a grain of dust, it can be completely reflected or completely absorbed by the grain, but never partially absorbed and reflected. This means that if we launch single photons, we will not obtain any outgoing light for some of them (those that are absorbed). For having better statistics in the results,

it would be desirable to get several outgoing light recorded events for each launch. There is a way to do this: launching *packets of photons*. Packets are collections of photons travelling together. We call the *weight of the packet* W to the proportion of the initial quantity of photons that still remains in the packet after a number of interaction events. Obviously, the initial weight of any packet is $W = 1$. We do not have to decide whether a packet is absorbed or reflected by a particle: a part of it is absorbed and the rest is reflected according to the single scattering albedo. In the same way, a part of the packet interacts with grains, while the rest goes to the infinity or to the nucleus, according to the probability of interaction with particles (given by the optical depth of the path ahead of the packet). The weight of a packet of photons is reduced each time that a part of it goes to the infinity or to the nucleus, and after each scattering event (see Sec. 10.3.4 for a detailed explanation). We track the evolution of packets until they vanish. We will consider that a packet is extinguished when its weight becomes lower than a certain limit W_{min}.

The Sun is so far from comets that the wave front reaching a comet is plane, and photons do not interact with the grains of the coma until they are very close to the comet. To reproduce these facts, we set a plane source of packets of photons at a distance Z_0 from the center of the comet (see Fig. 10.1). To ensure that the source is far enough, we checked that the results of the model are the same by using a distance Z_0 as by considering $2Z_0$. We set the launching platform circular with radius R_{max} ($R_{max} \gg R_N$). To ensure we chose a correct value of R_{max} we performed the same test as for Z_0. To make the flux uniform, as in the Sun, we did the following: Let us call ρ the distance from the launching point to the center of the launching platform (see Fig. 10.2), and P_L the probability of a packet of photons to be launched from a point within $[\rho, \rho + d\rho]$. If we denote by p_L the corresponding probability density function, $P_L(\rho) = p_L(\rho)d\rho$. If we divide the launching disk into small rings, the uniform-flux condition means that the probability of a packet to be launched from a specific ring must be proportional to the surface of that ring. Assuming infinitesimal rings, this leads to $P_L(\rho) \propto \rho d\rho$, since the surface of an infinitesimal ring is $dS = 2\pi\rho d\rho$. As a consequence $p_L(\rho) \propto \rho$. We can obtain the constant that we need to make this an identity by applying the normalization condition $\int_0^{R_{max}} p_L(\rho)d\rho = 1$. The result is:

$$p_L(\rho) = \frac{2\rho}{R_{max}^2}. \tag{10.1}$$

The probability density given by Eq. 10.1, along with the probability distribution sampling method described in Appendix A, easily lead us to a formula

for sampling values of the initial ρ coordinate of the launched packets:

$$\rho = \sqrt{\xi} R_{max}, \tag{10.2}$$

where ξ is a random number uniformly distributed within $[0, 1]$.

In order to improve the statistical stability of the model, we divided the launching disk into $NRING$ rings of equal surface (see Fig. 10.2), and we launched one packet of photons from each ring, starting from the central ring (actually a circle) and moving to the border sequentially. In this way it is assured that packets are launched from all regions of the launching platform. As rings have a certain width, the exact value of ρ for a packet to be launched

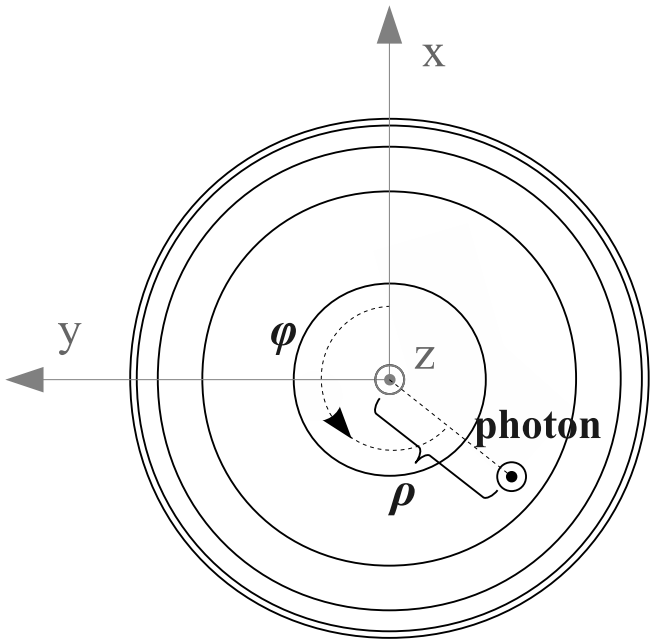

Figure 10.2: The launching disk is divided into a number of rings of equal area (as many as launched packets). Then, one packet is launched from each ring. For the inner rings, each packet is split into a number of sub-packets, and each of them is launched from a different point $[\rho, \varphi]$ into the ring. The exact coordinate ρ that a sub-packet is launched from, is calculated in such a way that the number of photons launched per unit area remains constant. Coordinate φ is uniformly randomly distributed in $[0, 2\pi]$.

from a certain ring $[\rho_1, \rho_2]$ is obtained through the distribution given by Eq.

10.1 and the method described in Appendix A as follows:

$$\rho = \rho_1 + \sqrt{\xi(\rho_2^2 - \rho_1^2)}. \tag{10.3}$$

The angle φ (see Figs. 10.2 and 10.1) can be obtained as a uniformly distributed random number within $[0, 2\pi]$.

A last issue to consider regarding the sampling of the launching coordinates is that it is important to resolve the central zone of the launching disk better than the outer part, in order to correctly account for the interaction of light with the nucleus. If the central ring covers a zone wider than the nucleus, then only one packet will be launched directly to it, and just a few of them will be deviated into it from a nearby region. Hence, there will not be good statistics for the incoming light on the nucleus, which is important because the interaction of light with the nucleus affects the outgoing radiation. The solution we adopted was to divide the launching platform into 3 zones: a)$\rho \leq R_N$, b)$R_N < \rho \leq 10R_N$, and c)$10R_N < \rho \leq R_{max}$, with $ndiv_1 > ndiv_2 > ndiv_3$. In zone a), $ndiv_1$ sub-packets of weigh $W = \frac{1}{ndiv_1}$ are launched instead of one only packet of $W = 1$. In region b) the division of the packet is by $ndiv_2$ and in region c) by $ndiv_3$. When several sub-packets are launched from the same ring, a different ρ and a different φ are sampled for each of them.

10.3.3 Interaction of a packet of photons with the grains

Let Φ be the flux of the incoming light, and let us call $\overline{\sigma}$ the average scattering cross-section of all particles in a certain volume element dV. Then, by the definition of the scattering cross-section (see Sec. 3.1), the decrease of the flux for light traveling a distance ds through dV is given by:

$$d\Phi = -\Phi n \overline{\sigma} dl, \tag{10.4}$$

where n is the particles number density in dV. By integrating, we obtain the *exponential decay law*:

$$\Phi = \Phi_0 e^{-\tau}, \tag{10.5}$$

where $\tau = \int_0^s n\overline{\sigma} ds'$ is called the *optical depth*. It is a dimensionless magnitude. Suppose that n is the same at all points of the cloud (which is not the case along the present study). Then, the *mean free path* of photons, which is defined as $\int_0^\infty n\overline{\sigma} e^{-\tau} s ds$, would be $\frac{1}{n\overline{\sigma}}$, and $\tau = n\overline{\sigma}s$. Therefore, in the case of n to be constant, the optical depth can be understood as the distance measured in units of the mean free path, i.e., it gives an idea of whether a photon is going to interact with particles when crossing a cloud or not.

This is why it is usually interpreted that a cloud of particles with $\tau > 1$ is opaque, and it is translucent if $\tau < 1$. We will call *optical thickness* to the *optical depth* of the whole object, like a comet or a gas cloud. As the relation between the optical depth and the distance is not linear, the optical depth may be finite for an infinite distance (for example, if $\overline{\sigma}$ is constant and the number density changes as $\frac{1}{s^2}$ along the path to the infinity).

The probability density of interaction of the packet of photons with a grain is:

$$p(s) = \frac{d(1 - \frac{\Phi}{\Phi_0})}{ds} = n\sigma e^{-\tau}, \tag{10.6}$$

which means that the proportion of photons that interact with particles within $[s, s + ds]$ is $p(s)ds \propto n\overline{\sigma}e^{-\tau}ds$. Equivalently, the proportion of photons that interact with particles within $[\tau, \tau + d\tau]$ is $p(\tau) \propto e^{-\tau}d\tau$. Let us call τ_{max} the maximum optical depth that a photon may travel (optical depth to the infinity or to any obstacle). The normalization constant a_1 of $p(\tau)$ can be obtained from the normalization condition:

$$\int_0^{\tau_{max}} a_1 e^{-\tau} d\tau = 1 \Leftrightarrow a_1 = \frac{1}{1 - e^{-\tau_{max}}} \Rightarrow p(\tau) = \frac{e^{-\tau}}{1 - e^{-\tau_{max}}}. \tag{10.7}$$

Once the probability density function has been derived, we can apply the general sampling method by using uniform random numbers (see Appendix A):

$$\xi = \int_0^{\tau} \frac{e^{-\tau'}}{1 - e^{-\tau_{max}}} d\tau' \Leftrightarrow \tau = -\ln[1 - \xi(1 - e^{-\tau_{max}})]. \tag{10.8}$$

Let us now calculate the formula to translate physical distance to optical depth and vice versa. As we made the homogeneous coma hypothesis (Sec. 10.3), $\overline{\sigma}$ is constant in the cloud, so we can write:

$$\tau = \int_0^s \overline{\sigma} n(s') ds' = \overline{\sigma} \int_0^s n(s') ds'. \tag{10.9}$$

To proceed, we need to assume some particular number distribution of grains in the coma. For simplicity, we chose $n(r) = a_2 \frac{1}{r^2}$, with $a_2 = constant$. Let us call τ_N the optical depth of the whole cloud from the surface of the nucleus to the infinity in the radial direction. Then:

$$\tau_N = \int_{R_N}^{\infty} \overline{\sigma} n(r) dr = a_2 \overline{\sigma} \int_{R_N}^{\infty} \frac{dr}{r^2} \Rightarrow a_2 = \frac{\tau_N R_N}{\overline{\sigma}}. \tag{10.10}$$

By substituting a_2 in Eq. 10.9 we obtain:

$$\tau = \tau_N R_N \int_0^s \frac{1}{r^{-2}} ds'. \tag{10.11}$$

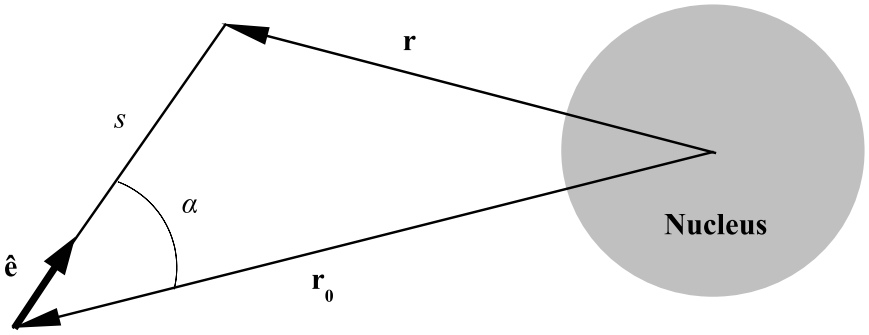

Figure 10.3: Initial ($\mathbf{r_0}$) and final ($\mathbf{r}$) positions of a packet of photons. The distance travelled in the direction of propagation $\hat{\mathbf{e}}$ is denoted by s. A non-right triangle is formed by edges r, r_0 and s, that can be solved by the *law of cosines*.

The radial distance r is different from the distance s if the path of the packet of photon is in a non-radial direction. In Fig. 10.3 it is clear that the problem can be easily solved by the well-known law of cosines as follows:

$$r^2 = s^2 + r_0^2 - 2sr_0\cos\alpha. \tag{10.12}$$

As $\mathbf{r_0}\cdot\hat{\mathbf{e}} = -r_0\cos\alpha$,

$$r^2 = s^2 + r_0^2 + 2s\mathbf{r_0}\cdot\hat{\mathbf{e}}. \tag{10.13}$$

Combining Eqs. 10.13 and 10.11 leads to:

$$\tau = \tau_N R_N \int_0^s (r_0^2 + 2s'\mathbf{r_0}\cdot\hat{\mathbf{e}} + s'^2)ds'. \tag{10.14}$$

By solving the integral in Eq. 10.14, we get:

$$\tau = \frac{\tau_N R_N}{\Delta}\left(\arctan\frac{\mathbf{r_0}\cdot\hat{\mathbf{e}}+s}{\Delta} - \arctan\frac{\mathbf{r_0}\cdot\hat{\mathbf{e}}}{\Delta}\right), \tag{10.15}$$

if $\Delta = \sqrt{r_0^2 - (\mathbf{r_0}\cdot\hat{\mathbf{e}})^2} \neq 0$.

In the particular case that $s \to \infty$, we just calculate the limit in Eq. 10.15:

$$\tau_\infty = \frac{\tau_N R_N}{\Delta}\left(\frac{\pi}{2} - \arctan\frac{\mathbf{r_0}\cdot\hat{\mathbf{e}}}{\Delta}\right). \tag{10.16}$$

We can obtain s as a function of τ just by working its value out in Eq. 10.15 :

$$s = \Delta\tan\frac{\Delta\tau}{\tau_N R_N} + \arctan\frac{\mathbf{r_0}\cdot\hat{\mathbf{e}}}{\Delta} - \mathbf{r_0}\cdot\hat{\mathbf{e}}. \tag{10.17}$$

In the case that $\Delta \approx 0$, we may have some numerical problems in applying Eqs. 10.15 to 10.17. Having $\Delta \approx 0$ means that $r_0 \approx \mathbf{r_0} \cdot \hat{\mathbf{e}}$, i.e., $\mathbf{r_0}$ is almost parallel (or anti-parallel) to $\hat{\mathbf{e}}$. This happens to packets of photons launched from the central region of the launching platform, before they interact with any grain. The solution to this numerical issue is to build the equations for the special case $\Delta = 0$, and use them when the actual Δ is below a certain minimum value Δ_{min}. Let us go back to Eq. 10.14. There exist two possibilities for $\Delta = 0$:

- $\mathbf{r_0} \parallel \hat{\mathbf{e}}$ in the opposite sense ($\mathbf{r_0} \cdot \hat{\mathbf{e}} = -r_0$): packets of photons coming into the nucleus in radial direction.
- $\mathbf{r_0} \parallel \hat{\mathbf{e}}$ in the same sense ($\mathbf{r_0} \cdot \hat{\mathbf{e}} = r_0$): packets of photons travelling far away from the nucleus in radial direction.

For packets of photons approaching the nucleus:

$$\tau = -\tau_N R_N \frac{s}{r_0(s - r_0)}, \tag{10.18}$$

and for those moving far away from the nucleus:

$$\tau = \tau_N R_N \frac{s}{r_0(s + r_0)}. \tag{10.19}$$

For the particular case that the packet goes to the infinity, we just calculate the limit $s \to \infty$ in Eq. 10.19:

$$\tau_\infty = \frac{\tau_N R_N}{r_0}. \tag{10.20}$$

Now we work s out from Eqs. 10.18 and 10.19. For packets of photons approaching the nucleus:

$$s = \frac{\tau r_0^2}{\tau_N R_N + \tau r_0}, \tag{10.21}$$

and for those travelling far away from the nucleus:

$$s = \frac{\tau r_0^2}{\tau_N R_N - \tau r_0}. \tag{10.22}$$

For obtaining the optical depth to the nucleus τ_c, we just have to apply Eq. 10.15 if $\Delta > \Delta_{min}$ or Eq. 10.18 if $\Delta \leq \Delta_{min}$, but in all cases we need the distance to the nucleus s_c. Let us call now $\mathbf{r_0}$ the position vector of a packet of photons that points in the direction (and sense) of the unit vector $\hat{\mathbf{e}}$. Fig. 10.4 shows a triangle where 2 edges and one angle are known. Therefore, the

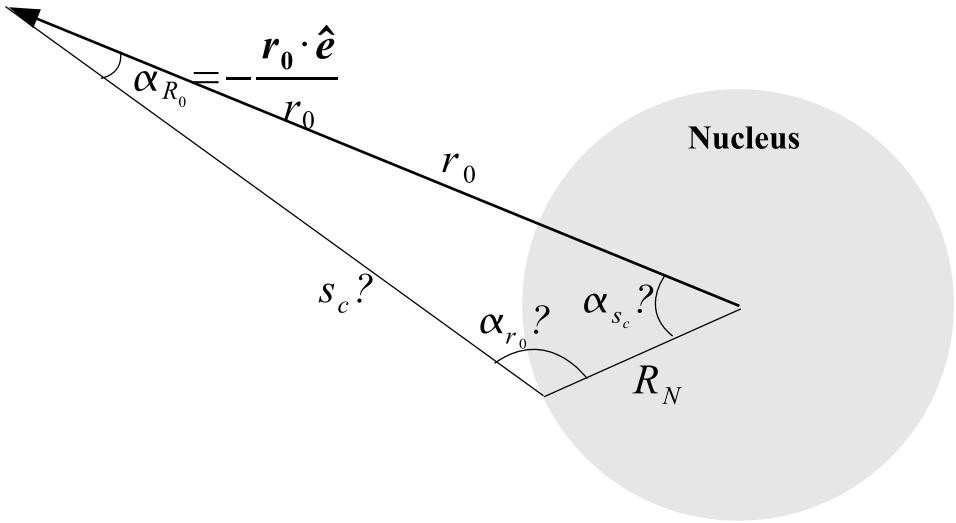

Figure 10.4: A non-right triangle with two known edges and one known angle. The triangle can be completely solved by using the law of sines and the law of cosines. Vector $\mathbf{r_0}$ is the position of a packet of photons that is pointing to the nucleus, and $\hat{\mathbf{e}}$ is a unit vector in the direction (and sense) of propagation of the packet. We are interested in obtaining the distance s_c from the position of a packet of photons to the surface of the nucleus.

triangle can be completely solved. By applying the well known *law of sines* with the edges R_N and r_0, we obtain:

$$\frac{R_N}{\sin \alpha_{R_N}} = \frac{r_0}{\sin \alpha_{r_0}} \Rightarrow \alpha_{r_0} = \pi - \arcsin\left(\frac{r_0}{R_N} \sin \alpha_{R_N}\right). \tag{10.23}$$

On the other hand, $\alpha_{s_c} = \pi - \alpha_{R_N} - \alpha_{r_0}$. Substituting Eq. 10.23 here leads to:

$$\alpha_{s_c} = -\arccos \frac{-\mathbf{r_0} \cdot \hat{\mathbf{e}}}{r_0} + \arcsin\left(\frac{r_0}{R_N} \sin \alpha_{R_N}\right) \tag{10.24}$$

Applying the law of sines to edges R_N and s_c gives:

$$\frac{R_N}{\sin \alpha_{R_N}} = \frac{s_c}{\sin \alpha_{s_c}}, \tag{10.25}$$

and by substituting Eq. 10.24 we get:

$$s_c = R_N \frac{\sin \alpha_{s_c}}{\sin \alpha_{R_N}}. \tag{10.26}$$

In the particular case of $\alpha_{R_N} = 0$:

$$s_c = r - R_N. \tag{10.27}$$

All equations derived in this section, are the base to track the paths of the packets of photons. We present a detailed explanation about that in the following section.

10.3.4 Paths of packets of photons

Imagine a packet of photons of weight W travelling in a certain direction $\hat{\mathbf{e}}$. There exist two possibilities:

- *Packets pointing to the nucleus*: Saying that a packet of photons points to the nucleus is equivalent to say that there exists an intersection between the straight line defined by the direction of propagation of the packet $\hat{\mathbf{e}} = (e_x, e_y, e_z)$ and the nucleus (a sphere of radius R_N centered at $(0, 0, 0)$). Suppose that the actual position of the packet is $\mathbf{r_0} = (x_0, y_0, z_0)$, and let s_c be the distance to the nucleus. Then, the intersection point (x_c, y_c, z_c) with the sphere will be given by:

$$\left.\begin{aligned} x_c &= x_0 + s_c e_x \\ y_c &= y_0 + s_c e_y \\ z_c &= z_0 + s_c e_z \\ x_c^2 + y_c^2 + z_c^2 &= R_N^2. \end{aligned}\right\} \tag{10.28}$$

  From Eq. 10.28 we derive:

$$(x_0^2 + y_0^2 + z_0^2) + 2 s_c \mathbf{r_0} \cdot \hat{\mathbf{e}} + s_c^2 = 0 \tag{10.29}$$

  Eq. 10.29 has a solution only if:

$$(\mathbf{r} \cdot \hat{\mathbf{e}}) \geq x_0^2 + y_0^2 + z_0^2 - R_N^2 \tag{10.30}$$

  Eq. 10.30 gives a necessary and sufficient condition for a packet to point to the nucleus.

  Once that we know that a packet points to the core of the comet, we do not have to decide whether it reaches the nucleus or it interacts with a grain of the coma. Instead, we split the packet into two parts: one going to the core and another remaining in the coma and forced to interact with a grain. According to the exponential decay law (Eq. 10.5), if the optical depth to the core is τ_c, the part of the packet of photons that reaches the nucleus is $We^{-\tau_c}$, so the part that remains in the coma for interaction with grains is $W(1 - e^{-\tau_c})$.

- *Packets pointing to the infinity*: Packets will point to the infinity when not pointing to the nucleus. According to Eq. 10.5 the part of the packet going to the infinity is $We^{-\tau_\infty}$, and a weight $W(1-e^{-\tau_\infty})$ remains in the coma for interacting with the particles.

When a packet of photons interacts with a grain, a part of it is absorbed and the rest is scattered. We do not care about the absorbed part because we are not interested in the infrared re-radiated light. If the initial weight of the packet is W, the weight of the scattered packet will be $\tilde{\omega}W$, where $\tilde{\omega}$ is the single scattering albedo of the particles of the coma (see Sec. 3.1). After each scattering event of a packet of photons we check whether the new weight of the packet is below the lower limit we set for extinction. If $W < W_{min}$ a new packet is launched.

Fig. 10.5 shows some examples of paths of packets of photons along with the weights of the packets at each stage.

The process of scattering of the packet of photons involves a number of calculations that must be described: the updating of the position, the choice of the scattering direction, the change from the old scattering plane to the new one, and the final change from the last plane of scattering to the meridian plane.

Updating of the position of the packet of photons: Consider that a packet of photons is located in a position $\mathbf{r_0}$ while travelling in a direction $\hat{\mathbf{e}}$. After subtracting the part that goes to the infinity to the nucleus, another part remains in the coma that is forced to interact with a grain. First of all, we sample by Eq. 10.8 the optical depth that the packet will travel from its present position to the point it will interact with a particle. Then, the optical depth is converted into distance by the corresponding Eq. (10.17, or 10.21 or 10.22), and the position is updated as $\mathbf{r} = \mathbf{r_0} + s\hat{\mathbf{e}}$.

Choice of the scattering direction: To make a reasonable choice of the scattering direction, we need a probability density distribution. Consider I the first Stokes parameter of the light scattered by a grain. As it is proportional to the flux (see Sec. 3.2.3), IdS is proportional to the energy that crosses an elemental surface dS per unit time. Let us assume now that the particles of the coma are randomly oriented. Then, the scattering matrix does not depend on φ, so I does not depend on it either. The elemental surface dS for a spherically symmetrical scenario is plotted in Fig. 10.6, and it is clear from the plot that $dS = 2\pi R^2 \sin\theta d\theta$. Therefore, $I(\theta)\sin\theta d\theta$ is proportional to the energy scattered at each direction θ per unit time. Since this is proportional to the probability of scattering at θ, the probability den-

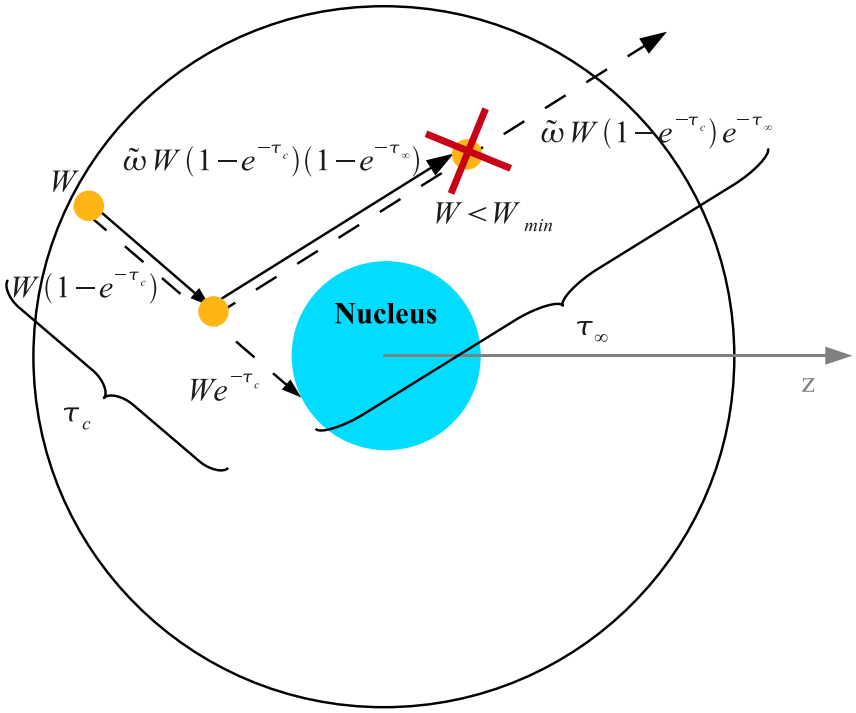

Figure 10.5: Evolution of the weight of a packet of photons. The packet reduces its weight by a factor of $(1-e^{\tau_c})$ or $(1-e^{\tau_\infty})$, depending on whether it points to the nucleus or to the infinity. The rest remains in the coma, and when it interacts with a grain, the scattered part is reduced by a factor $\tilde{\omega}$ (the single scattering albedo).

sity function of the scattering direction can be written as $p(\theta) \propto I(\theta) \sin\theta$. Just by applying Eq. 3.61 we obtain:

$$p(\theta) \propto [F_{11} I_0 + F_{12} Q_0 + F_{13} U_0 + F_{14} V_0] \sin\theta, \tag{10.31}$$

where (I_0, Q_0, U_0, V_0) is the Stokes vector of the incident light. The function given in Eq. 10.31 must be normalized to 1 each time we use it, because the Stokes parameters of the incident light are different at each event.

Change from the old scattering plane to the new one: For the first scattering event of a packet of photons, the incident light is natural, so the Stokes parameters are independent of the reference plane. But once the first scattering event occurs, the resulting Stokes parameters are written with regard to the scattering plane. The scattering plane of the second scattering event will

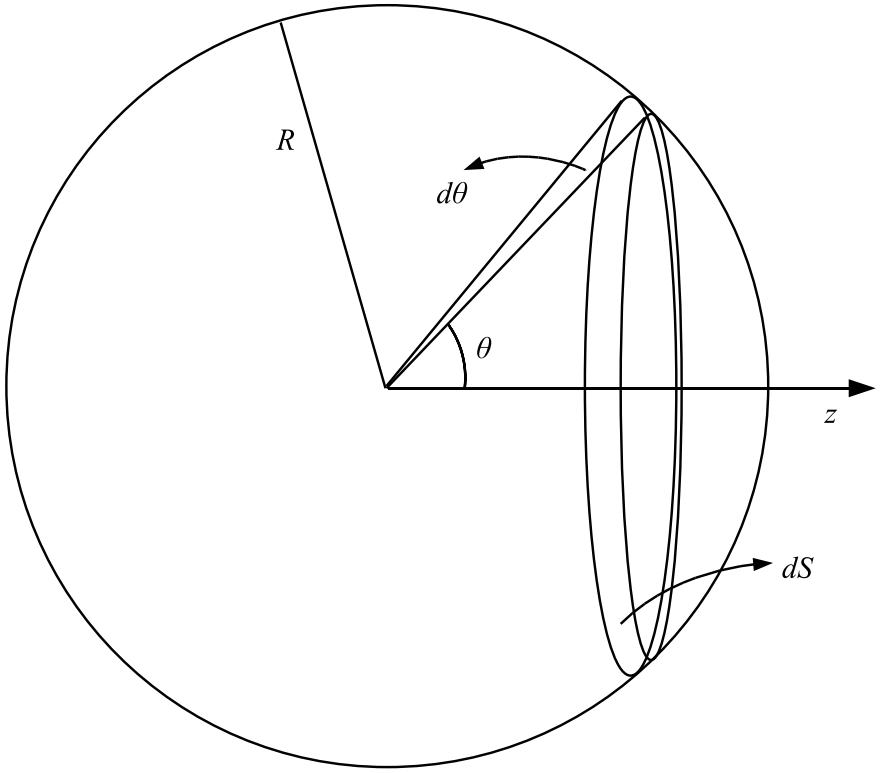

Figure 10.6: Elemental surface dS for a spherically symmetrical system. It can be written as $dS = 2\pi R^2 \sin\theta d\theta$.

be different, so the Stokes parameters of the incident light should be transformed into the new reference plane before applying the scattering matrix. The same applies for higher orders of scattering.

The scattered light of a scattering event becomes the incident light of the following. Hence, that beam of light (let us call it *intermediate beam*) is contained in both the last and the new scattering plane. As a consequence, the change of the scattering plane always consists of a rotation around the direction of the intermediate beam. This statement is illustrated in Fig. 10.7, where the intermediate beam is $\hat{\mathbf{u}}_\mathbf{2}$. To perform the change of reference plane we first calculate the rotation angle i_{rot} anticlockwise when looking in the direction (and sense) of propagation of light (see Fig. 10.7), and apply the transformation given in Eq. 3.59 to the Stokes parameters.

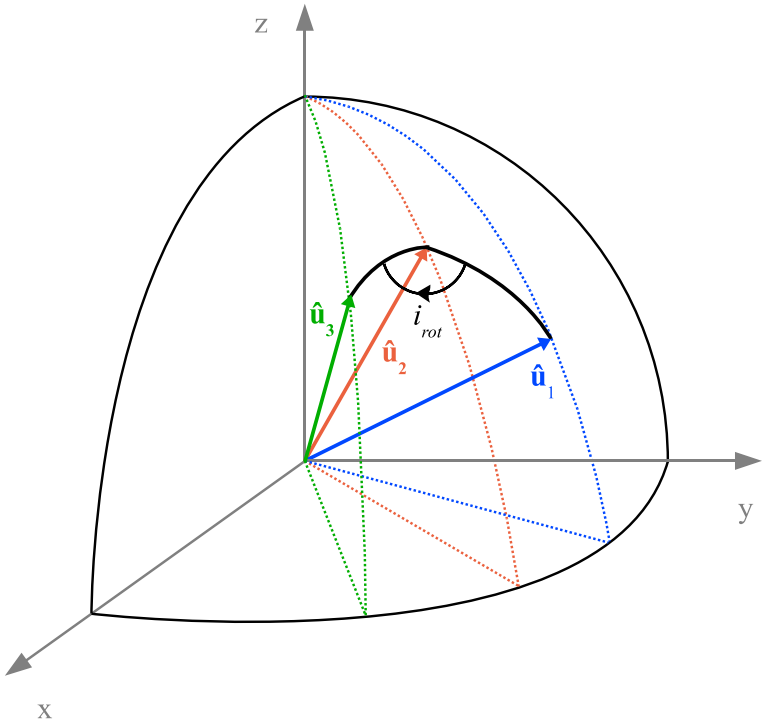

Figure 10.7: Diagram containing the directions of propagation of light and the scattering planes of a packet of photons that undergoes two scattering events. Light initially travelling in the direction (and sense) of $\hat{\mathbf{u}}_1$ is scattered and then it points in the direction (and sense) of $\hat{\mathbf{u}}_2$. After the second scattering event, $\hat{\mathbf{u}} = \hat{\mathbf{u}}_3$. The angle i_{rot} rotates the first scattering plane to make it coincident with the second anticlockwise when looking in the direction (and sense) of propagation of light. That is the angle to use in Eq. 3.59 to transform the Stokes parameters from the old to the new scattering plane.

Change from the last plane of scattering to the meridian plane: In order to record the Stokes parameters of light outgoing the comet, we performed two operations:

- We divided the whole sphere into small angular regions of $\Delta\theta \times \Delta\varphi$, around directions (θ, φ). Then, we considered that all parts of packets of photons escaping in a direction contained in one of those bins, are actually travelling in the same direction. The intervals $\Delta\theta$ and $\Delta\varphi$ should be small enough to fulfill the latter hypothesis, but large enough

to obtain a statistically significant signal in each region.

- We changed the plane of reference from the last scattering plane to the meridian plane at (θ, ϕ). To perform this operation we first calculated the angle i_{rot} (see Fig. 10.8). This is the angle that rotates the last scattering plane through the direction of light, to make it coincide with the meridian plane. It is considered positive when the rotation is anti-clockwise if looking in the direction (and sense) of propagation of light. With i_{rot}, we can apply to the Stokes parameters the transformation given in Eq. 3.59.

Once we divided the range of directions into bins, and changed the plane of reference to the meridian plane at each bin, the Stokes parameters of all packets of photons considered to escape in the same direction were written in the same system of reference. Hence, they could be added. After launching a sufficient number of packets of photons $NPHOT$ to achieve statistical stability, we obtained four maps corresponding to the four Stokes parameters as functions of θ and ϕ, plotted with bins of $\Delta\theta \times \Delta\varphi$. Just by applying definitions in Eqs. 3.55 and 3.56, we obtained maps of the flux, $EDLP$ and the DCP as functions of θ and ϕ.

Note: In all papers and books about radiative transfer we have studied, authors always make any change of a reference plane into other with a middle change to a meridian plane (see e.g., [6, 28, 53]). The change to the meridian plane only makes sense at the last stage of the path of light: when it escapes from the coma and is going to be recorded. We avoided to make these unnecessary rotations of the reference plane in order to make our code computationally efficient.

10.3.5 Light reflection on the nucleus

The exact reproduction of the reflections of light on the comet nucleus surface presents two problems:

- There not exist good approximations to simulate scattering by rough surfaces. As far as we know, the most complete tool is the model developed by Mishchenko and Travis in 1997 [49]. Even though, it is just valid for surfaces with smooth slopes. This model is meant to study the reflection of light on the surface of the ocean, and it is no valid for rough surfaces.

- We do not have conclusive data about the properties of the typical surfaces of the nuclei of comets.

Moreover, we used a high value of the optical thickness τ_N of the comet to ensure multiple scattering, since we deduced in Sec. 10.2 that this is a necessary condition for CP to be produced by a comet coma with only spherical optically inactive grains of dust.

The simplest model of reflection on a surface is the *lambertian reflection* model. Packets of photons are reflected in a random direction by such surface, and get totally unpolarized. We performed some tests and concluded that for $\tau_N = 2.5$, it does not make any difference to consider the reflections on the nucleus. This is due to the fact that just a few photons reach the surface

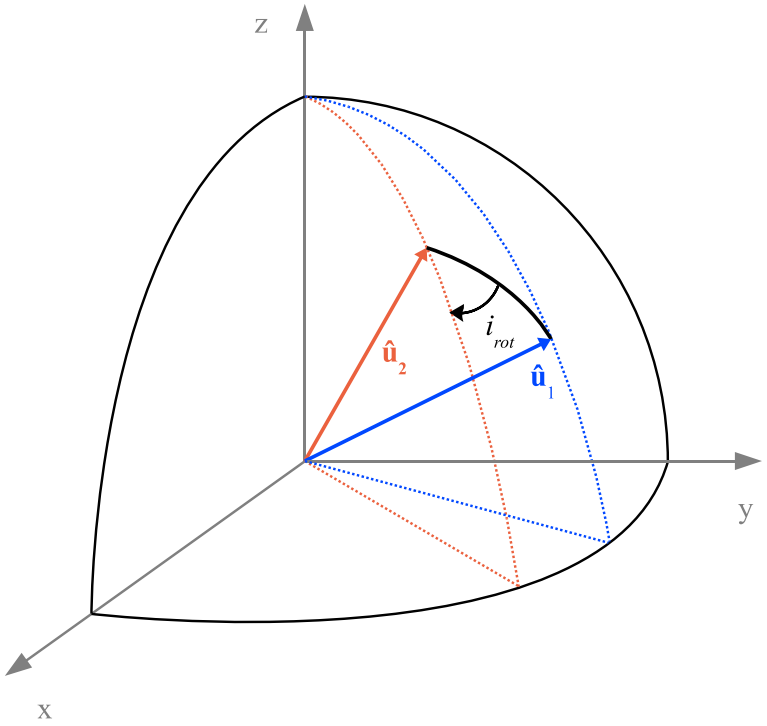

Figure 10.8: Change from the last scattering plane of a packet of photons to the meridian plane. Light travelling in the direction (and sense) of $\hat{\mathbf{u}}_\mathbf{1}$ is scattered and then it propagates with $\hat{\mathbf{u}} = \hat{\mathbf{u}}_\mathbf{2}$. We need to rotate the scattering plane by an angle i_{rot} anticlockwise (when seen in the direction and sense of propagation of light) to make it coincident with the meridian plane. This change of the plane of reference permits us to write in the same reference system the Stokes parameters of all the fractions of packets of photons scattered in the same direction. In this way, their Stokes parameters can be added.

of the nucleus and just a small fraction of the reflected photons escape from the coma. In addition, the typical surface albedo of comets is about 4%, as we stated in Sec. 2.1.

Based on all arguments posed above, we decided to consider a totally absorbent surface of the nucleus for the present study.

10.3.6 Common input parameters

Along the following sections, several calculations with the described radiative transfer model are presented. Different input parameters were used for each of them, but some of the inputs are common to all runs of the program. We present these common input parameters in Table 10.1.

R_N	5 km
Kind of particles	spheres
Size distribution type	power-law, exponent=-3.5
r_{min}	0.05 μm
m	$1.6 + i0.001$
$ndiv_1$	100
$ndiv_2$	10
$ndiv_3$	1
Wavelength	0.5 μm
W_{min}	10^{-8}
Δ_{min}	10^{-10} m

Table 10.1: Input parameters of the radiative transfer model used for calculations presented in Secs. 10.4 to 10.7.

The specific parameters for each calculation are specified in the corresponding section.

10.4 Checking the model

We performed several tests to check that the present model is correct and that the code implementing the model is working correctly. All of them deal with a perfectly symmetrical comet around the direction of the incident light.

Tables 10.1 and 10.2 contain the input parameters of the model used in the following tests:

1. Based on the condition given in Sec. 5.2, the DCP must be exactly zero for all scattering angles in case of a perfectly symmetrical comet

$NPHOT$	10^8
$NRING$	10^8
r_{max}	20 μm
$\Delta\theta$	1°
$\Delta\varphi$	1°

Table 10.2: Specific input parameters of the model that we used to calculate the $EDLP$ and DCP of light scattered by an azimuthally symmetrical comet around the optical axis. These calculations were devoted to test the model and the code.

around the direction of the incident light, independently of the optical thickness of the coma. We made calculations for $\tau_N = 0.25$, 1 and 2.5, and we found the condition to be fulfilled for all cases.

2. As we are assuming that the comet is symmetrical around the direction of the incident light, results on the $EDLP$ must be independent of φ for a certain θ. We do not need single scattering conditions for the present test, but we set $\tau_N = 0.1$ so that the calculations become also valid for the next test. It is clear from Fig. 10.9 that the condition is fulfilled.

3. In conditions of single scattering, the calculated $EDLP$ must be equal to $\frac{-F_{12}}{F_{11}}$ (Eq. 3.81) at all scattering directions. To assure the single scattering conditions we set $\tau_N = 0.1$. As the results on the $EDLP$ are independent of φ (see test 2), we randomly chose a value of the azimuthal angle: $\varphi = 309^\circ$. In Fig. 10.10, the $EDLP$ calculated with the model is compared to the theoretical value derived from the scattering matrix. The match is almost perfect, so that the test was successful.

10.5 The effect of local observations

We can simulate the observation of a small region of the comet by imposing the condition that only light escaping from a certain region of the coma will be added to calculate the Stokes parameters in all directions. The region of observation is defined as a cone in a direction $(\theta_{loc}, \varphi_{loc})$ and an angular width β_{loc} (see Fig. 10.11).

If a fraction of a packet of photons is escaping from the coma, the condition it must fulfill to be considered, is to come from the cone defined by

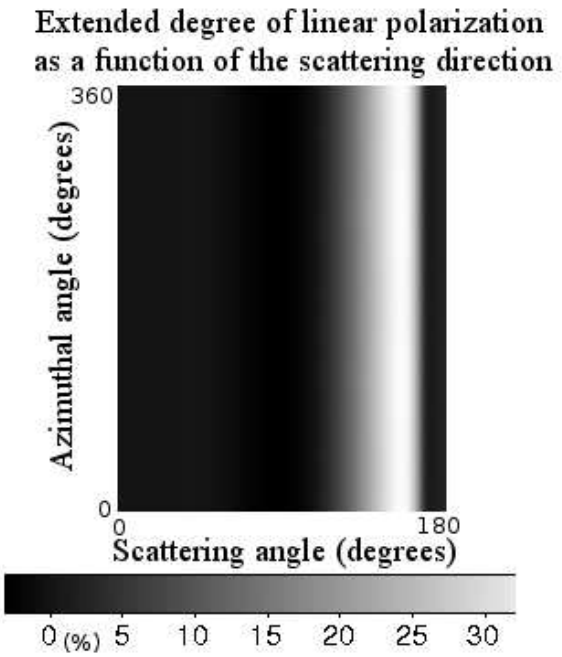

Figure 10.9: DLP as a function of θ and φ. The result is independent of φ, as corresponds to an azimuthally symmetrical comet around the direction of the incident light. The optical depth is set to $\tau_N = 0.1$.

$(\theta_{loc},\ \varphi_{loc})$ and β_{loc}. Let us call $\hat{\mathbf{r}}_{\mathbf{loc}}$ to a unit vector defined by coordinates θ_{loc} and φ_{loc}:

$$\hat{\mathbf{r}}_{\mathbf{loc}} = (\sin\theta_{loc}\cos\phi_{loc}, \sin\theta_{loc}\sin\phi_{loc}, \cos\theta_{loc}). \tag{10.32}$$

Let $\mathbf{r_0} = (x_0, y_0, z_0)$ be the position of the fraction of the packet of photons that escapes. The condition we have to impose is that $\hat{\mathbf{r}}_{\mathbf{loc}}$ and $\mathbf{r_0}$ form an angle smaller than β_{loc}. This can be written as:

$$\arccos \frac{x_0 \sin\theta_{loc}\cos\phi_{loc} + y_0 \sin\theta_{loc}\sin\phi_{loc} + z_0\cos\theta_{loc}}{x_0^2 + y_0^2 + z_0^2} \leq \beta_{loc} \tag{10.33}$$

The input parameters used for calculations of the DCP of light coming from a non-central region of the comet are listed in Tables 10.1 and 10.3. Note that the intervals $\Delta\theta$ and $\Delta\varphi$ are ten times wider than those chosen in the previous section. This is necessary to achieve good statistics in each bin $\Delta\theta \times \Delta\varphi$ because of two reasons:

- We are looking only at a small zone of the coma, so we are missing most of the light scattered in the comet. Thus, the same computational

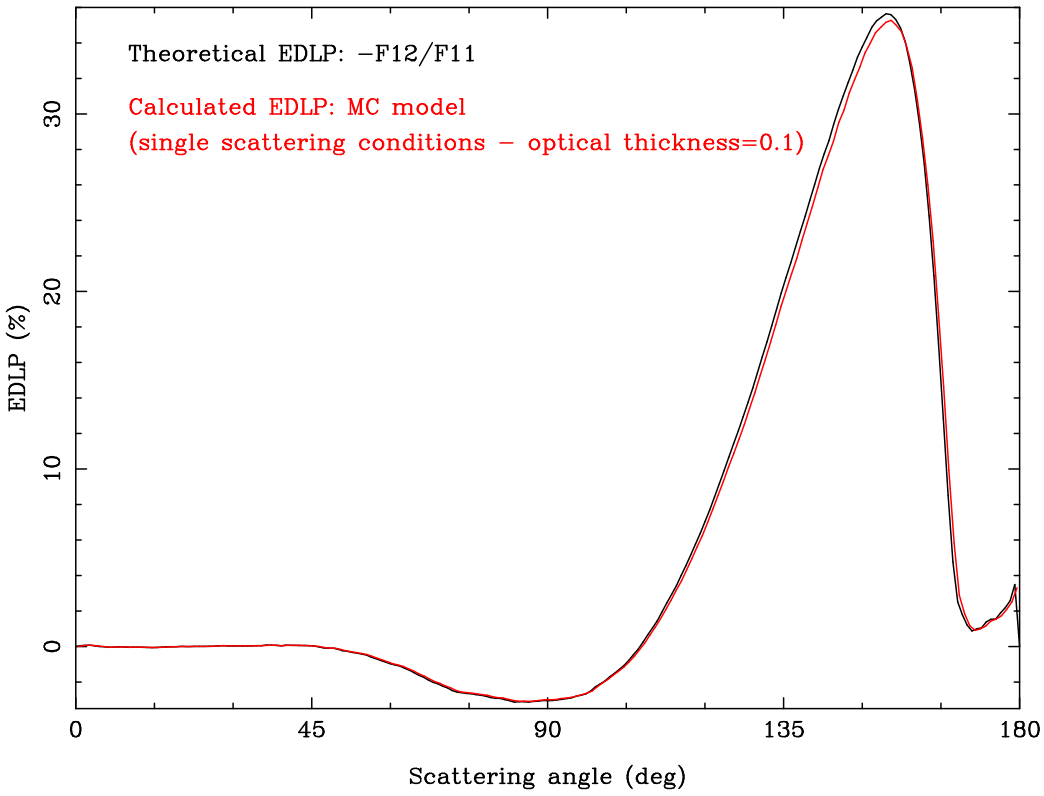

Figure 10.10: Comparison of the $EDLP$ calculated with the Monte Carlo model to the theoretical value in single scattering conditions, derived from the scattering matrix. The agreement is excellent.

$NPHOT$	10^8
$NRING$	10^8
τ_N	2.5
$\Delta\theta$	10°
$\Delta\varphi$	10°
θ_{loc}	60°
φ_{loc}	0°
β_{loc}	10°

Table 10.3: Specific input parameters used to calculate the DCP of light coming from a non-central local region of the comet (see Fig. 10.12).

effort to launch and track the evolution of the same number of packets of photons as in the previous section is being performed, but a much lower signal is being recorded at each bin.

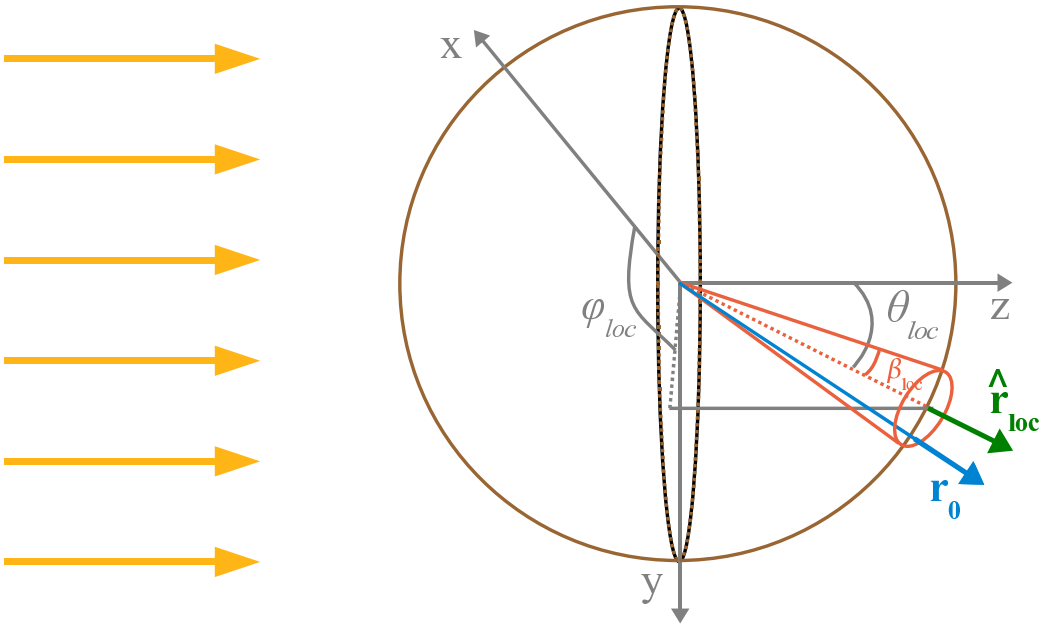

Figure 10.11: A small conical region of the comet (plotted in red) is defined by angular coordinates $(\theta_{loc}, \varphi_{loc})$ and an angle β_{loc}. A unit vector $\hat{\mathbf{r}}$ is defined by $(\theta_{loc}, \varphi_{loc})$. Light that escapes from the comet is considered only if the vector position $\mathbf{r_0}$ of the fractions of the packets of photons that escape is contained into the red cone.

- We are using a much larger optical thickness than in Sec. 10.4 (25 times larger), so much more absorption occurs in the coma, and the amount of outgoing radiation energy is much lower for the same number of launched packets of photons.

We checked the statistical stability by repeating the calculations with $NPHOT = 8 \cdot 10^8$, and verifying the convergence of the obtained results.

Fig. 10.12 presents the results of the calculations on the DCP (left panel) for $r_{max} = 20\ \mu m$, along with an illustration of the meaning of the plot (right panel).

The big light blue circle of the right panel of Fig. 10.12 represents the comet. It is illuminated from the back. Only light scattered from a 10° wide region was considered. That zone is marked in the figure by a small dark blue circle. From that region, light is scattered in all directions. We just present results for $-90° \leq \varphi \leq 90°$ because the best statistics was achieved for those angles.

We find three main features in the results presented in Fig. 10.12:

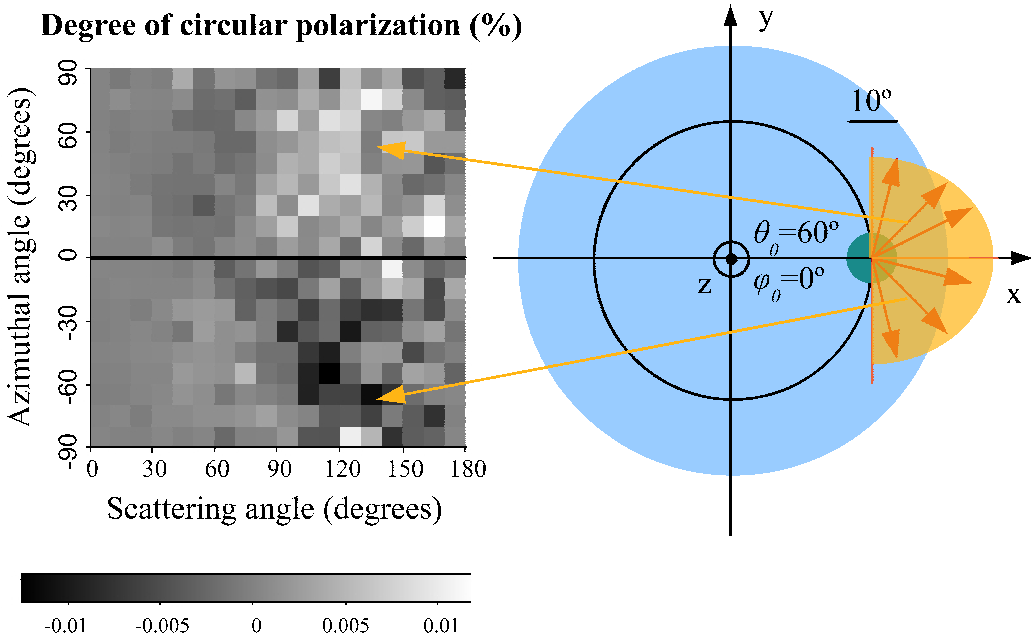

Figure 10.12: Results for the calculations of the DCP with our radiative transfer model (left panel). All parameters of the model are taken from Tables 10.1 and 10.3, except for r_{max}, that is set to 20 μm. An illustration of the meaning of the left plot is presented in the right panel. Only light coming from a small region (small dark blue circle) is recorded. Radiation is emitted in all directions from that zone. Only results for light scattered at φ within $[-90°, 90°]$ are presented, because the best statistics is achieved within this interval.

1. The upper part and the lower part of the left panel of Fig. 10.12 are color-complementary: the white bins of the upper part correspond to the black bins of the lower part.

2. For angles close to the backscattering, higher values of the DCP (in absolute value) are calculated than for forward-scattering angles.

3. The calculated values of the DCP are about one or two orders of magnitude below those of the observations.

Feature (1) can be understood in terms of symmetry: if a certain DCP appears by any means for positive values of the azimuthal angle, opposite values must be given when observing from a direction with $\varphi < 0$. The proof is again based in symmetry arguments, and it is identical to that given in Sec. 5.2.

Regarding feature (2), we think that this may be an argument to support the idea that multiple scattering is the responsible for the observed DCP, because light scattered in the back direction has generally undergone more scattering events that light passing by the comet with little interaction with the grains of the coma. If multiple scattering along with asymmetry of the observation scenario is the mechanism producing CP, it makes sense that the more important the multiple scattering becomes, the higher values of the DCP are reached.

About feature (3), we tried to achieve higher values of the DCP by making calculations for larger particles. Results presented in Fig. 10.12 correspond to particles with a maximum size of 20 μm. According to Sec. 2.4, much larger grains may be present in the coma of comets (up to the order of 1 mm). We performed calculations of the DCP for two samples with $r_{max} = 200$ μm and $r_{max} = 2$ mm. The rest of the parameters of the code were the same as for the result showed in Fig. 10.12.

The Mie scattering code implemented by Bohren & Huffman presents some convergence problems when particles become as large as 2 mm. In order to get accurate results, we used a large number of sizes to sample the size distribution (5000), and adjusted the accuracy parameters of the program. Both, the size distribution and the non-zero independent scattering matrix elements (see Sec. 3.6.2) are plotted in Figs. 10.13 and 10.14, respectively. All curves are smooth, and regarding the scattering matrix, conditions at exact forward- and backward-scattering are fulfilled (see, e.g., [30]). These arguments lead us to rely on the calculated size-averaged scattering matrix.

Fig. 10.15 shows the calculated DCP for the samples with $r_{max} = 200$ μm (left panel), and for the sample of $r_{max} = 2$ mm (right panel).

The calculated values are of the same order of those obtained for $r_{max} = 20$ μm (Fig. 10.12). Hence, the local observation of a symmetrical comet whose coma is formed by spherical grains, cannot explain the observed DCP in comets.

10.6 Asymmetry of the coma

The distribution of dust particles around the nucleus of a comet might be inhomogeneous. For instance, there might be active regions of the surface of the nucleus in some specific parts, or there might be more sublimation in the side of the comet that faces the Sun. This asymmetrical distribution could lead to the asymmetry of the coma around the optical axis, so some DCP could arise from this mechanism.

We divided the coma of the comet into two halves, the separation plane

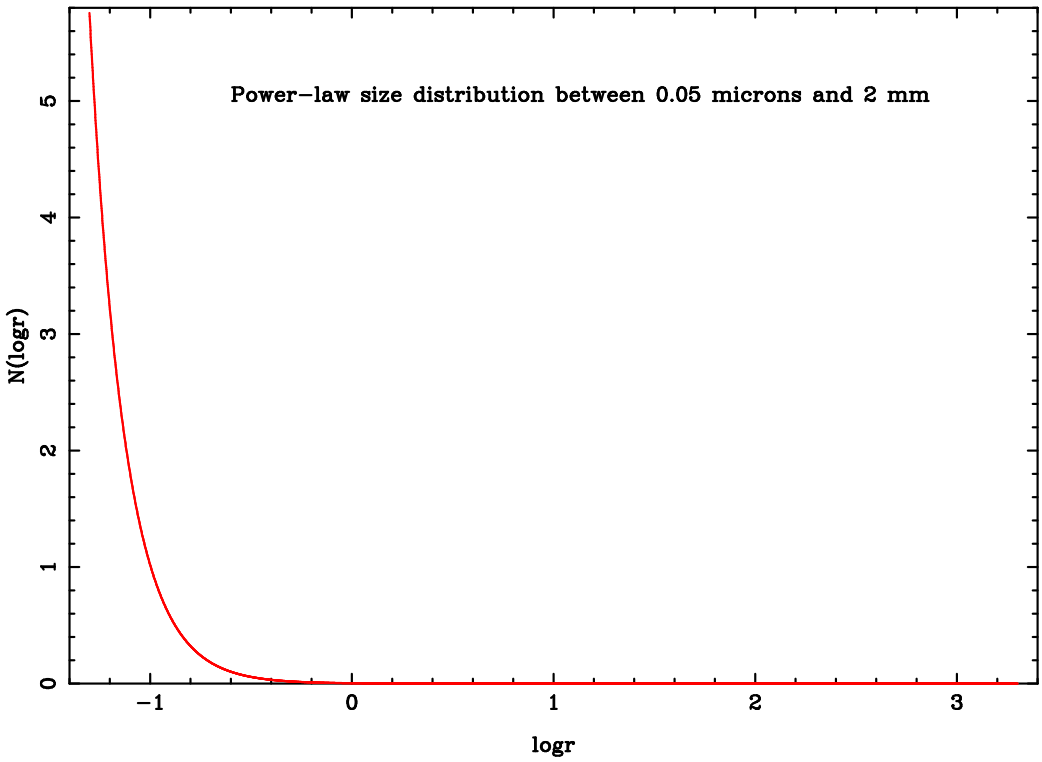

Figure 10.13: Power-law size distribution with $r_{min} = 0.05\ \mu m$, $r_{max} = 2\ mm$ and exponent $\delta = -3.5$. The curve was sampled with 5000 sizes to make smooth.

containing the direction of the incident light (see Fig. 10.16). An optical thickness τ_N was set for one of the halves, and $\gamma\tau_N$ for the other, with the condition that the optical thickness must be larger than 1 at least for one of the halves, in order to assure multiple scattering (otherwise no CP is possible, as stated in Sec. 10.2). Then, the DCP of light coming from the whole coma was calculated.

Some important modifications had to be introduced in the main equations that govern the model (Sec. 10.3.3) to make it work for the coma described in Fig. 10.16. In particular, Eqs. 10.15 to 10.22 are not valid for packets of photons which path crosses both halves of the coma.

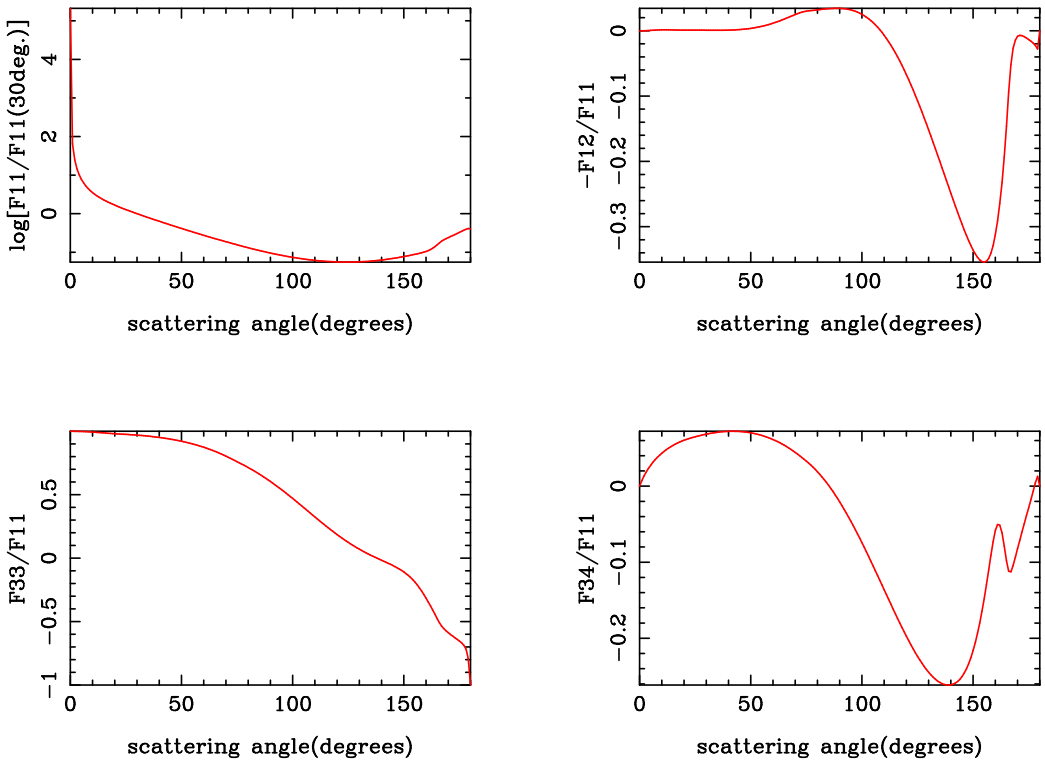

Figure 10.14: Non-zero independent elements of the scattering matrix of a sample of spheres with a size distribution as that given in Fig. 10.13. The curves are smooth, and all necessary conditions at the forward- and backward-scattering directions are fulfilled.

Suppose that a packet of photons located at P_0 (see Fig. 10.16) takes its next step to its destination P_d, where P_d might be the nucleus (A), the infinity (B) or another point P_2 in the coma (C). For each case, there exist four possibilities:

1. $P_0, P_d \in \tau_N$

2. $P_0, P_d \in \gamma\tau_N$

3. $P_0 \in \tau_N,\ P_d \in \gamma\tau_N$

4. $P_0 \in \gamma\tau_N,\ P_d \in \tau_N$

Some simple algebraic manipulations leads to the following equations for the cases enumerated above:

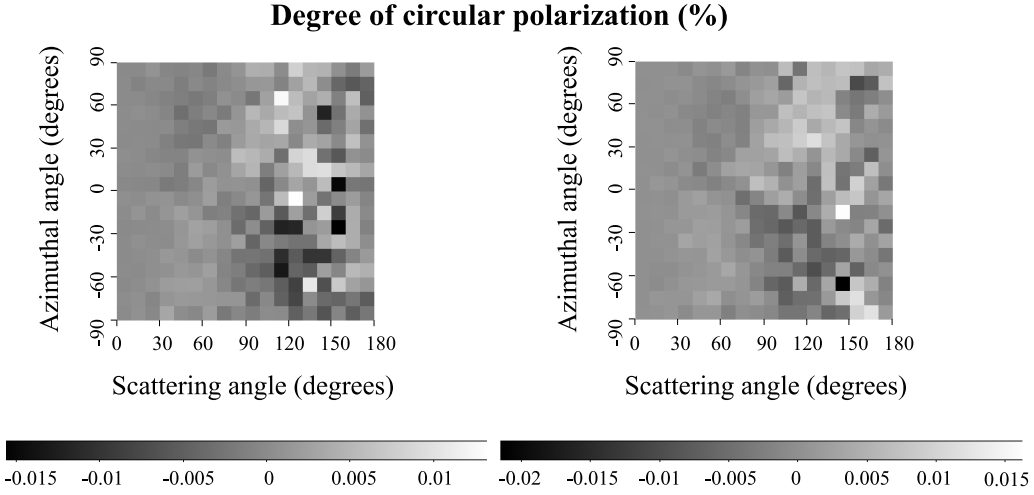

Figure 10.15: Results for the calculations of the DCP with our radiative transfer model. All parameters of the model are taken from Tables 10.1 and 10.3, except for r_{max}, that is set to 200 μm for the left panel. Only results for light scattered at φ within $[-90°, 90°]$ are presented, because the best statistics is achieved within this interval.

A1)

$$\tau_c = \frac{\tau_N R_N}{\Delta}\left(\arctan\frac{\mathbf{r_0}\cdot\hat{\mathbf{e}}+s_c}{\Delta} - \arctan\frac{\mathbf{r_0}\cdot\hat{\mathbf{e}}}{\Delta}\right), \tag{10.34}$$

if $\Delta \neq 0$, with $\Delta = \sqrt{r_0^2 - (\mathbf{r_0}\cdot\hat{\mathbf{e}})^2}$.

A2)

The same as in *A1* but exchanging τ_N by $\gamma\tau_N$.

A3)

$$\tau_c = \frac{\tau_N R_N}{\Delta}\left(\arctan\frac{\mathbf{r_0}\cdot\hat{\mathbf{e}}+s_1}{\Delta} - \arctan\frac{\mathbf{r_0}\cdot\hat{\mathbf{e}}}{\Delta}\right) + \frac{\gamma\tau_N R_N}{\Delta}\left(\arctan\frac{\mathbf{r_1}\cdot\hat{\mathbf{e}}+s_2}{\Delta} - \arctan\frac{\mathbf{r_1}\cdot\hat{\mathbf{e}}}{\Delta}\right), \tag{10.35}$$

if $\Delta \neq 0$, with $\Delta = \sqrt{r_0^2 - (\mathbf{r_0}\cdot\hat{\mathbf{e}})^2} = \sqrt{r_1^2 - (\mathbf{r_1}\cdot\hat{\mathbf{e}})^2}$. Longitude s_1 is the distance from P_0 to P_1 (see Fig. 10.16), and $s_2 = s_c - s_1$.

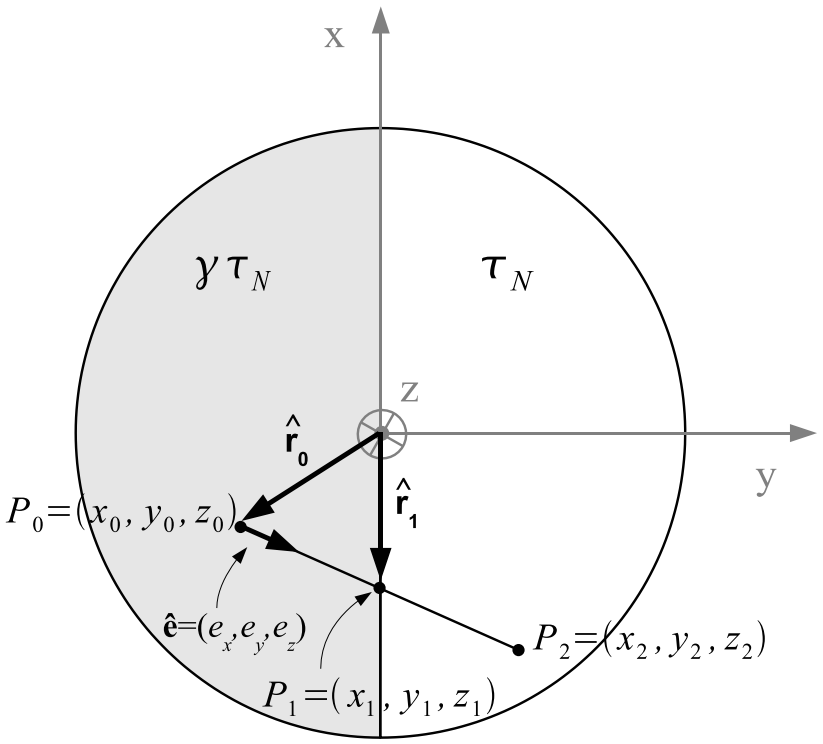

Figure 10.16: Asymmetrical coma formed by two halves of different optical thicknesses: τ_N and $\gamma\tau_N$. The optical axis is contained in the plane that separates both parts. A packet of photons travels from a point (x_0, y_0, z_0) in one part to (x_2, y_2, z_2) in the other crossing the interface plane at (x_1, y_1, z_1).

A4)

The same as in *A3* but exchanging τ_N by $\gamma\tau_N$.

B1)

$$\tau_\infty = \frac{\tau_N R_N}{\Delta}\left(\frac{\pi}{2} - \arctan\frac{\mathbf{r_0}\cdot\hat{\mathbf{e}}}{\Delta}\right), \tag{10.36}$$

if $\Delta \neq 0$, with $\Delta = \sqrt{r_0^2 - (\mathbf{r_0}\cdot\hat{\mathbf{e}})^2}$.

B2)

The same as in *B1* but exchanging τ_N by $\gamma\tau_N$.

B3)

$$\tau_\infty = \frac{\tau_N R_N}{\Delta}\left(\arctan\frac{\mathbf{r_0}\cdot\hat{\mathbf{e}}+s_1}{\Delta} - \arctan\frac{\mathbf{r_0}\cdot\hat{\mathbf{e}}}{\Delta}\right) + \frac{\gamma\tau_N R_N}{\Delta}\left(\frac{\pi}{2} - \arctan\frac{\mathbf{r_1}\cdot\hat{\mathbf{e}}}{\Delta}\right), \tag{10.37}$$

if $\Delta \neq 0$, with $\Delta = \sqrt{r_0^2 - (\mathbf{r_0}\cdot\hat{\mathbf{e}})^2} = \sqrt{r_1^2 - (\mathbf{r_1}\cdot\hat{\mathbf{e}})^2}$.

B4)
The same as in *B3* but exchanging τ_N by $\gamma\tau_N$.

C1) $y_0 \geq 0$, $e_y \geq 0$

$$s = \Delta\tan\frac{\Delta\tau}{\tau_N R_N} + \arctan\frac{\mathbf{r_0}\cdot\hat{\mathbf{e}}}{\Delta} - \mathbf{r_0}\cdot\hat{\mathbf{e}}, \tag{10.38}$$

if $\Delta \neq 0$, with $\Delta = \sqrt{r_0^2 - (\mathbf{r_0}\cdot\hat{\mathbf{e}})^2}$.

C2) $y_0 < 0$, $e_y < 0$
The same as in *C1* but exchanging τ_N by $\gamma\tau_N$.

C3) $y_0 \geq 0$, $e_y < 0$
Let us suppose $\Delta \neq 0$, with $\Delta = \sqrt{r_0^2 - (\mathbf{r_0}\cdot\hat{\mathbf{e}})^2} = \sqrt{r_1^2 - (\mathbf{r_1}\cdot\hat{\mathbf{e}})^2}$. Then, we define:

$$\tau_{sep} = \frac{\tau_N R_N}{\Delta}\left(\arctan\frac{\mathbf{r_0}\cdot\hat{\mathbf{e}}+s_c}{\Delta} - \arctan\frac{\mathbf{r_0}\cdot\hat{\mathbf{e}}}{\Delta}\right). \tag{10.39}$$

If $\tau \leq \tau_{sep}$ (τ given by Eq. 10.8):

$$s = \Delta\tan\frac{\Delta\tau}{\tau_N R_N} + \arctan\frac{\mathbf{r_0}\cdot\hat{\mathbf{e}}}{\Delta} - \mathbf{r_0}\cdot\hat{\mathbf{e}}. \tag{10.40}$$

Otherwise:

$$s = \Delta\tan\frac{\Delta\tau}{\tau_N R_N} + \arctan\frac{\mathbf{r_0}\cdot\hat{\mathbf{e}}}{\Delta} - \mathbf{r_0}\cdot\hat{\mathbf{e}} + \Delta\tan\frac{\Delta\tau}{\gamma\tau_N R_N} + \arctan\frac{\mathbf{r_1}\cdot\hat{\mathbf{e}}}{\Delta} - \mathbf{r_1}\cdot\hat{\mathbf{e}} \tag{10.41}$$

C4) $y_0 < 0$, $e_y \geq 0$

Identical as in *C3* but exchanging τ_N by $\gamma\tau_N$.

The special case $\Delta = 0$ for cases *A1*, *A2*, *B1*, *B2*, *C1* and *C2* are presented below. For any other case Δ cannot be equal to zero because a packet of photons cannot cross from one half of the coma to the other in radial direction.

A1) For packets of photons approaching the nucleus, Eq. 10.18, and for those travelling far away, Eq. 10.19 (substituting in both cases τ by τ_c and s by s_c).

A2) The same as in *A1* but substituting τ_N by $\gamma\tau_N$.

B1) Eq. 10.20.

B2) The same as in *B2* but substituting τ_N by $\gamma\tau_N$.

C1) For packets of photons approaching the nucleus, Eq. 10.18, and for those travelling far away, Eq. 10.19.

C2) The same as in *C1* but changing τ_N by $\gamma\tau_N$.

$NPHOT$	10^8
$NRING$	10^8
τ_N	0.5
γ	10
$\Delta\theta$	1°
$\Delta\varphi$	1°

Table 10.4: Specific input parameters of the model that were used to calculate the DCP of light scattered by an azimuthally asymmetrical comet around the optical axis (see Fig. 10.16).

Fig. 10.17 shows the DCP produced by an asymmetrical comet with parameters given in Tables 10.1 and 10.4. Results for two different values of r_{max} are shown: 200 μm on the left and 2 mm on the right panel. Despite the artificial asymmetry that we imposed to the comet, no significant DCP compared to the observations was achieved by this mechanism either.

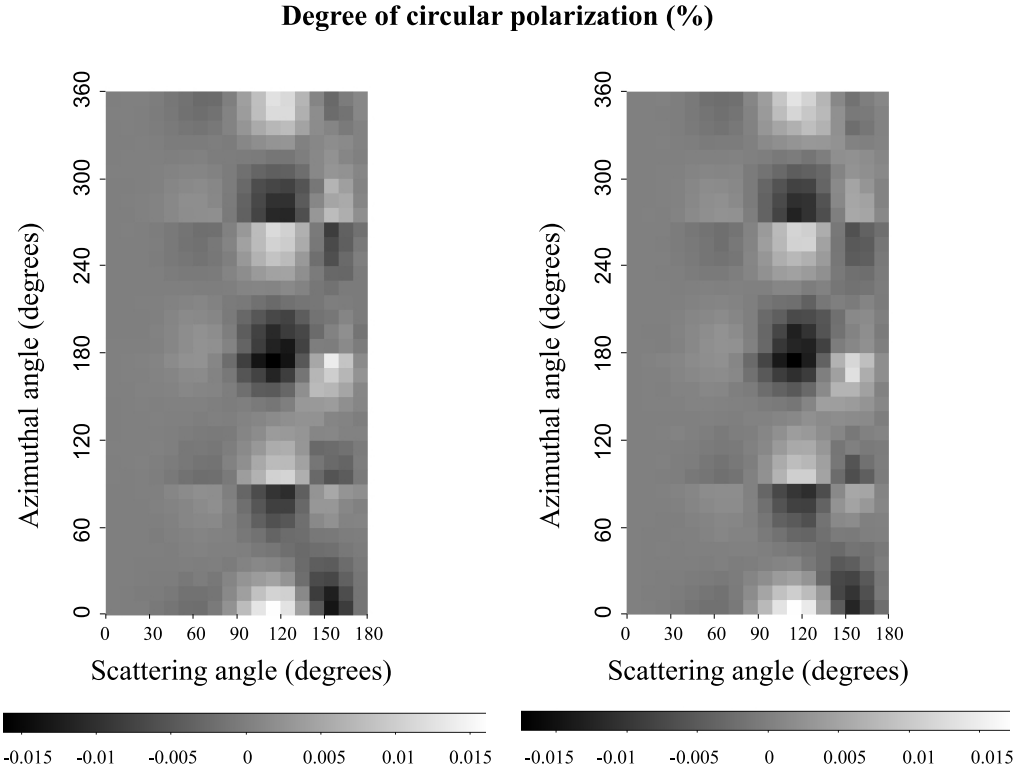

Figure 10.17: Results for the calculations of the DCP with our radiative transfer model. All parameters of the model are taken from Tables 10.1 and 10.4, except for r_{max}, that was set to 200 μm for the left panel, and 2 mm for the right one. Light coming from the whole comet is taken into account.

10.7 Local observation of an asymmetrical coma

Although mechanisms presented in Secs. 10.5 and 10.6 did not produce by themselves values of the DCP comparable to the observations, a mixture of both of them may give a different result. In the present section we calculate the DCP given by the same system as presented in Sec. 10.6. Moreover, the comet is locally observed as in the case presented in Sec. 10.5. The observation region is located in the half of the coma with the highest optical thickness (see Fig. 10.18). In this way, the maximum multiple scattering conditions are assured.

Specific input parameters for this run of the model are given in Table 10.5, and results are presented in Fig. 10.19.

Slightly higher values of the DCP have been achieved than in Secs. 10.5 and 10.6, but still the calculated values are one or two orders of magnitude

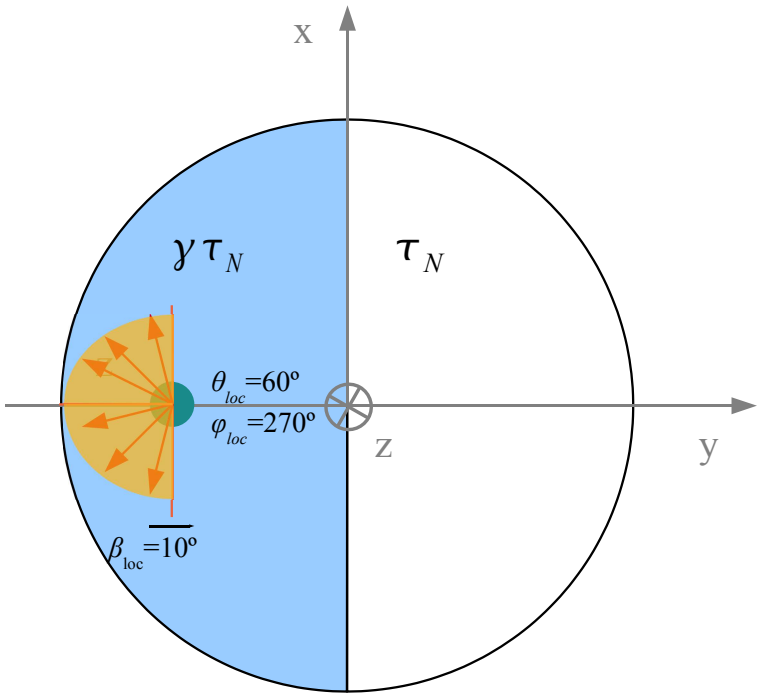

Figure 10.18: Target system to study in the present section: a comet is divided into two parts of different optical thicknesses, with multiple scattering at least in one of them. It is observed locally, i.e., just light coming from a certain small region of the coma is recorded. This region is located in the half of the coma with the highest optical thickness.

below the observations. However, we still rely on multiple scattering as the responsible mechanism of the observed DCP in comets because of the following reasons:

- As pointed out in Sec. 4.3, two common features to several observations of the DCP in comets are the tendency to the DCP to vanish when approaching the nucleus and when increasing the aperture of the used diaphragm. Local observation in a multiple scattering scenario is an explanation for both of these features, but the other discussed mechanisms can hardly be compatible with these facts.
- All mechanisms based on multiple scattering that we have studied in the present chapter, systematically give a non-negligible DCP, just one or two orders of magnitude below the observations.

$NPHOT$	10^7
$NRING$	10^7
r_{max}	200 μm
τ_N	0.5
γ	10
$\Delta\theta$	10°
$\Delta\varphi$	10°
θ_{loc}	60°
φ_{loc}	270°
β_{loc}	10°

Table 10.5: Specific input parameters used to calculate the DCP of light coming from a non-central local region of an azimuthally asymmetrical comet around the optical axis (see Fig. 10.18).

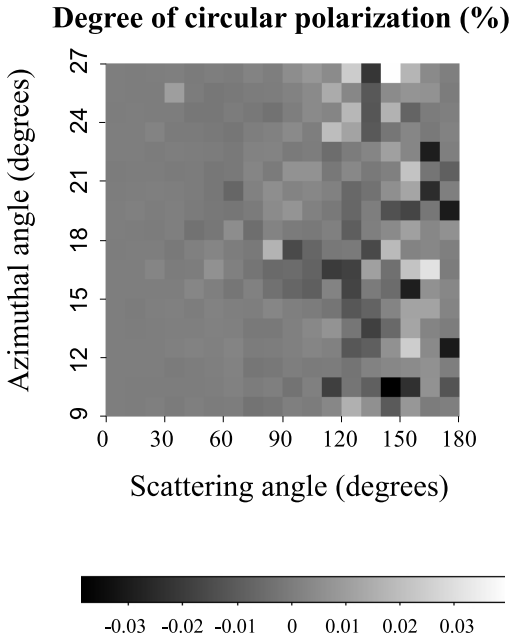

Figure 10.19: Calculations of the DCP with our radiative transfer model for a locally observed asymmetrical comet around the direction of the incident light (see Fig. 10.18). All parameters of the model are taken from Tables 10.1 and 10.5.

- Our calculations only deal with spherical particles, and grains with

more realistic shapes may yield higher values of the DCP.

- We are considering only silicates, but not carbon-like refractive indices. Changing the refractive index in the calculations may lead to values of the DCP comparable to the observations.

Using non-spherical (even asymmetrical) particles may yield highest values of the DCP. To make a good approximation to a real comet, we need to calculate the scattering matrices of non-spherical particles with sizes ranging from the order of 0.1 μm to 1 mm approximately (see Sec. 2.4). Techniques described in Sec. 3.5 are adequate to obtain the scattering matrices of particles of the order of the wavelength, and ray-tracing models [56] can make accurate calculations for particles much larger than the wavelength. For irregular shapes, there is still a wide range of sizes whose scattering properties cannot be calculated by any known method.

10.8 Conclusions

- A new model of radiative transfer in the coma of comets has been developed, including any kind of particles either in conditions of single or multiple scattering.

- A certain DCP appears in an azimuthally symmetrical comet if we break the symmetry of the system by considering only light coming from a non-central zone of the comet in conditions of multiple scattering. However, the obtained values of the DCP are one or two orders of magnitude below the observations when using spherical silicate-like particles for the dust grains of the coma.

- A non-negligible DCP arises when integrating all light coming from a non-symmetrical comet (coma divided into two part with very different optical thicknesses, the optical axis contained in the plane that separates both parts). Again the values are one or two orders of magnitude below the observations. Observing just a small region of the high-density half of the coma does not lead to results comparable to the observations either.

- Using non-spherical particles or a carbon-like refractive index for the grains of the coma may yield higher calculated values of the DCP.

Chapter 11

Conclusions

Regarding the observations:

- In all cases, the observed DCP for a certain region of the comet is highly variable in time (day-to-day and even minute-to-minute variations).
- The DCP approaches zero when the aperture of the diaphragm increases in observations of Halley.
- For accurate observations, such as those of Hale-Bopp, and others acquired later, the DCP approaches zero when looking at the nuclear region of the comet.
- In most cases, both positive and negative values of the DCP are obtained, except for two exceptions: observations of Hale-Bopp by Rosenbush et al. [63], where all obtained values were negative, and observations of Comet C/1999 S4. For the latter case, all observed values were positive for the smallest phase angle (60.9°). Then both positive and negative values appeared at intermediate values of ϕ, becoming finally mostly negative at $\phi \approx 120°$.

Regarding the candidate mechanisms to produce CP:

- The breaking of the symmetry of a comet around the direction of the incident light is a necessary condition for a mechanism to circularly polarize the scattered light.
- A complete list of candidates to produce CP of light scattered in comets is the following:

1. Alignment of non-spherical grains.
2. Breaking of the mirror symmetry.
3. Optical activity of the material composing the particles.
4. Local observation of a non-central region.
5. Inhomogeneous distribution of particles in the coma.
6. Asymmetrical nucleus of the comet.

Regarding the alignment of non-spherical particles:

- Prolate rectangular prisms of dimensions $0.1\ \mu m \times 0.1\ \mu m \times 0.2\ \mu m$ with a density of 3 gcm^{-3} are aligned in $1.8 \cdot 10^4\ s$ due to the bombardment by the solar wind particles at an heliocentric distance of $1AU$.
- The alignment occurs with the longest axis of the particle oriented perpendicularly to the direction of the incident light.
- Oblate particles with the same volume and density as the prolate ones, but with axes ratios 2:2:1, are not aligned even in $2.4 \cdot 10^5\ s$.
- If particles in comets were actually aligned and the responsible mechanism for the alignment was the bombardment by the solar wind, we would not obtained any non-zero DCP, because the cloud of aligned particles would be symmetrical around the direction of the incident light.

Regarding asymmetrical model particles:

- For the snake-like shape with seven monomers and $m = 1.5 + i0.001$, the mean amplitude of the curve of the DCP is close to zero for small size parameters (as corresponds to the Rayleigh domain), and then grows as the size parameters of the monomers increases to $x = 1.8$, in which case a maximum larger than 2% is found. When the size parameter becomes larger than $x = 1.8$, the amplitude decreases gradually, becoming essentially zero for $x = 10$.
- For the snake-like shape with seven monomers and $m = 1.5 + i0.001$, the complexity of the curves of the DCP increases always when increasing the size of the particle.
- Single scattering of optically inactive asymmetrical particles in random orientations can give large values of the DCP of the scattered light (more than 2%), at least for a snake-like aggregate composed of seven spherical monomers with $m = 1.5 + i0.001$.

- If we use a typical power-law size distribution, the curves of the DCP corresponding to snake-like aggregates made of 7 monomers with $m = 1.5+i0.001$ still show values of the DCP of the order of the observations ($\approx 0.1\%$ or less).

- Increasing the absorption of the particles makes the main amplitude of the curves of the DCP to decrease, at least for snake-like aggregates of seven monomers with $x = 2$ and $Re(m) = 1.5$. However, the effect is the opposite if the imaginary part of the refractive index is fixed to $Im(m) = 0.001$ and the real part is increased.

- By increasing the number of monomers of an aggregate, but keeping the whole size constant, the number of maxima and minima of DCP curves increases and the amplitudes of these decreases, at least for snake-like particles with $x = 2$ and $m = 1.5 + i0.001$.

- It is not necessary that monomers composing the aggregates are equal-sized to obtain high values of the DCP. In fact, the *snake* particle gives almost identical curves of the DCP even taking for the monomers volumes as different as V_0, $V_0 + 30\%V_0$ and $V_0 - 30\%V_0$.

- If the *snake* particle made of 7 monomers is compared to the *Mr Sanchez* particle (made of 25 monomers and more complex), the mean amplitude of the curve of the DCP is larger for the *snake* at small size parameters ($X \lesssim 4$), but it is comparable for both shapes if the size of the aggregates is large enough ($X \gtrsim 7$).

- The peaks of the curves of the DCP may be due to resonances. There exist two types of peaks: primary peaks (fixed number, at fixed scattering angles and due to resonances by the substructures that produce the asymmetry of the particle), and secondary peaks (the number increases with the size of the grain, not at fixed scattering angles and due to resonances by the monomers).

Regarding irregular particles:

- Primary peaks have smaller amplitudes in randomly built aggregates than in the asymmetrical model particles used in the previous chapter.

- Secondary peaks have larger amplitudes than primary ones in randomly built aggregates.

- The DCP of a sample of particles averaged over sizes for a fixed shape is mainly determined by the primary peaks, as in the case of model particles.

- A lower DCP arises from a size-averaged sample of randomly built aggregates of a fixed shape than for that of model grains.

- The DCP rapidly tends to zero when building a sample with just a few size-averaged shapes.

- Single scattering by asymmetrical particles in random orientation does not make a significant contribution of the observed DCP in comets.

Regarding optical activity:

Althoug there are evidences that optical active materials are present in comets, we rule out the scattering by optically active grains as the responsible mechanism for the DCP observed in comets, because it does not match some of the features found in the observations.

Regarding multiple scattering:

- A new model of radiative transfer in the coma of comets has been developed, including any kind of particles either in conditions of single or multiple scattering.

- A certain DCP appears in an azimuthally symmetrical comet if we break the symmetry of the system by considering only light coming from a non-central zone of the comet in conditions of multiple scattering. However, the obtained values of the DCP are one or two orders of magnitude below the observations when using spherical silicate-like particles for the dust grains of the coma.

- A non-negligible DCP arises when integrating all light coming from a non-symmetrical comet (coma divided into two part with very different optical thicknesses, the optical axis contained in the plane that separates both parts). Again the values are one or two orders of magnitude below the observations. Observing just a small region of the high-density half of the coma does not lead to results comparable to the observations either.

- Using non-spherical particles or a carbon-like refractive index for the grains of the coma may yield higher calculated values of the DCP.

Chapter 12

Future work

- To perform calculations of the DCP with the Monte Carlo radiative transfer model by using non-spherical particles of sizes ranging from 0.1 μm to 1 mm.
- To perform calculations of the DCP with the Monte Carlo radiative transfer model by using a refractive index typical for amorphous carbon.
- To include the possibility to use a particular scattering matrix for each particle at each orientation in the Monte Carlo model, instead of using average matrices.
- To include the possibility of a layered number density distribution of particles in the coma for the radiative transfer model in order to fit linear polarization *in situ* measurements of the $EDLP$ in the atmosphere of Titan (collaboration with Robert West-JPL).
- To include the possibility of dealing with numerical, instead of analytical, number density distributions of particles in the coma for the radiative transfer model. This would be applicable, e.g., to the outputs of the circumnuclear coma hydrodynamic models by Crifo [10].
- To build a numerical code to calculate the DCP given by optically active particles.
- To mix together several candidate mechanisms producing CP by using, in the radiative transfer model, scattering matrices corresponding to aligned, asymmetrical and optically active particles.
- To build an adequate model of scattering on surfaces and use it to simulate the reflection of light on the nucleus of the comet.

Appendix A

General method to sample values of a variable from its probability density function

The probability density p of a variable x is defined such as the probability of x to be between x_1 and x_2 is given by $P(x_1 \leq x \leq x_2) = \int_{x_1}^{x_2} p(x)dx$. The probability is equal to the area under the curve of $p(x)$ from x_1 to x_2: equal areas means equal probabilities. Let us divide now the area under the curve of $p(x)$ into infinite regions of elemental surface dS. The probability of x to be within each of those regions is the same, because they all have the same area. A way of sampling x is to uniformly randomly choose one region of area dS (a), and then calculate the coordinate x corresponding to that region (b). Step (a) can be achieved as follows: the chosen region is the last elemental surface added to the integral $S(x) = \int_0^x p(x')dx'$ to make it a certain value ξ. If ξ is uniformly distributed, all regions of area dS will be equally probable. Step (b) simply consists on finding the value of x that makes $S(x) = \xi$.

In summary, a way to sample values of x from a probability density function p is the following:

1. To determine a uniform random number ξ within $[0, 1]$.
2. To work x out from $S(x) = \xi$.

Bibliography

[1] C.F. Bohren. Light scattering by an optically active sphere. *Chemical Physics Letters*, 29:458–462, 1974.

[2] C.F. Bohren. Scattering of electromagnetic waves by an optically active cylinder. *J. Colloid Interface Sci.*, 66:105–109, 1978.

[3] C.F. Bohren and D.R. Huffman. *Absorption and Scattering of Light by Small Particles*. Wiley, 1983.

[4] M. Born, E. Wolf, and A.B. Bhatia. *Principles of Optics*. Cambridge University Press, October 1999.

[5] D. Brownlee, P. Tsou, J. Aléon, C.M.O'D. Alexander, T. Araki, S. Bajt, G.A. Baratta, R. Bastien, P. Bland, P. Bleuet, J. Borg, J.P. Bradley, A. Brearley, F. Brenker, S. Brennan, J.C. Bridges, N.D. Browning, J.R. Brucato, E. Bullock, M.J. Burchell, H. Busemann, A. Butterworth, M. Chaussidon, A. Cheuvront, Miaofang Chi, Mark J. Cintala, B. C. Clark, S.J. Clemett, G. Cody, L. Colangeli, G. Cooper, P. Cordier, C. Daghlian, Z. Dai, L. D'Hendecourt, Z. Djouadi, G. Dominguez, T. Duxbury, J.P. Dworkin, D.S. Ebel, T.E. Economou, S. Fakra, S.A.J. Fairey, S. Fallon, G. Ferrini, T. Ferroir, H. Fleckenstein, C. Floss, G. Flynn, I.A. Franchi, M. Fries, Z. Gainsforth, J.-P. Gallien, M. Genge, M.K. Gilles, P. Gillet, J. Gilmour, D.P. Glavin, M. Gounelle, M.M. Grady, G.A. Graham, P.G. Grant, S.F. Green, F. Grossemy, L. Grossman, J.N. Grossman, Y. Guan, K. Hagiya, R. Harvey, P. Heck, G.F. Herzog, P. Hoppe, F. Hörz, J. Huth, I.D. Hutcheon, K. Ignatyev, H. Ishii, M. Ito, D. Jacob, C. Jacobsen, S. Jacobsen, S. Jones, D. Joswiak, A. Jurewicz, A.T. Kearsley, L.P. Keller, H. Khodja, A.L.D. Kilcoyne, J. Kissel, A. Krot, F. Langenhorst, A. Lanzirotti, L. Le, L.A. Leshin, J. Leitner, L. Lemelle, H. Leroux, M.-C. Liu, K. Luening, I. Lyon, G. MacPherson, M.A. Marcus, K. Marhas, B. Marty, G. Matrajt, K. McKeegan, A. Meibom, V. Mennella, K. Messenger, S. Messenger, T. Mikouchi, S. Mostefaoui, T. Nakamura, T. Nakano, M. Newville,

L.R. Nittler, I. Ohnishi, K. Ohsumi, K. Okudaira, D.A. Papanastassiou, R. Palma, M.E. Palumbo, R.O. Pepin, D. Perkins, M. Perronnet, P. Pianetta, W. Rao, F.J.M. Rietmeijer, F. Robert, D. Rost, A. Rotundi, R. Ryan, S.A. Sandford, C.S. Schwandt, T.H. See, D. Schlutter, J. Sheffield-Parker, A. Simionovici, S. Simon, I. Sitnitsky, C.J. Snead, M.K. Spencer, F. J. Stadermann, A. Steele, T. Stephan, R. Stroud, J. Susini, S.R. Sutton, Y. Suzuki, M. Taheri, S. Taylor, N. Teslich, K. Tomeoka, N. Tomioka, A. Toppani, J.M. Trigo-Rodríguez, D. Troadec, A. Tsuchiyama, A.J. Tuzzolino, T. Tyliszczak, K. Uesugi, M. Velbel, J. Vellenga, E. Vicenzi, L. Vincze, J. Warren, I. Weber, M. Weisberg, A.J. Westphal, S. Wirick, D. Wooden, B. Wopenka, P. Wozniakiewicz, I. Wright, H. Yabuta, H. Yano, E.D. Young, R.N. Zare, T. Zega, K. Ziegler, L. Zimmerman, E. Zinner, and M. Zolensky. Comet 81P/Wild 2 under a microscope. *Science*, 314:1711, 2006.

[6] S. Chandrasekhar. *Radiative Transfer*. Courier Dover Publications, 1960.

[7] R.W. Christy, J.R. Reitz, and F.J. Milford. *Fundamentos de la Teoría Electromagnética*. Addison-Wesley Iberoamericana S. A., 1996.

[8] S.R. Cloude. Group theory and polarization algebra. *Optik*, 75:26, 1986.

[9] J.F. Crifo, M. Fulle, N.I. Kömle, and K. Szego. Nucleus-coma structural relationships: lessons from physical models. In *Comets II*, pages 471–503. University of Arizona Press, 2004.

[10] J.F. Crifo, G.A. Lukianov, A.V. Rodionov, G.O. Khanlarov, and V.V. Zakharov. Comparison between Navier-Stokes and direct Monte-Carlo simulations of the circumnuclear coma. I - Homogeneous, spherical source. *Icarus*, 156:249–268, 2002.

[11] P. Debye. Der lichtdruck auf kugeln von beliebigem material. *Annalen der Physik*, 335:57–136, 1909.

[12] J.C. del Toro Iniesta. *Introduction to Spectropolarimetry*. Cambridge University Press, 2003.

[13] A.Z. Dolginov and I.G. Mitrofanov. Orientation of cometary dust and polarization observations of comets. *Soviet Astronomy*, 19:758–764, 1976.

[14] A. Dollfus and J.-L. Suchail. Polarimetry of grains in the coma of P/Halley. I - Observations. *Astronomy and Astrophysics*, 187:669–688, November 1987.

[15] M. Donahue, J. Bennett, N. Schneider, and M. Voit. *The Essential Cosmic Perspective*. Addison-Wesley, 2006.

[16] B.T. Draine and P.J. Flatau. Discrete-dipole approximation for scattering calculations. *Journal of the Optical Society of America A*, 11:1491–1499, 1994.

[17] B.T. Draine and P.J. Flatau. User guide for the discrete dipole approximation code DDSCAT 7.0. *http://arXiv.org/abs/0809.0337v5*, 2008.

[18] A. Einstein. Über einen die erzeugung und verwandlung des lichtes betreffenden heuristischen gesichtspunkt. *Annalen der Physik*, 322:132–148, 1905.

[19] M.C. Festou, H. Rickman, and R.M. West. Comets. I - Concepts and observations. *Astronomy and Astrophysics Review*, 4:363–447, 1993.

[20] M. Fulle. Motion of cometary dust. In *Comets II*, pages 565–575. University of Arizona Press, 2004.

[21] D.P. Glavin, J.P. Dworkin, and S.A. Sandford. Detection of cometary amines in samples returned by Stardust. *Meteoritics and Planetary Science*, 43:399–413, 2008.

[22] D. Guirado, J.W. Hovenier, and F. Moreno. Circular polarization of light scattered by asymmetrical particles. *Journal of Quantitative Spectroscopy and Radiative Transfer*, 106:63–73, 2007.

[23] D. Guirado, F. Moreno, and J.W. Hovenier. Circular polarization of light scattered by randomly built aggregates. In *X Conference on Electromagnetic & Light Scattering by Non-Spherical Particles*, pages 45–48, Bodrum (Turkey), 2007.

[24] D. Guirado, F. Moreno, and M.I. Mishchenko. A new mechanism possibly explaining the circular polarization of light scattered in comets: asymmetry of the comet itself. In *XI Conference on Electromagnetic & Light Scattering by Non-Spherical Particles*, Hertfordshire (UK), 2008.

[25] J.E. Hansen and L.D. Travis. Light scattering in planetary atmospheres. *Space Science Reviews*, 16:527–610, October 1974.

[26] F. Hörz, R. Bastien, J. Borg, J.P. Bradley, J.C. Bridges, D.E. Brownlee, M.J. Burchell, M. Chi, M.J. Cintala, Z.R. Dai, Z. Djouadi, G. Domínguez, T.E. Economou, S.A.J. Fairey, C. Floss, I.A. Franchi, G.A. Graham, S.F. Green, P. Heck, P. Hoppe, J. Huth, H. Ishii, A.T. Kearsley, J. Kissel, J. Leitner, H. Leroux, K. Marhas, K. Messenger, C.S. Schwandt, T.H. See, C. Snead, F.J. Stadermann, T. Stephan, R. Stroud, N. Teslich, J.M. Trigo-Rodríguez, A.J. Tuzzolino, D. Troadec, P. Tsou, J. Warren, A. Westphal, P. Wozniakiewicz, I. Wright, and E. Zinner. Impact features on Stardust: implications for comet 81P/Wild 2 dust. *Science*, 314:1716, 2006.

[27] J.W. Hovenier. Measuring scattering matrices of small particles at optical wavelengths. In *Light Scattering by Nonspherical Particles: Theory, Measurments and Applications.*, page 355. Academic Press, 2000.

[28] J.W. Hovenier, C. van der Mee, and H. Domke. *Transfer of Polarized Light in Planetary Atmospheres*. Springer, 2004.

[29] J.W. Hovenier and C.V.M. van der Mee. Testing scattering matrices: a compendium of recipes. *Journal of Quantitative Spectroscopy and Radiative Transfer*, 55:649–661, 1996.

[30] J.W. Hovenier and C.V.M. van der Mee. Basic relationships for matrices describing scattering by small particles. In *Light Scattering by Nonspherical Particles: Theory, Measurements and Applications*, pages 61–85. Academic Press, 2000.

[31] K. Jockers. Observations of scattered light from cometary dust and their interpretation. *Earth Moon and Planets*, 79:221–245, 1997.

[32] H.U. Keller. Properties of cometary nuclei. In *Revista Mexicana de Astronomía y Astrofísica Conference Series*, volume 35, page 285, Isla Margarita (Venezuela), 2009.

[33] H.U. Keller, C. Arpigny, C. Barbieri, R.M. Bonnet, S. Cazes, M. Coradini, C.B. Cosmovici, W.A. Delamere, W.F. Huebner, D.W. Hughes, C. Jamar, D. Malaise, H.J. Reitsema, H.U. Schmidt, W.K.H. Schmidt, P. Seige, F.L. Whipple, and K. Wilhelm. First Halley multicolour camera imaging results from Giotto. *Nature*, 321:320–326, 1986.

[34] M.S. Kelley and D.H. Wooden. The composition of dust in jupiter-family comets inferred from infrared spectroscopy. *Planetary and Space Science*, 57:1133–1145, 2009.

[35] R.E. Kleinman and T.B.A. Senior. Rayleigh scattering. In *Low and High Frequency Asymptotics*. North-Holland: Sole distributors for the USA and Canada, Elsevier Science Pub. Co, 1986.

[36] L. Kolokolova and K. Jockers. Composition of cometary dust from polarization spectra. *Planetary and Space Science*, 45:1543–1550, 1997.

[37] L. Kolokolova, H. Kimura, K. Ziegler, and I. Mann. Light-scattering properties of random-oriented aggregates: Do they represent the properties of an ensemble of aggregates? *Journal of Quantitative Spectroscopy and Radiative Transfer*, 100:199–206, 2006.

[38] A. Lazarian. Magnetic fields via polarimetry: progress of grain alignment theory. *Journal of Quantitative Spectroscopy and Radiative Transfer*, 79:881–902, 2003.

[39] L. Lorenz. Über die refractionconstante. *Ann. Phys. Chem.*, 11:70–103, 1880.

[40] A.E.H. Love. The scattering of electric waves by a dielectric sphere. In *London. Math. Soc. Conference*, volume 30, pages 308–321, London, 1899.

[41] R.W. Maas, E.P. Ney, and N.J. Woolf. The 10-MICRON emission peak of comet Bennett 1969i. *Astrophysical Journal*, 160:L101, 1970.

[42] D.W. Mackowski and M.I. Mishchenko. Calculation of the T-matrix and the scattering matrix for ensembles of spheres. *Journal of the Optical Society of America A*, 13:2266–2278, 1996.

[43] N. Manset and P. Bastien. Polarimetric observations of comets C/1995 O1 Hale-Bopp and C/1996 B2 Hyakutake. *Icarus*, 145:203–219, May 2000.

[44] E.P. Mazets, R.L. Aptekar, S.V. Golenetskii, Y.A. Guryan, A.V. Dyachkov, V.N. Ilyinskii, V.N. Panov, G.G. Petrov, A.V. Savvin, R.Z. Sagdeev, I.A. Sokolov, N.G. Khavenson, V.D. Shapiro, and V.I. Shevchenko. Comet Halley dust environment from SP-2 detector measurements. *Nature*, 321:276–278, 1986.

[45] L.M. Merino-González and E. Santos-Aláez. *Álgebra lineal*. Publicated by the authors, 1997.

[46] K. Metz and R. Haefner. Circular polarization near the nucleus of comet P/Halley. *Astronomy and Astrophysics*, 187:539–542, 1987.

[47] G. Mie. Beiträge zur optik trüber medien, speziell kolloidaler metallösungen. *Annalen der Physik*, 330:377–445, 1908.

[48] M. Min, J.W. Hovenier, A. de Koter, L.B.F.M. Waters, and C. Dominik. The composition and size distribution of the dust in the coma of comet Hale Bopp. *Icarus*, 179:158–173, 2005.

[49] M.I. Mishchenko and L.D. Travis. Satellite retrieval of aerosol properties over the ocean using polarization as well as intensity of reflected sunlight. *Journal of Geophysical Research*, 102(D14):16989–17013, 1997.

[50] M.I. Mishchenko, L.D. Travis, and A.A. Lacis. *Multiple Scattering of Light by Particles*. Cambridge University Press, 2006.

[51] M.I. Mishchenko, L.D. Travis, and D.W. Mackowski. T-matrix computations of light scattering by nonspherical particles: a review. *Journal of Quantitative Spectroscopy and Radiative Transfer*, 55:535–575, 1996.

[52] F. Moreno, O. Muñoz, D. Guirado, and R. Vilaplana. Comet dust as a size distribution of irregularly shaped, compact particles. *Journal of Quantitative Spectroscopy and Radiative Transfer*, 106:348–359, 2007.

[53] F. Moreno, O. Muñoz, J.J. López-Moreno, A. Molina, and J.L. Ortiz. A Monte Carlo code to compute energy fluxes in cometary nuclei. *Icarus*, 156:474–484, 2002.

[54] A.V. Morozhenko, N.N. Kiselev, and A.L. Gural'Chuk. On the circular polarization of comet Halley head. *Kinematika i Fizika Nebesnykh Tel*, 3:89, April 1987.

[55] O. Muñoz, F. Moreno, D. Guirado, J.L. Ramos, A. López, F. Girela, J.M. Jerónimo, L.P. Costillo, and I. Bustamante. Experimental determination of scattering matrices of dust particles at visible wavelengths: the IAA light scattering apparatus. *Journal of Quantitative Spectroscopy and Radiative Transfer*, 111:187–196, 2010.

[56] K. Muinonen, T. Nousiainen, P. Fast, K. Lumme, and J. Peltoneimi. Light scattering by Gaussian random particles: ray optics approximation. *Journal of Quantitative Spectroscopy and Radiative Transfer*, 55:577–601, 1996.

[57] P. Murdin. *Encyclopedia of Astronomy and Astrophysics*. Nature Publishing Group, 2001.

[58] T. Oguchi. Scattering properties of oblate raindrops & cross polarization of radio waves due to rain. calculations at 19.3 & 34.8 GHz. *J Radio Res. Lab. Jpn.*, 20:79–118, 1973.

[59] T. Oguchi. Light scattering by a spheroidal particle. *Appl. Optics*, 14:29–49, 1975.

[60] A. Penttilä, E. Zubko, K. Lumme, K. Muinonen, M.A. Yurkin, B. Draine, J. Rahola, A.G. Hoekstra, and Y. Shkuratov. Comparison between discrete dipole implementations and exact techniques. *Journal of Quantitative Spectroscopy and Radiative Transfer*, 106:417–436, 2007.

[61] V. Rosenbush, N. Kiselev, N. Shakhovskoy, S. Kolesnikov, and V. Breus. Circular and linear polarization of comet C/2001 Q4 (NEAT). Why circular polarization in comets is predominantly left-handed? In *X Conference on Electromagnetic & Light Scattering by Non-Spherical Particles*, pages 181–184, Bodrum (Turkey), 2007.

[62] V. Rosenbush, L. Kolokolova, A. Lazarian, N. Shakhovskoy, and N. Kiselev. Circular polarization in comets: observations of comet C/1999 S4 (LINEAR) and tentative interpretation. *Icarus*, 186:317–330, 2007.

[63] V.K. Rosenbush, N.M. Shakhovskoj, and A.E. Rosenbush. Polarimetry of comet Hale-Bopp: linear and circular polarization, stellar occultation. *Earth Moon and Planets*, 78:381–386, 1999.

[64] H. Salo. Monte Carlo modeling of the net effects of coma scattering and thermal reradiation on the energy input to cometary nucleus. *Icarus*, 76:253–269, 1988.

[65] S.A. Sandford, J. Aléon, C.M.O'D. Alexander, T. Araki, S. Bajt, G.A. Baratta, J. Borg, J.P. Bradley, D.E. Brownlee, J.R. Brucato, M.J. Burchell, H. Busemann, A. Butterworth, S.J. Clemett, G. Cody, L. Colangeli, G. Cooper, L. D'Hendecourt, Z. Djouadi, J.P. Dworkin, G. Ferrini, H. Fleckenstein, G.J. Flynn, I.A. Franchi, M. Fries, M.K. Gilles, D.P. Glavin, M. Gounelle, F. Grossemy, C. Jacobsen, L.P. Keller, A.L.D. Kilcoyne, J. Leitner, G. Matrajt, A. Meibom, V. Mennella, S. Mostefaoui, L.R. Nittler, M.E. Palumbo, D.A. Papanastassiou, F. Robert, A. Rotundi, C.J. Snead, M.K. Spencer, F.J. Stadermann, A. Steele, T. Stephan, P. Tsou, T. Tyliszczak, A.J. Westphal, S. Wirick, B. Wopenka, H. Yabuta, R.N. Zare, and M.E. Zolensky. Organics captured from comet 81P/Wild 2 by the Stardust spacecraft. *Science*, 314:1720, 2006.

[66] S.A. Stern. The evolution of comets in the Oort cloud and Kuiper belt. *Nature*, 424:639–642, 2003.

[67] W. Sun, Q. Fu, and Z. Chen. Finite-Difference Time-Domain solution of light scattering by dielectric particles with a perfectly matched layer absorbing boundary condition. *Applied Optics*, 38:3141–3151, 1999.

[68] H.C. van de Hulst. *Light Scattering by Small Particles*. Courier Dover Publications, 1981.

[69] R. Vilaplana, J. Cantó, F. Moreno, and D. Guirado. The influence of particles shapes and sizes in the CO ice stretching mode. *Earth, Planets and Space*, accepted for publication, 2009.

[70] J.R. Wait. Scattering of a plane wave from a circular dielectric cylinder at oblique incidence. *Canadian Journal of Physics*, 33:189–195, 1955.

[71] Y.-L. Xu and B.S. Gustafson. A generalized multiparticle Mie-solution: further experimental verification. *Journal of Quantitative Spectroscopy and Radiative Transfer*, 70:395–419, 2001.

[72] M.A. Yurkin and A.G. Hoekstra. User manual for the discrete dipole approximation code Amsterdam DDA (version 0.79). *http://www.science.uva.nl/research/scs/Software/adda/index.html*, 2009.